Probing surfaces and interfaces by nonlinear optical spectroscopy with time, energy, and phase resolution

Cory Nelson

Submitted in partial fulfillment of the

requirements for the degree

of Doctor of Philosophy

in the Graduate School of Arts and Sciences

COLUMBIA UNIVERSITY

2015

ABSTRACT

Probing surfaces and interfaces by nonlinear optical spectroscopy with time, energy, and phase resolution

Cory Nelson

Surfaces and interfaces are a ubiquitous part of nature. They influence the behavior of devices and are essential components in charge transfer and charge trapping. While surfaces and interfaces are important studying them is difficult because they consist of only the first few layers of a material. Therefore, surface-specific techniques are needed to investigate their properties and dynamics.

Perhaps the most common surface electronic surface characterization techniques are electron spectroscopies which have become the standard for determining surface electronic band structure. However, these spectroscopies require ultra high vacuum which precludes the study of surfaces at ambient pressures and buried interfaces. Ambient pressures and interfaces are precisely the conditions under which most devices operate. Therefore there is a need for a technique which can reveal information about electronic states and their dynamics of buried interfaces at ambient conditions.

This thesis describes the implementation of broadband time-resolved second harmonic generation and the recovery of the time-resolved amplitude and phase by employing spectral interferometry. The even order nonlinear process allows the measurement to be surface specific which the spectral amplitude and phase reveal information about surface state transitions and couplings. The first chapter motivates the study of surface and interfaces while chapters 2 and 3 cover background information about surfaces and nonlinear optics to help understand the experiments presented in the following two chapters.

Chapter 4 presents a broadband time resolved spectral SHG technique whose usefulness is demonstrated on gallium phosphide passivated undoped gallium arsenide. In this case the spec-

tral features are due to the E_1 resonance in GaAs and the dynamics are assigned to band gap renormalization.

Chapter 5 details a method to recover the time resolved amplitude and phase and then demonstrates the recovery of the amplitude and phase from SH emitted from n- and p-type GaAs. The spectra reveal a discreet surface state ascribed to defect formation specific to n-type GaAs. The asymmetric line shape of this state indicates that it is coupled to a continuum; most likely a surface projected bulk band. We found that this coupling can be controlled by changing the azimuthal angle. However, p-type GaAs does not show distinct features in the second harmonic spectrum.

Experiments on bilayers consisting of p-type GaAs and copper pthalocyanine (CuPc) are also presented in chapter 5. No changes in the signal are observed for either the constituents alone. However, when CuPc is deposited on GaAs a transient state forms at 200 fs delay between the pump delay which also exhibits an asymmetric line shape. This indicates the formation of a new state at the heterojunction that was not present before and may be evidence for a charge transfer state.

Chapter 6 closes the thesis with concluding remarks which suggest improvements in the experimental design and implementation of time-resolved second harmonic spectral interferometry.

Table of Contents

List of Figures

List of Tables

Acknowledgments

First, thanks to my adviser, Xiaoyang Zhu, for always being available for discussions and for supporting some of my crazy ideas. Without your support and motivation this work would not have been possible. Your enthusiasm is infectious and has allowed me to become a better scientist.

Now, there is a long list of people who I need to thank from UT-Austin. I'll start by thanking the entire group that way no one can be angry if I leave them out. The group in Texas provided an atmosphere of unparalleled skepticism that promoted rigorous interpretation of data and what is actually measurable from a given experiment. This atmosphere, I believe allowed all of us to become the best scientists we could be. This environment has honed my critical thinking skills and has certainly aided in my growth as a scientist.

I need to thank some people specifically. First, from when I was working with quantum dots, thanks to Dr. Abraham Wolcott for teaching me everything you know about QD synthesis. Although I took a different direction in the end I appreciate the time and effort you put in to teach me. Secondly, thanks to Dr. Kenrick Williams. All of my knowledge about optics, detection, and how to write a LabView program that brings everything together into an optical setup that actually works comes from your guidance. None of the work in this thesis would have been possible with out it.

There were more than a few people that helped me come up with this idea. I am indebted to Dr. Josh Morris, for introducing the group to literature on the interferometric second harmonic spectroscopy. This was the Genesis for what became this thesis work. Dr. Askat Jailabakov was instrumental in coming up with a practical implementation of a time resolved version of interferometric second harmonic spectroscopy.

Thanks to those I never worked directly with but nevertheless gained an unfathomable amount

of knowledge from. For all things vacuum related Dr. John Tristch and Dr. Nick Monahan. Though I rarely used vacuum equipment I can say that I used it properly because of your guidance. Like a second adviser was Dr. Loren Kaake who helped me refine the basics of my knowledge which allowed me to progress the way I did after we moved from Texas.

Things were not so easy when we moved from Texas to Columbia and then moved from one lab to another. I attribute what remains of my sanity to the friends and coworkers who took me out of the lab and showed me how to enjoy New York City. I also must specially thank soon to be Dr. Nick Monahan for his critical suggestion that I exclusively use the home built oscillator when we finally moved into our final lab. This allowed me to work at my leisure on developing the technique in this thesis.

Thanks to those who provided that intangible but all important moral support. To my parents especially; your visits in Texas and in New York were welcome diversions from lab work. I'm glad you were there for those times when I wanted to quit but you kept me going. Thanks, I'm not sure I would have finished if it wasn't for your encouragement.

Lastly, to Paolomi; I love you so much. You led me out of the lab to enjoy all that is NYC while at the same time putting up with my lab addiction. Your love and encouragement helped me make it through those last months of my PhD. Thank you sweetheart!

1

Introduction

1.1 The importance of interfaces

Interfaces are a ubiquitous and important part of nature connecting two separate and distinct materials to each other giving rise to unique electronic, chemical and physical properties not found in the bulk of either material. Examples include surface tension at the interface between air and water, the catalytic activity of platinum in a catalytic converter at a gas-solid interface and surface states at a semiconductor-vacuum interface. Even though these effects occur within a few atomic layers they can dominate the behavior of the system[1].

This is especially true for the omnipresent electronic devices that pervade our modern world. As demand for smaller, faster and more efficient devices increases so does the importance of the material interface. Whether it is a metal making contact to a transistor or an organic donor-acceptor interface, charges need to move from one material to another across an interface. Interaction between atoms at a boundary between materials necessarily creates states that do not exist in the volume of either material (Fig. 1.1). These states may trap charge carriers and therefore, be detrimental to device performance. Or, they may actually aid charge separation such as charge transfer states in organic solar materials and, consequently, are integral to a functioning device.

New generations of photovoltaic devices require exquisite surface control to function properly. A hot electron solar cell (Fig. 1.2a), for example, operates on a principle where electrons are extracted though selective energy contacts before thermalizing with the lattice minimizing losses

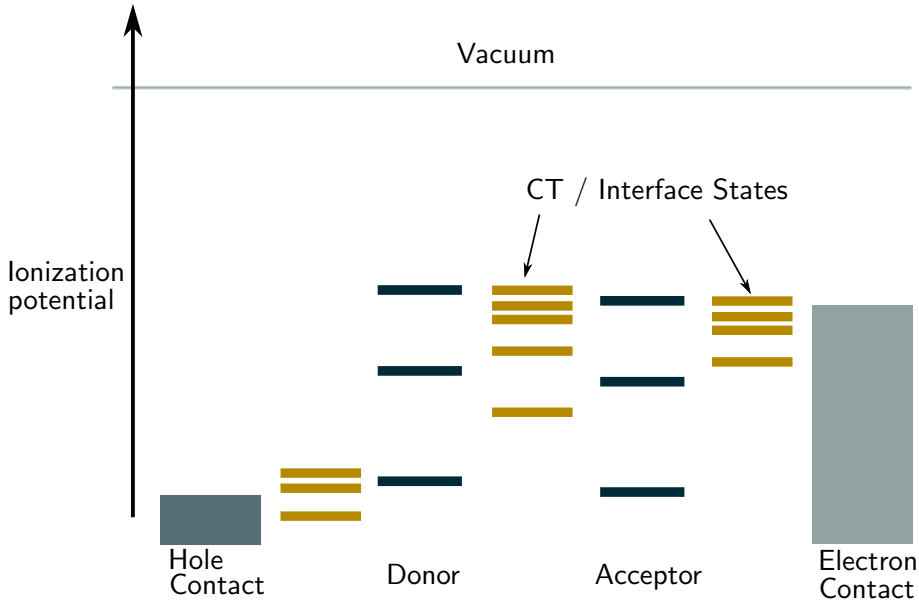

Figure 1.1: Representation of a simple device involving a two contacts and a donor and acceptor. Charge transfer and interface states are indicated by gold lines.

due to electron cooling. Capturing this otherwise wasted energy increases solar cell efficiency from 33 % for a single junction cell[2] to 66 %[3]. Creating a solar cell of this type is difficult partly because the energetic location and bandwidth of the contacts must be precise while simultaneously ensuring that no other competing pathways exist. Multiple carrier generation in a photovoltaic device can increase efficiency to 45 %[4]. One type of particular interest is a multiple carrier generation based on a process known as singlet fission (Fig. 1.2b). In this case an organic molecule absorbs high energy photons creating a singlet excited state. The singlet undergoes a process known as singlet fission to become two triplet charge carriers at half the singlet energy. The triplet pair is then extracted to another absorbing layer with a band gap near the triplet energy. Again, utilizing higher energy photons to create electrical current. With this process it is critical that the charge transfer process proceed after single fission which requires a probe sensitive to charge transfer.

Next generation solar cell concepts have been around for many years but no highly efficient cells have been developed which take advantage of these designs. This is partly because of the difficulty in engineering these devices but also because of the lack of techniques that can specifically probe buried interfaces with the time and frequency resolution necessary to measure charge transfer

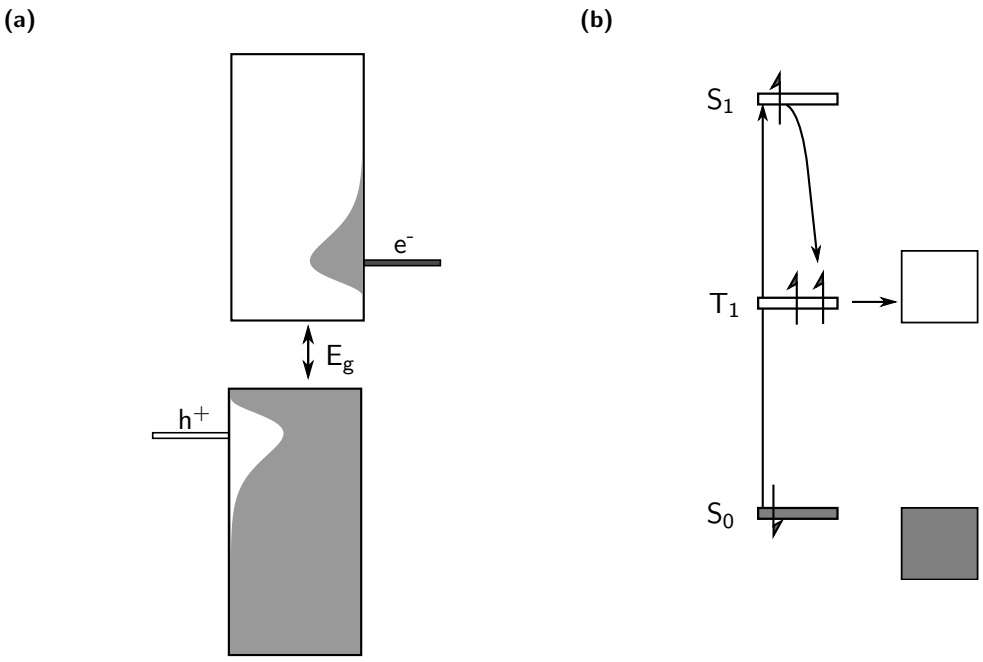

Figure 1.2: Two types of third-generation solar cells. Figure 1.2a is a depiction of the operating principle of a hot electron solar cell with band gap E_g and selective energy contacts for electrons and holes. Figure 1.2b is a depiction of a type of multiexciton generation called singlet fission and extraction of those charges.

process at interfaces. Techniques which can make measurements at buried interfaces on time scales relevant to charge transfer and singlet fission will give much needed insight to guide the design of the next generation photovoltaics.

A class of techniques which have been instrumental in increasing our understating of fundamental surface science are ultra high vacuum (UHV) techniques. Surface structure is determined by measuring the spacial distribution of reflected electrons from a surface. Electronic states are measured with the photoelectric effect and reveal direct information about the energy and momentum of occupied electronic states. When photoelectron spectroscopies are coupled with ultrafast lasers in a pump-probe geometry, electron dynamics of the surface can be studied on femtosecond time scales. Since these methods involve measuring the kinetic energy of electrons they are highly sensitive to scattering and therefore need UHV. Working under these conditions precludes studies of buried interfaces and measurements at ambient pressures. However, these are precisely the conditions under which most devices operate creating the need for new methods that overcome these

limitations.

Optical techniques are ideally suited to measure buried interfaces in all conditions and are limited only by the optical transparency of the medium under investigation. These methods can be broken down into linear and nonlinear surface methods. The difference between them is the degree with which the driving field polarizes the material. For field strengths which are large but still smaller than atomic electric fields (see section 3.1) the polarization can be expanded as a power series in the applied field as

$$P^{(tot)} = \epsilon_0 \left(\chi^{(1)} \cdot E + \chi^{(2)} \cdot E \cdot E + \chi^{(3)} \cdot E \cdot E \cdot E + \cdots \right). \tag{1.1}$$

The driving electric field is E and $\chi^{(n)}$ is the n^{th} order susceptibility with $n = 1$ termed linear and $n > 1$ referring to nonlinear susceptibilities. The resultant is the total polarization in the material, $P^{(tot)}$.

Linear optical methods have provided understanding of surface growth and electronic structure mainly through reflectance anisotropy data. Many of the linear techniques, however, suffer from absorption or emission from the bulk which masks information from the interface[5]. Nonlinear spectroscopies based on even orders in the applied field are forbidden in the volume of a material with inversion symmetry and therefore have unique sensitivity to surfaces and interfaces (see section 3.3.2) where inversion symmetry is necessarily broken. Even if the material does not have inversion symmetry, bulk contributions can be minimized by carefully choosing the polarization of the driving electric fields as well as the crystal orientation in order to minimize bulk contributions.

To attain large electric field strengths required for nonlinear spectroscopies pulsed lasers are often used. Over the past 50 years state of the art pulsed lasers have now become commercially available providing pulses nearly as short as the optical period of their carrier wave[6]. These sources provide high temporal resolution for ultrafast events and also sustain bandwidths on the order of 100 meV or greater. This can be taken advantage of for nonlinear spectroscopies to resolve spectral changes on ultrafast time scales. While ultrafast nonlinear spectroscopies are useful their interpretation can be far more difficult. Unlike photoelectron spectroscopies which directly measure single particle energies, spectroscopies only measure macroscopic polarization induced by an incident

electric field. This difference may seem subtle but can make data interpretation much more difficult usually requiring spectroscopic information and a theoretical model of the interaction.

1.2 Aim of this thesis

This thesis will focus on a second-order nonlinear optical technique called second harmonic generation (SHG) as a surface sensitive probe for measuring electric fields and states at buried interfaces with applications to charge transfer. The aim of this research is to extend the use of ultrafast pump-probe SHG as a more general and, ultimately, more informative time-resolved spectroscopy by simultaneously measuring spectral intensity and phase as a function of pump-probe delay. Previous time resolved SHG (TR-SHG) experiments have observed charge transfer at interfaces[7–9] and interpreted an increase in signal as charge transfer, however, multiple contributions can contribute to changes in the SH intensity and whether the signal increases or decreases is highly dependent on the amplitude and phase of the components contributing to the overall SH signal. While previous assumptions have been made on the effect of SH phase on the signal in an organic bilayer[9], no direct measurement of the phase was made to validate the assumption.

Only when the probe beam is far from one or two photon resonances can it be assumed that there is no phase shift contributing to the overall signal. However, as mentioned above, new states emerge at interfaces that may not be apparent in either material alone so one cannot be certain that the condition of 'far from a resonance' is met without information of the interface spectrum. Furthermore, it must also be assumed that there is no initial inter-facial electric field as a change in the electric field direction would correspond to a 180 degree phase shift as well. There is also a phase relationship between the static and pump-induced SHG that can result in an unexpected signal. The work presented here will measure interface SH spectra and phase shifts from an inorganic surface and organic-inorganic bilayers and by doing so determine the relationship between pump-induced and static SHG. This is accomplished by extending an amplitude and phase retrieval technique for second harmonic spectra pioneered by Wilson *et al.*[10, 11] to the time domain.

1.3 Organization of the thesis

Since the content of this thesis is at the interface of nonlinear optics and surface science the following two chapters will serve as an introduction to solids and nonlinear optics respectively and introduce concepts that are important for the rest of the thesis. Chapter 2 covers the basics of solids and the consequences of forming a surface. The basics of nonlinear optical spectroscopy from both a time domain and frequency domain representation are discussed in chapter 3. This will give the reader a background in the concepts used in the research, hopefully from a fresh perspective not usually encountered in the analysis of time-resolved SHG experiments.

Chapter 4 will introduce the phase resolved technique for measuring the time dependent amplitude and phase of second harmonic emission using Fourier transform spectral interferometry. In this chapter spectral interferometry will be introduced and the algorithm for the extraction of the amplitude and phase will be presented, tested and discussed. A preliminary demonstration of this technique to the oxidized Gallium Arsenide (GaAs) surface and the organic-inorganic interface between copper phthalocyanine (CuPc) and GaAs will be presented in chapter 5. Future directions and applications to further the current work will be introduced in chapter 6 inspiring investigation on the uses of this technique and how it may be useful for surface and interface problems.

References

1. Somorjai, G. a. & Li, Y. "Impact of surface chemistry." *Proceedings of the National Academy of Sciences of the United States of America* **108,** 917–24 (2011).

2. Shockley, W. & Queisser, H. J. "Detailed balance limit of efficiency of p-n junction solar cells." *Journal of Applied Physics* **32,** 510 (1961).

3. Ross, R. T. & Nozik, A. J. "Efficiency of hot-carrier solar energy converters." *Journal of Applied Physics* **53,** 3813–3818 (1982).

4. Hanna, M. C. & Nozik, A. J. "Solar conversion efficiency of photovoltaic and photoelectrolysis cells with carrier multiplication absorbers." *Journal of Applied Physics* **100,** 074510 (2006).

5. McGilp, J. F. "Optical characterization of semiconductor surfaces and interfaces." *Progress in Surface Science* **49,** 1–106 (1995).

6. Kärtner, F. X., Ippen, E. P. & Cundiff, S. T. (eds Ye, J. & Cundiff, S. T.) 54–77 (Springer US).

7. Tisdale, W. A. *et al.* "Hot-Electron transfer from semiconductor nanocrystals." *Science* **328,** 1543–1547 (2010).

8. Jailaubekov, A. E. *et al.* "Hot charge-transfer excitons set the time limit for charge separation at donor/acceptor interfaces in organic photovoltaics." *Nature Materials* **12,** 66–73 (2013).

9. Kaake, L. G., Jailaubekov, A., Williams, K. J. & Zhu, X.-Y. "Probing ultrafast charge separation at organic donor/acceptor interfaces by a femtosecond electric field meter." *Applied Physics Letters* **99,** 083307 (2011).

10. Wilson, P. T., Jiang, Y, Aktsipetrov, O. a., Mishina, E. D. & Downer, M. C. "Frequency-domain interferometric second-harmonic spectroscopy." *Optics Letters* **24,** 496–498 (1999).

11. Wilson, P. T., Jiang, Y., Carriles, R. & Downer, M. C. "Second-harmonic amplitude and phase spectroscopy by use of broad-bandwidth femtosecond pulses." *Journal of the Optical Society of America B* **20,** 2548 (2003).

2

Semiconductor Surfaces and Interfaces

God made solids, but surfaces were the work of the Devil

— Wolfgang Pauli

Two objectives of this thesis are to measure inter-facial states and electric fields. Semiconductors are an excellent model system because they exhibit both localized surface states as well as inter-facial electric fields in what is known as the space charge region. This chapter will review the conceptual framework used to understand surfaces and their electronic structure. Bulk and surface properties are examined with two different but complementary frameworks: the nearly free electron approach and the tight binding approach. Both will demonstrate the effect of truncating a crystal and states localized at the surface which are formed as a result. Finally, the effects of charged surface states on surface electric fields in semiconductors is reviewed. This chapter is only meant to highlight the difference between bulk and surface structure. Entire books have been written about solid state and crystal surfaces. More information on bulk properties of crystals can be found in a variety of textbooks[1–3]. In depth discussion of surfaces and conventional techniques used to investigate them are provided in Lüth[4].

2.1 Bulk and surface electronic structure

This section covers two models which approach bulk and surface structure from the two extremes of nearly free electrons and tightly bound electrons. Both methods give similar results and provide insights into the physical phenomena that cause crystals to form states at their surface when they are terminated. These methods also provide insights into why these states often occur within the band gap of a material. The first two sections are restricted to a one dimensional treatment for simplicity but the last section extends the 1-D concepts to a more realistic treatment of 3-D crystals and their surfaces.

2.1.1 The nearly free electron case

Crystals have greater than 10^{22} atoms per cm^3, making a theoretical treatment in real space a daunting task. This problem is greatly simplified by taking advantage of the crystal structure and moving the calculations into reciprocal space. Here a monoatomic chain of atoms is used to provide a simple illustration of the band structure and the effect of a surface within the nearly free electron approximation. The chain is truncated at $z = 0$ which represents the crystal vacuum interface. For $z < 0$ the crystal has a periodic potential $V(z) = V(z+na)$ where n is an integer and a is the lattice constant. For $z > 0$ the potential is the vacuum potential, $V(z) = V_0$. Fig. 2.1a is a representation of the potential energy landscape for an electron in the crystal. It is assumed that the perturbing potential, $V(z)$, is weak to allow for the nearly free electron approximation. Our main task is to solve the Schrödinger equation on either side of the boundary and match the wavefunctions and their first derivatives at the boundary, $z = 0$.

Solving for the eigenvalues of the Schrödinger equation as a function of the wave vector for a region deep inside the crystal, we recover the bulk dispersion. These values are plotted over the extended Brillouin zone in Fig. 2.1b. The graph is displayed as a function energy, E, vs. reciprocal distance or wave vector k_z. These values provide an index for the electron energy and have the meaning of available states at a given energy. At small values of k_z, the electron energies follow the free electron energies, $\frac{\hbar^2 k^2}{2m}$. As k_z increases to $\frac{\pi}{a}$, at the Brillouin zone boundary, the energy values

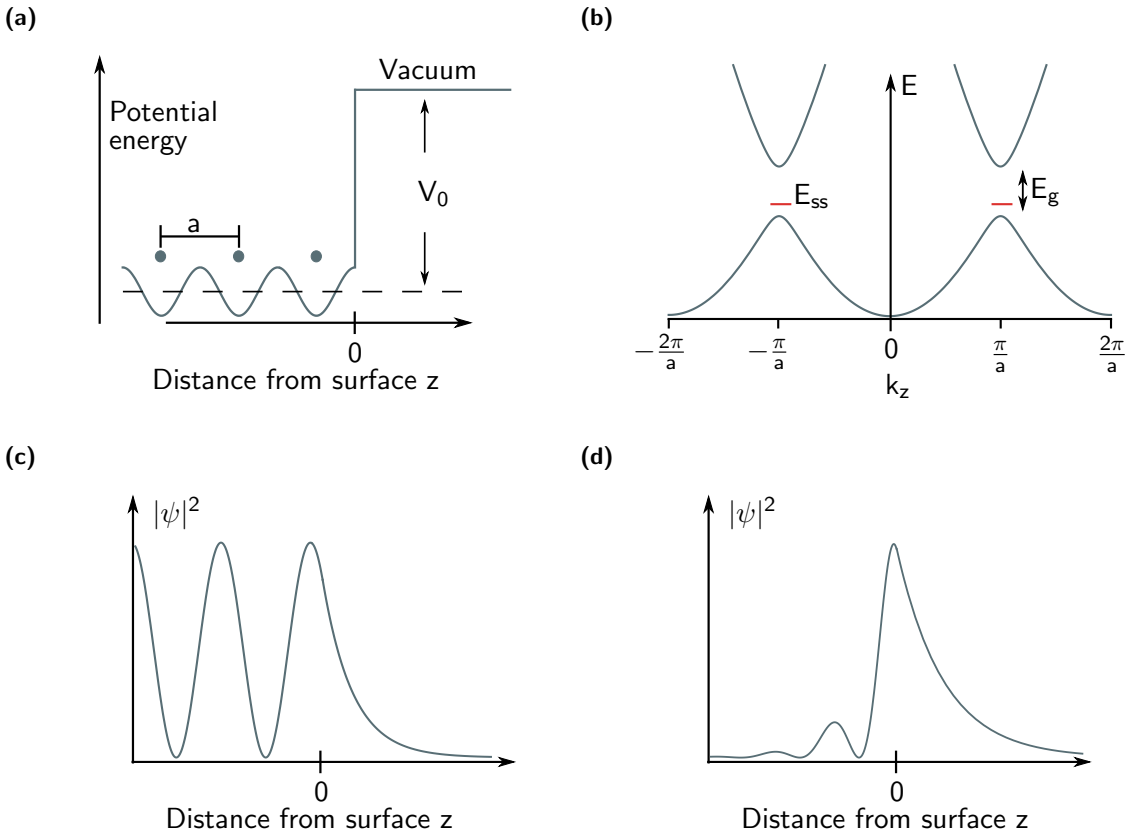

Figure 2.1: Nearly free electron model of an electron moving in crystal with lattice constant, a, modeled using a cosine potential (2.1a). Band structure for the simple linear chain for $z \ll 0$ with band gap E_g. Superimposed on the band structure is a localized surface state E_{ss} (2.1b). Probability density of a bulk (2.1c) and surface (2.1d) state. *Adapted from [4].*

deviate from a perfectly free particle and a band gap opens indicated by E_g on the graph in Fig. 2.1c.

In addition to finding the energy values we can also find the wave functions propagating in the k_z direction. Eventually the wave function will arrive at the surface and will decay exponentially into the vacuum provided the energy is below V_0 (Fig. 2.1b). This wave function represents a bulk derived state which has similar amplitude at the surface as in the bulk. The presence of a surface allows for new solutions to the Schrödinger equation not allowed in the bulk. At the surface the bulk derived wave function decays exponentially into the vacuum. The presence of the surface can also allow for the existence of new states that are not part of the bulk band structure.

Imaginary values of wavevectors are forbidden within the bulk of a crystal because the wave-

function would increase to infinity but the wavefunction must be normalizable so these solutions cannot exist in the bulk. At a surface this restriction is relaxed and imaginary values of k are allowed while the normalizability restriction still holds. An example of such a state is shown in Fig. 2.1d. At $z < 0$ the wavefunction increases exponentially to the surface and then decays exponentially at $z > 0$ into the vacuum. At $z = 0$ both the left and right side of the wavefunction must have the same value and slope. These conditions restrict the possible wavefunctions and energies at the surface allowing for only a single surface state within the band gap. The energy of this surface state is within the forbidden bulk band gap and is known as a Schockley state[5].

This simple treatment demonstrates how the addition of a surface gives rise to additional states within the band gap. One of the primary goals of this research is to investigate these states. The treatment presented above is limited to perfectly clean and cleaved surfaces, but completely neglects the atomic nature of the surface and unsatisfied valencies that arise from broken bonds at a crystal surface or interface. A more intuitive approach is the tight binding approach introduced in the following subsection.

2.1.2 Tight-binding picture for crystals and surfaces

The tight binding model provides a qualitative picture that may be more intuitive to the chemist since the connection between real space and reciprocal space is more apparent. In this model only the frontier orbitals participate in bonding and only the on site and nearest neighbor interactions contribute. Tight-binding has been particularly successful for calculating surface energetics and band structure of semiconductor surfaces[6]. The covalent character of the bonding in semiconductors makes the tight-binding approach a superb fit for calculating their properties. Because of its usefulness and physical insight a brief introduction to the tight-binding theory is presented in this section. More detailed conversations can be found in books and papers by Roald Hoffman [7–9] and Chadi [10].

The tight-binding model represents the opposite extreme of the nearly free electron model where instead of electrons being free to move about the lattice they are bound loosely to the parent atom. Tight-binding is essentially a modified version of linear combination of atomic orbitals

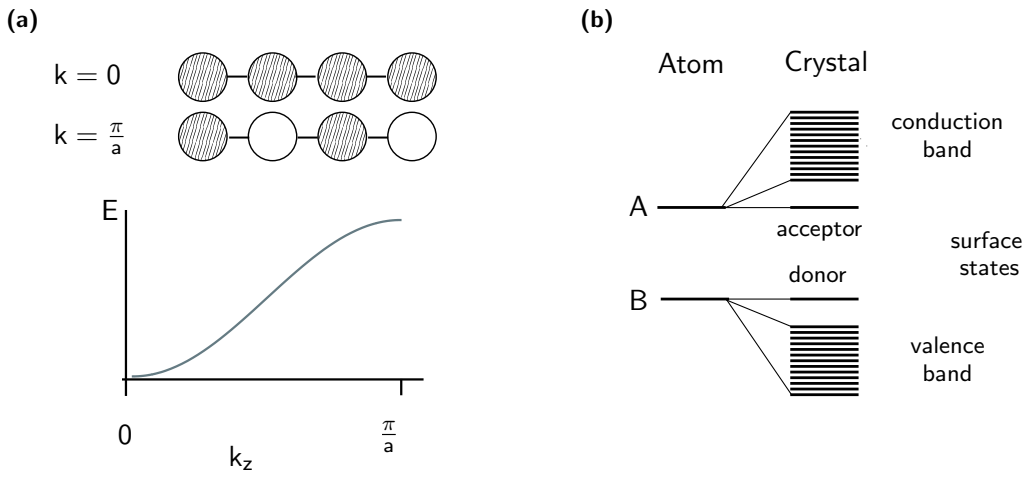

Figure 2.2: Tight-binding picture of crystal band structure illustrated using a 1-D chain of S-orbitals (2.2a). Truncation of the chain leaves dangling bonds at the surface whose energies are nearer the atomic orbital energies creating in-gap surface states (2.2b).

(LCAOs) used to treat many molecular systems. The main difference is that we are looking at a periodic structure with many atoms, on the order of Avagadro's number, 10^{23}. In this situation there are a vast number of energy levels also on the order of Avagadro's number and instead of having bonding or antibonding character, as in a molecule, there is a continuum of different energies. An illustration of this idea using a hypothetical 1-D material comprised of S orbitals is presented in Fig. **??**. For S orbitals at wave vector $k = 0$ all of the orbitals are in phase corresponding to a bonding orbital or 0 nodes in the wavefunction. At $k = \frac{\pi}{a}$, the Brillouin zone boundary, all of the orbitals are out of phase and this has antibonding characteristics or one node for each atom in the unit cell. The large number of atoms allows for a different number of nodes between these two extremes and gives rise to a continuously varying energy with k, also known as the band structure. An example of the band structure for a one-dimensional infinite chain of S-orbitals is given in Fig. 2.2a.

When the chain is finite we again have the same problem as in the nearly free electron approach. Within the tight-binding framework, however, it is easier to see where these states arise from and what their nature will be. In Fig. 2.2b two atomic levels, A and B, combine to comprise the conduction and valence band of the crystal respectively. At the surface the atoms have fewer

bonding partners than in the bulk leading to energy levels that are closer to those of the free atom. This, in turn, leads to in-gap states localized at the surface. The separation of these states from the bulk valence and conduction bands depends on the perturbation caused by the surface. For sp^3 hybridized orbitals found in Si, Ge, GaAs, InAs, GaP, and many more, the surface often represents a significant deviation from the bulk bands. Surface states derived from state A take on acceptor character and the states derived from state B have donor character. A simple example is GaAs(100) whose surface consists of both Ga and As atoms. The conduction band has a primary contribution for the Ga atoms and the valence band is primarily composed of orbitals from the As atoms. Surface states on GaAs derived from As have donor character and those derived from Ga states have more acceptor character.

2.1.3 Bulk states and surface states in 3-D crystals

So far all of the examples have been one dimensional chains of atoms that were eventually truncated in the z direction. Since we live in a 3-D world and crystals have properties which depend on crystallographic direction, we need to consider some basics of 3-D crystals. The concentration will be on 3-D crystals with zinc-blend structures since this is the same structure as GaAs, the material of focus in this thesis.

Previously within the tight-binding picture we found that, k, is a wavevector and counts nodes. Additionally, k indicates the symmetry directions for 2 and 3 dimensional materials. The first Brillouin zone of a zinc-blend crystal is displayed in Fig. 2.3. The labeled lines and points indicate directions of high symmetry which have cryptic labels that have become convention. Points and lines inside of the first Brillouin zone are labeled with capital Greek letters while those on the surface of the Brillouin zone are marked with capital Roman letters. The center point of Brillouin zone is termed the gamma, Γ, point at $k = (0, 0, 0)$. Energies along high symmetry points are calculated and displayed in the band structure (2.3b). For example, taking a cut from Γ along Δ to X corresponds to the real space [100] direction and is plotted in figure 2.3b. Similarly, the other labels on the x-axis of figure 2.3b represent the energies along different cuts through the high symmetry points labeled in figure 2.3a This is analogous to the 1-D case but now k also represents

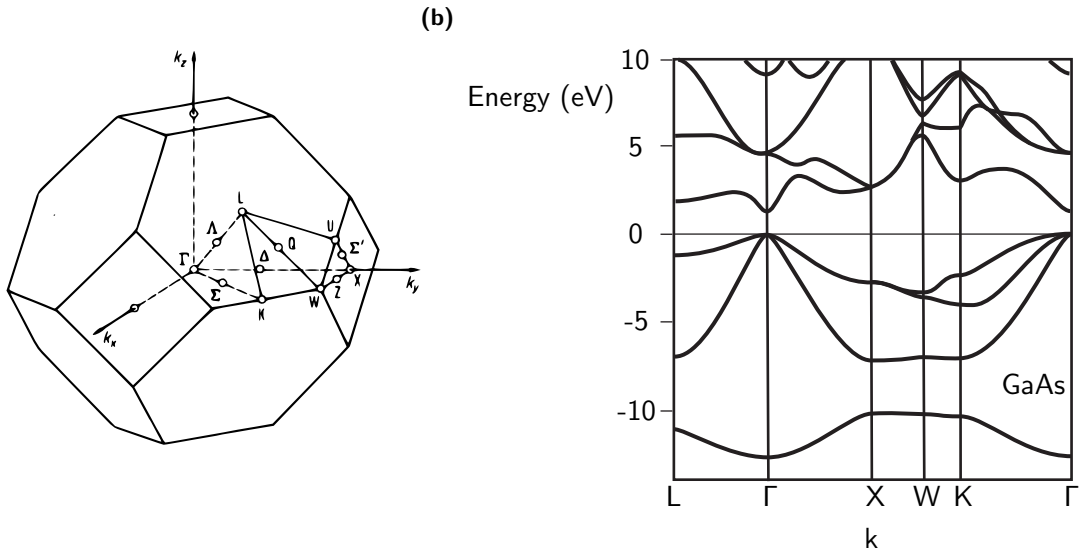

Figure 2.3: First Bruillion zone for a zinc blend crystal (2.3a) along with the bulk band structure for a prototypical zinc blend material, GaAs, calculated with the tight-binding model (2.3b). The top of the valence band is set to 0 eV. *Band structure adapted from Ref. [11]*

the symmetry labels along crystal directions. Though the band structure seems complicated, it is only a combination of many one dimensional cuts through the Brillouin zone at high symmetry points which correspond to different real space crystal directions.

As we have seen for the 1-D cases above, the surface is different from the bulk. When a crystal is truncated along the z direction it forms a surface plane which can be described in the same manner as the bulk using wave vectors to label the continuous states in the surface plane. Perpendicular to the surface there are states within the band gap similar to those in the 1-D case. In the surface plane, however, these surface states can be delocalized in the surface plane which gives rise to a surface band structure that contains both bulk bands projected onto the surface and new states arising from the termination of the surface. Usually this projected surface band structure, as it is known, has a different labeling convention than the bulk band structure. An example of a surface band structure is shown in Fig. 2.1c where $k_\perp$ is the same as k_z in our 1-D treatments and the axis labeled $k_\parallel$ is the wave vector parallel to the surface. Shaded regions represent the bulk bands that have been projected onto the surface. Dotted lines indicate states that are unique to the surface and have some dispersion in the plane of the material. When the dotted lines cross the

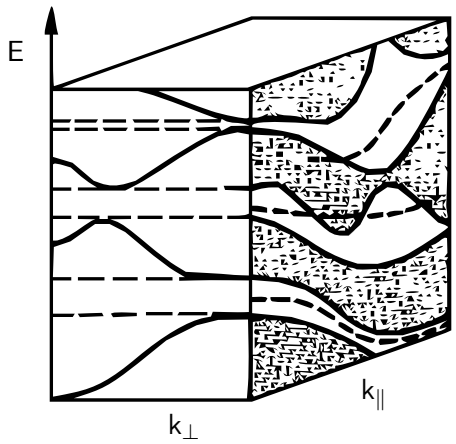

Figure 2.4: Hypothetical band structure containing both $E(k_\perp)$ and $E(k_\parallel)$. Shaded regions represent the bulk band structure projected along $k_\perp$ onto the surface. Dashed lines represent the surface states localized in the $k_\parallel$ plane. Solid lines indicate bulk bands. *From Ref. [4]*

bulk band structure the surface states are said to be in resonance with a bulk band. This means that, while there is still probability amplitude of the surface state at the surface, the state also has probability amplitude extending throughout the bulk of the crystal. These are called surface resonances.

Surface band structure can be indicated more clearly by taking a definite example of an unreconstructed GaAs(100)(1x1) surface. Similar to the bulk case we have the center of the zone labeled Γ and high symmetry directions labeled J, K and J$'$ (Fig. 2.5), which correspond to real space directions [011], $[0\bar{1}0]$ and $[0\overline{11}]$. Surface band structure for the unreconstructed surface is illustrated on the right side of Fig 2.5. The bulk projected bands onto the (100) surface are the shaded regions while the surface bands are illustrated as solid lines. As we traverse the surface Bruillion zone we can see that the surface states go in and out of resonance with the bulk band structure. Dispersive surface state bands arise because energy values are functions of $k_\perp$ and $k_\parallel$ so the matching of the wave function at the boundary depicted in Fig. 2.1d needs to be repeated for every value of $k_\parallel = k_x, k_y$. This leads, in general, to different energies for different values of $k_\parallel$. In addition, states derived from the bulk are also present at the surface (Fig. 2.5) so care must be taken when considering true surface states.

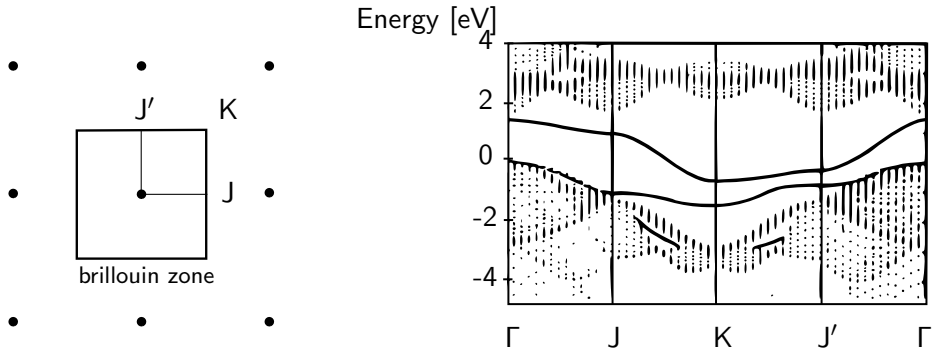

Figure 2.5: Surface Brillouin zone and corresponding calculated band diagram of a 1x1 surface of gallium arsenide. Band structure from reference [12].

2.2 Space charge region at semiconductor interfaces

As mentioned in the previous, section when a surface is formed there are unsatisfied valencies described as dangling bonds which can localize charges at the semiconductor surface. These surface states can carry either a positive or negative charge depending which atom they originated from and whether they are occupied or unoccupied. The low carrier density in semiconductors means that this surface charge is screened over very large distances relative to atomic distances which leads to charge redistribution near the surface forming an area known as the space charge region.

Referring back to Fig. 2.2b we see that atom A comprises the conduction band of the material and atom B the valence band. Surface states arising from unsatisfied valencies from atom A will become negatively charged when they are filled whereas states derived from atom B have will be positively charged when they are unfilled. The charging character of dangling bond states are summarized in table 2.1.

	occupied	empty
surface donors	0	+
surface acceptors	−	0

Table 2.1: Charging character of surface states.

The occupancy of these states generally depends on the energetic location of the Fermi level at the surface. The surface Fermi level can be determined by taking into account the charge neutrality condition at the surface. This means that charge at the surface resulting from either atom A or B, Q_{ss}, must be balanced by an opposite charge inside the semiconductor. This compensating charge is termed the space charge, Q_{sc}. Total charge neutrality requires that $Q_{ss} = -Q_{sc}$.

Real surfaces typically have a combination of donor and acceptor states at the surface. However, for illustrating the basic principles and effects of the space charge region we will consider donor and acceptor states separately. Application to more complex surfaces are straight forward.

An illustration of band bending at an n-type semiconductor surface with only acceptor states is given in Fig. 2.6. The reason for band bending can be explained as follows. Inside the bulk of the material, the Fermi level is determined by the bulk doping density of the material. For an n-type semiconductor this means the bulk donor level which is depicted in Fig. 2.6. Acceptor states are formed due to the presence of the surface and unsatisfied valencies of atoms comprising the conduction band. Their energetic position is related to the inter-atomic potentials and are therefore fixed. In the limit of a flat band condition all of the acceptor states are filled and a large amount of charge builds up at the surface which must be compensated for in the bulk. This is an energetically unfavorable situation for the semiconductor surface and is unstable. Consequently, the conduction and valence bands in the near surface region deform such that the Fermi level crosses the surface acceptor states resulting in a decreased surface charge density Q_{ss}. Inside the crystal near the surface region the band bending moves the bulk donor levels above the Fermi level which causes the donors to become ionized creating a Q_{sc} of opposite sign and equal in magnitude to Q_{ss}.

The curvature in the bands induced by the surface charge causes the conduction band electrons to move away from the surface and holes to move toward the surface. This is termed a depletion layer. Two other situations may also be present at a semiconductor surface. First, if the surface state density is sufficiently high then the band bending can become so extreme that the valence band and surface states cross forming an inversion region. Second, if donor states are sufficiently high in energy and are ionized they leave the surface positively charged. In order to compensate for this extra surface charge, electrons are drawn to the surface and create what is called an accumulation

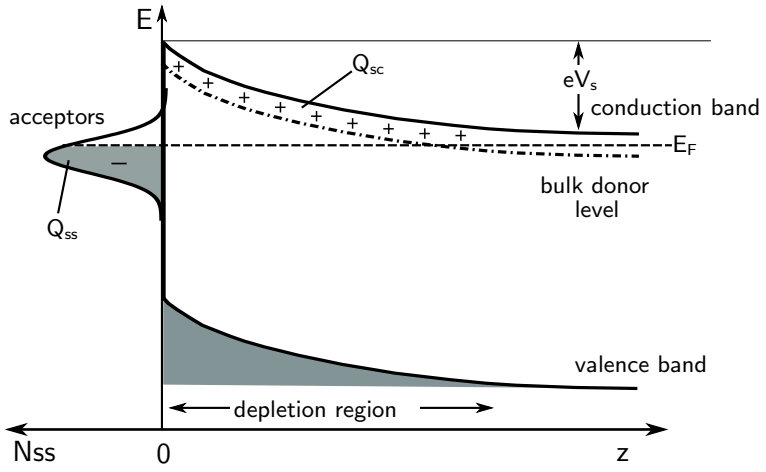

Figure 2.6: Energy of electronic bands versus the surface normal coordinate, z, with the surface set at z=0, for an n-type semiconductor with a depletion region. Gaussian acceptor states with density N_{ss}, are partially occupied. The charge induced by the surface states, Q_{ss} is compensated for in the bulk by the space charge, Q_{sc}. The Fermi level is indicated by E_F and the total bending of the bands is indicated by eV_s with e indicating the value of an elementary charge.

layer. Unlike the previous two cases the accumulation layer is not balanced by bulk donors but by conduction band electrons.

The magnitude of the band bending along with its depth can be solved using Poisson's equation:

$$\frac{d^2V(z)}{dz^2} = -\frac{\rho(z)}{\epsilon\epsilon_0} \tag{2.1}$$

Usually a single direction z is sufficient for determining surface band bending. The previous details concerning an n-type semiconductor can easily be applied to a p-type semiconductor. Only the signs of the charges need to be reversed. Then instead of an upward bending band there would be a downward bending band.

This research is concerned with the ultra-fast dynamics of electric fields. Therefore we should be able to predict how the space charge field changes when the semiconductor absorbs light. Upon absorption of light electron-hole pairs are formed. In most inorganic semiconductors, exciton binding energy is less than the thermal energy of the environment. Therefore, the exciton spontaneously separates into a free electron-hole pair. Electrons move to lower energy positions in the conduction band away from the surface while holes move towards the surface following the curvature of the space charge region. At large enough densities these photo excited carriers screen the surface charge

resulting in an overall decrease in the magnitude of the space charge field on time scales ranging from femtoseconds to picoseconds[13, 14].

The overall purpose of this thesis is to develop a method for taking time and spectral resolved data of the amplitude and phase of the second harmonic (SH) signal. These data would be rather uninformative if there were no spectral features to be observed. Surfaces states may display an increase in SH signal are ideal for spectroscopic SH measurements. We also wish to track the ultrafast dynamics of electric fields at interfaces. Since we already know that there is a space charge field present at the surface of most semiconductors they provide an ideal platform to study the evolution of electric fields in a controlled manner. The following chapter seeks to lay down a theoretical framework from which we can interpret our time-resolved second harmonic spectra.

References

1. Ashcroft, N. W. & Mermin, D. N. *Solid state physics.* 1st ed. (Thomson Learning, Toronto, 1976).
2. Kittel, C. *Introduction to Solid State Physics.* 6th (John Wiley & Sons, Inc., New York, 1986).
3. Madelung, O. *Introduction to solid State Theory* (Springer Berlin Heidelberg, 1978).
4. Lüth, H. *Surfaces and Interfaces of Solids.* (Springer Verlag, 1993).
5. Shockley, W. "On the surface states associated with a periodic potential." *Physical Review* **56,** 317–323 (1939).
6. Goringe, C. M., Bowler, D. R. & Hernández, E. *Tight-binding modelling of materials.* 1999.
7. Hoffmann, R. "A chemical and theoretical way to look at bonding on surfaces." *Reviews of Modern Physics* **60,** 601–628 (1988).
8. Hoffmann, R. "A chemical and theoretical way to look at bonding on surfaces." *Reviews of Modern Physics* **60,** 601–628 (1988).

9. Glassey, W. V. & Hoffmann, R. "Band structure representations of the electronic structure of one-dimensional materials with helical symmetry." *Theoretical Chemistry Accounts* **107,** 272–281 (2002).

10. Chadi, D. J & Cohen, M. L. "Tight-binding calculations of the valence bands of diamond and zincblende crystals." *physica status solidi (b)* **68,** 405–419 (1975).

11. Rohlfing, M., Krüger, P. & Pollmann, J. "Quasiparticle band-structure calculations for C, Si, Ge, GaAs, and SiC using Gaussian-orbital basis sets." *Physical Review B* **48,** 17791–17805 (1993).

12. Larsen, P., Veen, J. V. D., Mazur, a & Pollmann, J. "Surface electronic structure of GaAs(001)-(2x4): Angle-resolved photoemission and tight-binding calculations." *Physical Review B* **26** (1982).

13. Dekorsy, T., Pfeifer, T., Kütt, W. & Kurz, H. "Subpicosecond carrier transport in GaAs surface-space-charge fields." *Physical Review B* **47,** 3842–3849 (1993).

14. Tomita, Y. & Ishii, H. "Dynamics of photoexcited carriers and space-charge field by picosecond two-beam excitation in photorefractive semiconductors." *Japanese Journal of Applied Physics, Part 1: Regular Papers and Short Notes and Review Papers* **33,** 1892–1898 (1994).

3

Second-Order Nonlinear Optics

In order to observe surface states and interfacial electric fields present at surfaces and interfaces we will need to develop a framework we can use to approach data interpretation and analysis. Since our pump-probe experiment will collect information in both time and frequency domains, we must first understand how we can represent this experiment mathematically using the framework of nonlinear optics in both representations. This chapter introduces nonlinear response theory as a framework for representing nonlinear optical responses and then applies this structure to static and time-resolved second harmonic generation (SHG) experiments.

First, an introduction to nonlinear optics is presented, followed by a description of the polarization response in both the time and frequency domains. Density matrices and the interaction picture are introduced and used to understand, at a more fundamental level, the nonlinear light-matter interactions that occur in these experiments. Pictorial representations of the polarization response in the form of Feynman-like diagrams will also be introduced. Practical applications to SHG and time-resolved SHG (TR-SHG) are presented to place the overall experiments presented at the end of the thesis in context. More extensive and thorough treatment of the topics considered here are found in a variety of texts by Zanni and Hamm[1], Mukamel[2], and Boyd[1] among others.

3.1 Optical response functions and susceptibilities

To illustrate the ideas behind nonlinear optics we begin with a simple classical picture of the optical response consisting of classical electrons moving in a potential well. The interaction of light with the electrons in a dielectric material proceeds in two stages. First, the incident electromagnetic field $\mathbf{E}(r,t)$ interacts with the material which generates a polarization $\mathbf{P}(r,t)$ defined as a dipole moment per unit volume $\left[\frac{\mathrm{C}\cdot\mathrm{m}}{\mathrm{m}^3}\right]$ in the material. In the simplest picture the polarization can be viewed as a set of dipoles oscillating at the frequency of the incident radiation. This process is governed by the wave equation which, in the case of non-magnetic materials free of currents and free charges, is

$$\nabla \times \nabla \times \mathbf{E}\left(\mathbf{r},t\right) + \frac{1}{c^2}\frac{\partial^2 \mathbf{E}\left(\mathbf{r},t\right)}{\partial t^2} = -\frac{1}{\epsilon_0 c^2}\frac{\partial^2 \mathbf{P}\left(\mathbf{r},t\right)}{\partial t^2}. \tag{3.1}$$

As mentioned above $\mathbf{E}(r,t)$ and $\mathbf{P}(r,t)$ are the electric field and polarization, respectively. The permittivity of free space is ϵ_0 and c is the speed of light. The polarization on the right-hand side of the Eq. 3.1 is a source term responsible for radiating an electromagnetic wave at the frequency of the driving electric field; this is termed the linear polarization.

Nonlinearities in the polarization arise if the driving field is of sufficient intensity to drive electrons outside of their harmonic potential. We can illustrate the effects of a strong electromagnetic wave using an anharmonic potential, the Morse potential, and a simple harmonic potential as the lowest order approximation to the Morse potential (Fig. 3.1a). Weak driving fields cause the electrons to oscillate very near the equilibrium position. Comparing the Morse potential and the harmonic potential at very low displacements we see that they are nearly equivalent.

As the intensity of the driving electric field increases, electrons are driven outside of the region where the harmonic approximation is valid. In these regions the electrons no longer oscillate at a single frequency but now oscillate at many frequencies (Fig. 3.1b). While a majority of electrons oscillate at the fundamental frequency other electrons will oscillate at two, three, four, *etc.*, times the driving frequency. Though the magnitude of these oscillations are much smaller than the fundamental frequency it is still possible to detect light from oscillations of higher frequencies using suitably strong light sources and sensitive detectors[3].

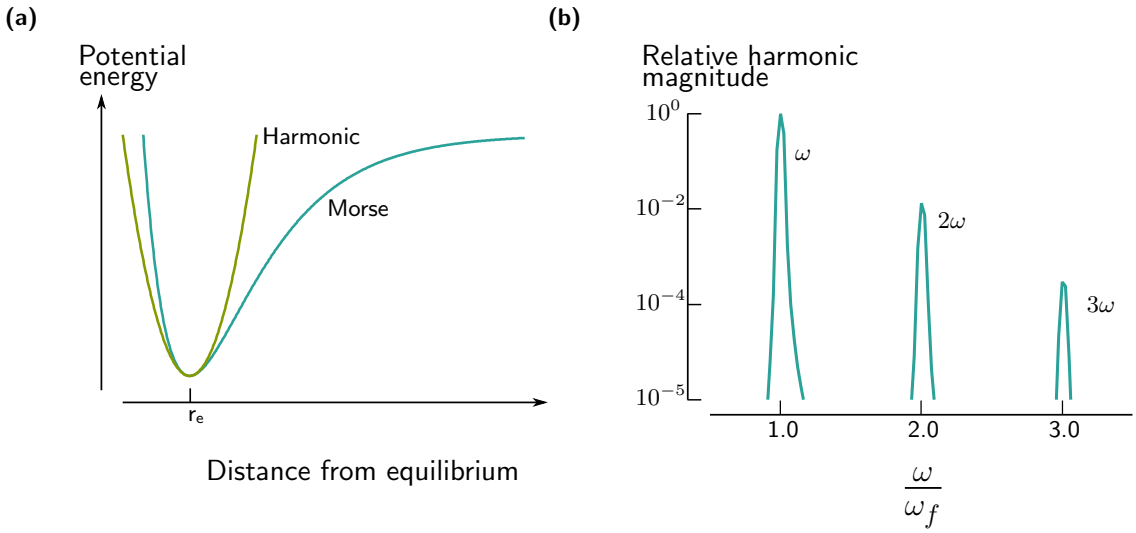

Figure 3.1: Comparison of a harmonic potential and a Morse potential (3.1a) and illustration of the resulting harmonics (3.1b) generated from electrons oscillating in a Morse potential.

In the case where there is a strong driving electric field the material polarization is expanded as a power series

$$\mathbf{P}^{(tot)}(\mathbf{r},t) = \mathbf{P}^{(1)}(\mathbf{r},t) + \mathbf{P}^{(2)}(\mathbf{r},t) + \cdots + \mathbf{P}^{(n)}(\mathbf{r},t) = \sum_{n=1}^{\infty} \mathbf{P}^{(n)}(\mathbf{r},t). \tag{3.2}$$

In expanding the polarization in terms of a power series we have made the tacit assumption that the driving field is weak compared with inter-atomic fields. That is the electric field between the electrons and the nucleus. The value of the inter-atomic electric field is on the order of 10^9 $\frac{\text{V}}{\text{cm}}$[4] which corresponds to peak intensities on the order of 10^{16} $\frac{\text{W}}{\text{cm}^2}$. For all of the experiments presented in chapters 4 and 5 the peak intensities are on the order of 10^{10} $\frac{\text{W}}{\text{cm}^2}$ which is well within the range where the power series expansion applies. These higher order polarizations represent dipole oscillations which generate harmonics of the incident polarization as illustrated in Fig. 3.1b.

A polarization of order 1 in Eq. 3.2, $\mathbf{P}^{(1)}(\mathbf{r},t)$, is the linear polarization and polarizations of order 2 or higher are referred to as the nonlinear polarization. For example, $\mathbf{P}^{(2)}(\mathbf{r},t)$ would give rise to the second harmonic of the incident wave. Once the polarization is known it is possible to solve for the outgoing field by inserting the polarization into equation 3.1. Unfortunately this only abstracts the problem to finding the polarization which is our main concern in the rest of this

section.

3.1.1 Time-domain polarization

A time-domain approach for describing the nonlinear polarization is useful when considering the interaction of short pulses, like those used in this thesis, with a material. This section examines nonlinear optics in the framework of nonlinear response theory. Using this theory it is possible to write the material polarization in terms of response functions and interactions with an electric field. To introduce the basics of response functions we begin with the linear response function of a material[5],

$$P_i^{(1)}(\mathbf{r},t) = \epsilon_0 \int_{\substack{all\\space}} d^3\mathbf{R} \int_{-\infty}^{\infty} d\tau \, R_{ij}^{(1)}(\mathbf{r},t;\mathbf{R},\tau)\, E_j(\mathbf{R},\tau)\,. \tag{3.3}$$

Equation 3.3 is the most general form of the linear response function. The response of the material is a tensor which relates the electric field at time τ and location $\mathbf{R}$ to a polarization in the material at position $\mathbf{r}$ and time t. Integration over all of space and time indicates the the polarization depends on the driving field at all other locations and times in the crystal. Another way of saying this is that the polarization of the material is "non-local" in both space and time. Most materials are also anisotropic which is why the response function is represented by a tensor relating the applied electric field vector to the polarization vector. The subscripts, ij range over the Cartesian coordinates (x, y, z), and Einstein summation convention is assumed. Eq. 3.3 is the most general form of the linear susceptibility.

Fortunately, we can make a variety of assumptions that reduce Eq. 3.3 to a more manageable form. First, we assume that the the polarization does not depend spatially on the electric field at every point in the material. This is equivalent to taking the electric dipole approximation which will be used throughout this thesis. Furthermore, insisting on time invariance and causality the polarization can be written as[5]

$$P_i^{(1)}(t) = \epsilon_0 \int_0^{\infty} dt_1 \, R_{ij}^{(1)}(t_1)\, E_j(t-t_1) \tag{3.4}$$

which is a convolution of the electric field with the response function. The quantity t_1 indicates an interval of time and $t-t_1$ indicates a time point. In the limit of an infinitely short laser pulse we can

recover the exact response function. In the limit that the pulse is shorter than any time dynamics governed by the response function the pulse can be considered effectively a delta function. This is the semi-impulsive approximation and is valid for vibrational spectroscopies. Electronic events such as polarization and transitions usually take place on the same time scales as the pulses. In this case the laser pulse obscures the dynamics of interest.

The second order polarization is a result of two fields interacting with the material. Following the linear case the second order polarization is written as

$$P_i^{(2)}(t) = \epsilon_0 \int_0^\infty dt_2 \int_0^\infty dt_1 \, R_{ijk}(t_2, t_1) \, E_j(t - t_2) \, E_k(t - t_1) \,. \tag{3.5}$$

Instead of a single interaction as in the linear case we now have two interactions with an electromagnetic field at time points $\tau_1 = t - t_2 - t_1$ and $\tau_2 = t - t_2$. This produces the second order polarization, which is responsible for sum frequency generation (SFG), difference frequency generation (DFG), and in the special case where $E_j = E_k$, second harmonic generation (SHG) and optical rectification (OR).

We can generalize these equations to the n$^{\text{th}}$ order nonlinear polarization as

$$\begin{aligned} P_i^{(n)}(t) = \epsilon_0 \int_0^\infty dt_n \int_0^\infty dt_{n-1} \cdots \int_0^\infty dt_1 \\ R_{ijk\cdots}(t_n, t_{n-1}, \cdots t_1) \, E_j(t - t_n) \, E_k(t - t_n - t_{n-1}) \cdots E_{\cdots}(t - t_n - \cdots - t_1) \,. \end{aligned} \tag{3.6}$$

A generalized diagram which relates the time intervals to time points is given in Fig 3.2. Since the pump-probe spectroscopy experiment we perform takes place in both the time and frequency domain we should also consider the frequency domain representation of the polarization.

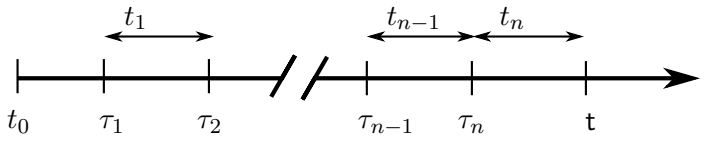

Figure 3.2: Time ordering indicated for the values of τ and t. Interaction time points are indicated by τ_n while time intervals are indicated with t_n.

3.1.2 Frequency-domain polarization

When using continuous wave lasers or pulses that are long compared to the material polarization time then the frequency domain description is more appropriate. By writing the time domain fields in terms of their Fourier transforms and performing an additional Fourier transformation of the polarization we arrive at the frequency domain representation of the linear polarization[5]:

$$P_i^{(1)}(\omega) = \epsilon_0 \chi_{ij}^{(1)}(\omega) E_j(\omega), \tag{3.7}$$

which is the more common equation involving the nonlinear susceptibility. The frequency domain susceptibility, $\chi_{ij}^{(1)}(\omega)$, is just the Fourier transform of the material response,

$$\chi_{ij}^{(1)}(\omega) = \int_0^\infty R_{ij}^{(1)}(t_1) e^{-i\omega t_1} dt_1 . \tag{3.8}$$

The second order nonlinear susceptibility can be transformed, albeit with a little more effort, to yield

$$P_i^{(2)}(\omega) = \epsilon_0 \chi_{ijk}^{(2)}(\omega) E_j(\omega_1) E_k(\omega_2) . \tag{3.9}$$

It is important to note that these frequency domain representations contain real and imaginary parts which correspond to a signal with amplitude and phase and is important in time-resolved SHG spectroscopy in chapters 4 and 5.

3.2 Quantum mechanics of the nonlinear response

So far we have only discussed the polarization in terms of electromagnetic fields interacting with a material response function. All of the details of the actual material, however, are hidden in the linear and nonlinear response functions. This section introduces density matrices to describe light-matter interactions and reaches a point where we can describe linear and nonlinear responses as perturbations to the system caused by the electric field and the dipole operator on the density matrix. Moreover, a pictorial representation using Feynman-like diagrams will better illustrate the nonlinear interactions taking place in both static and time-resolved SHG.

3.2.1 The density matrix

We begin where we left off in section 3.1.1 with a description of the polarization in a material which consists of n-number of electric fields interacting with an n^{th} order response function to produce the n^{th} order polarization (Eq. 3.6). Macroscopic polarization is related to the microscopic crystal properties by the expectation value of the time-dependent density matrix, $\rho(t)$, with the dipole moment for emission, μ, which is written as

$$P(t) = \langle \mu\rho(t) \rangle \equiv \mathrm{Tr}\left(\mu\rho(t)\right), \tag{3.10}$$

with the density matrix defined as

$$\rho(t) \equiv \sum_i p_i \left|\psi_i(t)\right\rangle \left\langle\psi_i(t)\right|. \tag{3.11}$$

Here $|\psi_i(t)\rangle$ is the time dependent wave function and p_i is the probability of the wave function to be in state i. Since p_i is a probability it must sum to one ($\sum_i p_i = 1$) which is the normalization condition for the density matrix.

The time evolution of a nonlinear system interacting with a classical electric field is governed by the dipole interaction. We can write the Hamiltonian for this interaction as

$$H(t) = H_0 + H_I(t) \tag{3.12}$$

where H_0 is Hamiltonian of the system in the absence of the electric field and H_I represents the field-matter interaction which is $H_I = \mu E(t)$. Now we have the expressions to calculate the time evolution of the system described by the density matrix.

First, the unperturbed density matrix is

$$\rho(-\infty) = \frac{\exp(-\beta H_0)}{\mathrm{Tr}\left(\exp(-\beta H_0)\right)}, \tag{3.13}$$

which is a statistical representation of the occupancy of the initial states at an equilibrium temperature where $\beta = (k_b T)^{-1}$. Then the time evolution of the density matrix is described by the

Liouville-von Neumann equation as

$$\frac{d}{dt}\rho\left(t\right)=-\frac{i}{\hbar}\left[H_0\left(t\right),\rho\left(t\right)\right]-\frac{i}{\hbar}\left[H_I\left(t\right),\rho_I\left(t\right)\right] \tag{3.14}$$

where $\left[H_I\left(t\right),\rho_I\left(t\right)\right]$ is the commutator between two operators. Since the internal fields of the atom are much greater than the perturbing electric fields the eigenstates of the system, represented by the first term on the right-hand side of Eq. 3.14, remain essentially unchanged. Therefore we only need to expand the density matrix in powers of interactions with the electric fields. Perturbatively expanding the second term on the right-hand side of Eq. 3.14 to the n^{th} order in the field-matter interaction results in[1]

$$\rho_I\left(t\right)\equiv\rho^{(0)}\left(t\right)+\rho^{(1)}\left(t\right)+\rho^{(2)}\left(t\right)+\cdots \tag{3.15}$$

We can now write a description of the n^{th} order density matrix to be

$$\begin{aligned}\rho_I^{(n)}\left(t\right)=\left(-\frac{i}{\hbar}\right)^n\int_{-\infty}^{t}d\tau_n\int_{-\infty}^{\tau_n}d\tau_{n-1}\cdots\int_{-\infty}^{\tau_2}d\tau_1 E\left(\tau_n\right)E\left(\tau_{n-1}\right)\cdots E\left(\tau_1\right)\\ \left[\mu_I\left(\tau_n\right),\left[\mu_I\left(\tau_{n-1}\right),\cdots\left[\mu_I\left(\tau_1\right),\rho_I\left(-\infty\right)\right]\cdots\right]\right]\end{aligned} \tag{3.16}$$

Switching from time points to time intervals using Fig. 3.2 as a reference and taking the expectation value of Eq. 3.16 we arrive at an expression for the polarization

$$\begin{aligned}P^{(n)}\left(t\right)=\left(-\frac{i}{\hbar}\right)^n\int_0^{\infty}dt_n\int_0^{\infty}dt_{n-1}\cdots\int_0^{\infty}dt_1\\ E\left(t-t_n\right)E\left(t-t_n-t_{n-1}\right)\cdots E\left(t-t_n-\cdots-t_1\right)\\ \left\langle\mu_I\left(t_n+t_{n-1}+\cdots+t\right)\left[\mu_I\left(t_{n-1}+\cdots+t_1\right),\cdots\left[\mu_I\left(0\right),\rho_I\left(-\infty\right)\right]\cdots\right]\right\rangle\end{aligned} \tag{3.17}$$

which includes all of the microscopic properties of the material. Eq. 3.17 describes an equilibrium density matrix $\rho_I\left(-\infty\right)$, defined in Eq. 3.13, interacting with an electric field at time point, τ, and then evolving for a time interval, t, determined by the commutator of the density matrix with the dipole operator.

Comparing Eq. 3.17 with Eq. 3.6 we can see the the response function introduced earlier is

actually the microscopic properties of the material and is,

$$R^{(n)}\left(t_n, t_{n-1}, \cdots t_1\right) \equiv \langle \mu_I\left(t_n + t_{n-1} + \cdots + t\right)\left[\mu_I\left(t_{n-1} + \cdots + t_1\right), \cdots \left[\mu_I\left(0\right), \rho_I\left(-\infty\right)\right] \cdots \right]\rangle. \tag{3.18}$$

In principle it is possible to simulate the response of a material given the density matrix, dipole matrix and the fields coupling them together. For simple molecules and atoms this can be accomplished with a reasonable degree of accuracy. For solid state materials and especially at surfaces and interfaces this task is very difficult. The purpose of presenting these equations is to illustrate the interactions occurring with the material which can be difficult to keep track of higher order polarizations.

In the n-th order response function there are many terms that contribute to the n-th order polarization. There are 2^n terms in the commutator which couple with n fields each which interact with the sample in any time order. In addition, there are $n!$ (n factorial) ways those fields can be ordered in time. Moreover, each field has a term corresponding to ω and $-\omega$ corresponding to the electric field and its complex conjugate. In total, there are $2^n \cdot n! \cdot 2$ terms which can contribute to the n^{th} order polarization. We need effective ways to analyze these interaction to determine which ones dominate the polarization response.

The next subsection introduces graphical representations that allow us to visually keep track of the interactions with the density matrix. The pictorial representation keeps track of all of the important features in Eq. 3.17 without having to write down all of the terms.

3.2.2 Graphical representations of the polarization

One way to visualise the pathways of the response is to use a Liouville-space diagram. Considering the simple example of the linear response (Fig. 3.3a) there should be $2^n = 2$ terms contributing to

the linear polarization which are,

$$\begin{aligned} R^{(1)}(t) &= -\frac{i}{\hbar}\langle \mu(t_1)[\mu(0), \rho(-\infty)]\rangle \\ &= -\frac{i}{\hbar}\langle \mu(t_1)\mu(0)\rho(-\infty)\rangle - \langle \mu(t_1)\rho(-\infty)\mu(0)\rangle \\ &= -\frac{i}{\hbar}\langle \mu(t_1)\mu(0)\rho(-\infty)\rangle - \langle \rho(-\infty)\mu(0)\mu(t_1)\rangle. \end{aligned} \tag{3.19}$$

A diagram illustrating these interactions can be drawn with a density matrix starting in the ground state, $\rho(-\infty) = |a\rangle\langle a|$, in the upper left-hand corner. Interactions which change the density matrix from the ground state to another state are indicated by either a vertical or horizontal line. A vertical line indicates interaction from the right side and a horizontal line indicates an interaction from the left side of a density matrix. Time intervals are indicated with a thin, dashed line. The final state, which results from taking the trace, is represented by a thick vertical dashed line (Fig. 3.3). All of the final states end in population states. This is essentially a way to keep track of all of the contributions that can result from taking the commutator of the dipole and density matrix. In the linear case the coupling scheme contains two pathways.

For the second order we expect $2^2 = 4$ contributions to the overall polarization. There is only one path to end in $|c\rangle\langle c|$, one path to end in $|a\rangle\langle a|$ and two paths to end in paths $|b\rangle\langle b|$. Instead of writing out these four contributions it is far easier and often more informative to draw a diagram depicting these interactions.

With the Liouville-space couplings scheme we are able to depict all possible interactions. A complimentary and more detailed picture is captured in a double-sided Feynman diagram. These diagrams take into account how the field interacts with the density matrix and allows us to visually eliminate pathways that do not correspond to either the frequency or wave vector our experiment measures. It also allows us to make approximations based on visually inspecting these diagrams.

Before we go any further we need to describe the nature of the electric field. The electric field is a real quantity which can be decomposed into two exponential components,

$$E(t) = 2\cos(\omega t - ikr) = \mathrm{e}^{-i\omega t + ikr} + \mathrm{e}^{i\omega t - ikr}. \tag{3.20}$$

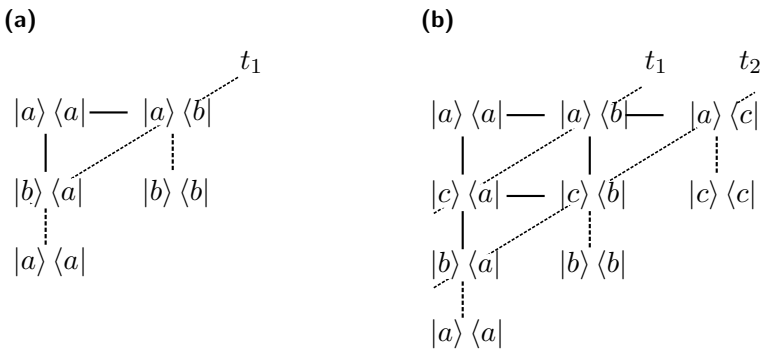

Figure 3.3: Liouville-space coupling scheme for the linear (3.3a) and second order (3.3b) response. Horizontal lines indicate interaction from the right side of the density matrix and vertical lines indicate interaction from the left side of the density matrix. The interaction occurs at time intervals t_1 and t_2. The final interaction indicates the macroscopic polarization calculated from the trace operation.

Whether the field carries a positive or negative frequency and a negative or positive wave vector is important because the signal that we measure must be a sum of all of the frequencies and wave vectors of the field matter interactions.

Double-sided Feynman diagrams keep track of whether an interaction took place from the bra or ket side of the density matrix, if the interaction excites or de-excites the system and the total frequency and wave vector of each interaction. In these diagrams the progression of time is from bottom to top indicated by the vertical lines (Fig. 3.4). Arrows pointing to the right indicate an interaction with an electric field of negative frequency and positive wave vector and arrows pointing to the left, indicate an interaction with an electric field of positive frequency and negative wave vector. Arrows pointing toward a bra or ket signify absorption and those that are pointing away signify de-excitation of a state. The final interaction is from the trace and is signified with a dashed line. As mentioned above the signal is emitted at the sum of all the interaction frequencies and in a wave vector that is the sum of all of the wave vector interactions.

For the case of the total linear polarization there are four diagrams that represent all possible interactions (Fig. 3.4). Two of the diagrams show a de-excitation of the ground state which is not possible. These are eliminated via the rotating wave approximation. Two diagrams are highlighted with dashed boxes. These are the figures that survive the rotating wave approximation. Above the figures is an equation which represents that diagram's contribution to the polarization. The

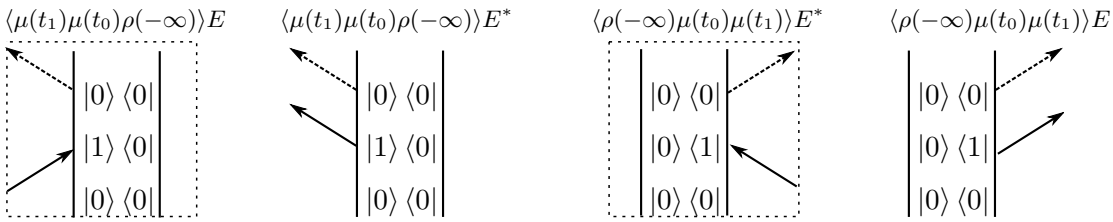

Figure 3.4: Double sided Feynman diagrams for the linear response. Broken line boxes highlight the diagrams that survive the rotating wave approximation.

two boxed diagrams are complex conjugates of each other. We therefore arrive at only one unique diagram. With the concepts of the density matrix and graphical representations of the polarization we can more closely examine static and time resolved SHG.

3.3 Static second harmonic generation

Since the discovery of second harmonic generation (SHG) in 1961 by Franken and coworkers[3] and a subsequent phenomenological description by Bloembergan and Pershan [6] SHG and a variety of related optical nonlinear phenomena have been exploited for practical and scientific use particularly for studying surfaces. SHG is a coherent frequency conversion tool that takes a frequency ω as an input and generates double the frequency, 2ω, as output. Typically an energy level diagram is used to depict this process (Fig.3.5a) where two photons interact with states $|1\rangle$ and $|2\rangle$ to produce double the incident frequency. The states involved in the process can be real, that is they are eigenstates of the Hamiltonian, or virtual. This illustration pervades the literature but the formalism developed in section 3.2 provides a more complete picture of the SHG process.

In Fig. 3.5b we see explicitly two interactions with electomagnetic fields create a coherence between the ground and first state and then between the ground and second state. Since all diagrams must end in a population state the emission is from the second state to the ground state at a frequency $\omega + (\omega) = 2\omega = \omega_{\text{sig}}$ and wave vector $k + k = 2k = k_{\text{sig}}$.

A physical picture of the two interactions and the time evolution of the coherence is provided in Fig. 3.6. The first interaction at time τ_1 creates a coherence oscillating at the fundamental frequency. After a time period t_1 a second interaction with the field at τ_2 creates a coherence at

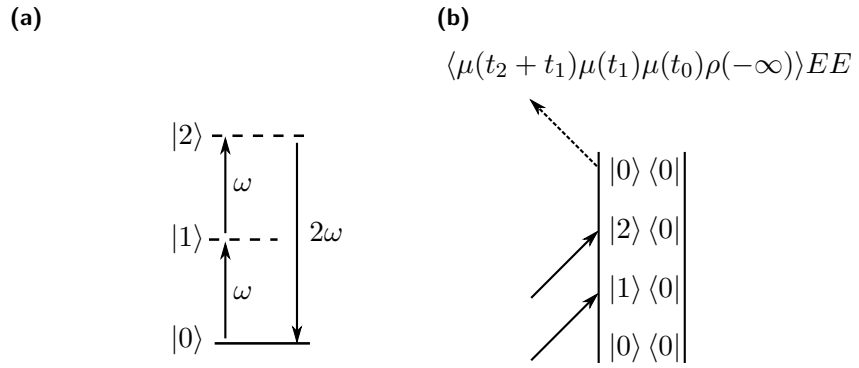

Figure 3.5: Two illustrations of the second harmonic process. Fig. 3.5a is the typical energy level diagram depiction of SHG. Fig. 3.5b displays the Feynman-like diagram for second harmonic generations. The states labeled one and two can be either real or virtual states.

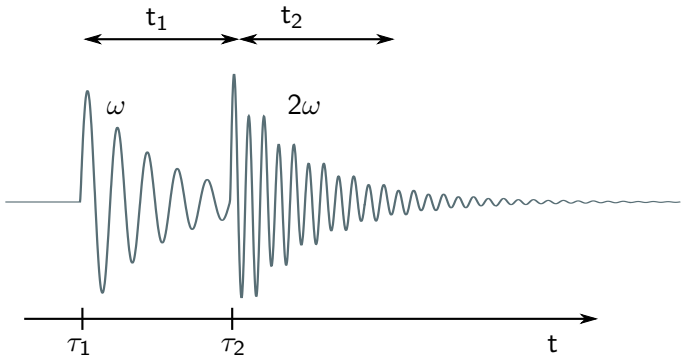

Figure 3.6: Illustration of the internal polarization in a material after interaction with a pulses laser two times at τ_1 and τ_2 to generate polarization at the second harmonic frequency.

twice the fundamental frequency which decays exponentially. For gallium arsenide, the material system of interest here, the polarization response at optical frequencies is typically very short lived; on the order of tens of femtoseconds[7]. Longer lived polarization may occur, however, if the state is in resonance with the laser pulse frequency. With life times on the order of 30 fs it may be possible to observe the resonant states in the frequency domain.

3.3.1 SHG in the frequency domain

From subsection 3.1.2 we know that the time domain response can be Fourier transformed into the frequency domain. Following Boyd's[4] derivation for the second order susceptibility of a 3-level system we can arrive at an expression that we would expect if there are resonances within the

spectral bandwidth of the fundamental pulses. The left side of Fig. 3.5 illustrates the states used in the equation below, where ω is nearly resonant with the $|0\rangle \rightarrow |1\rangle$ transition or the $|1\rangle \rightarrow |2\rangle$ or both. The expression for the nonlinear susceptibility in the frequency domain is

$$\chi^{(2)}_{ijk}(2\omega,\omega,\omega) = (\rho^{(2)}_{00} - \rho^{(2)}_{11}) \left[\frac{\mu^i_{02}\mu^j_{21}\mu^k_{10}}{[\omega_{20} - 2\omega - i\gamma_{20}][\omega_{10} - \omega - i\gamma_{10}]} \right] + (\rho^{(2)}_{22} - \rho^{(2)}_{11}) \left[\frac{\mu^i_{02}\mu^j_{21}\mu^k_{10}}{[\omega_{20} - 2\omega - i\gamma_{20}][\omega_{21} - \omega - i\gamma_{21}]} \right] \tag{3.21}$$

where μ is the transition dipole between two states and their indicies, ijk, range over the Cartesian coordinates x, y, z. When considering optical frequencies the energy levels are separated by sufficient energy so they cannot be thermally populated. Therefore, we can take $\rho^{(2)}_{00}$ to be 1 (for a normalized density matrix) and then the second term Eq. 3.21 is zero.

There are two conditions for resonance which we can explore using this equation. One in which there is one photon resonant the $|0\rangle \rightarrow |1\rangle$ transition and the other in which the fundamental is resonant with both the the $|0\rangle \rightarrow |1\rangle$ and $|1\rangle \rightarrow |2\rangle$ transitions. Since both frequencies are the same for SHG, they are necessarily in resonance with $|2\rangle \rightarrow |0\rangle$. Eq. 3.21 is plotted in Fig. 3.7 with $\omega_{20} = 2\omega_{10}$ and dephasing rates $\gamma_{10}/\omega_{10} = \gamma_{20}/\omega_{10} = 0.07$. Notice how the amplitude shapes are similar but their phases are very different. The one photon resonance has π phase shift whereas the double resonance has a 2π phase shift. Therefore, a method which is phase sensitive could determine whether a resonance is a single or a double resonance.

3.3.2 SHG and symmetry

One of the main goals of this thesis is to measure surface states and electric fields at a surface or interface. SHG is our method of choice to examine surfaces and interfaces because even order nonlinear processes are forbidden in centrosymmetric materials. The argument relies purely on symmetry considerations and is relatively simple. If we have a coordinate system $\mathbf{r} \rightarrow (x, y, z)$ and apply an electric field in the $+z$ direction the polarization response is also in the $+z$ direction. When we invert the coordinate system $-\mathbf{r} \rightarrow (-x, -y, -z)$ then the polarization as well as the electric field change sign. The crystal, however, is the same since each atomic position, when inverted, is at

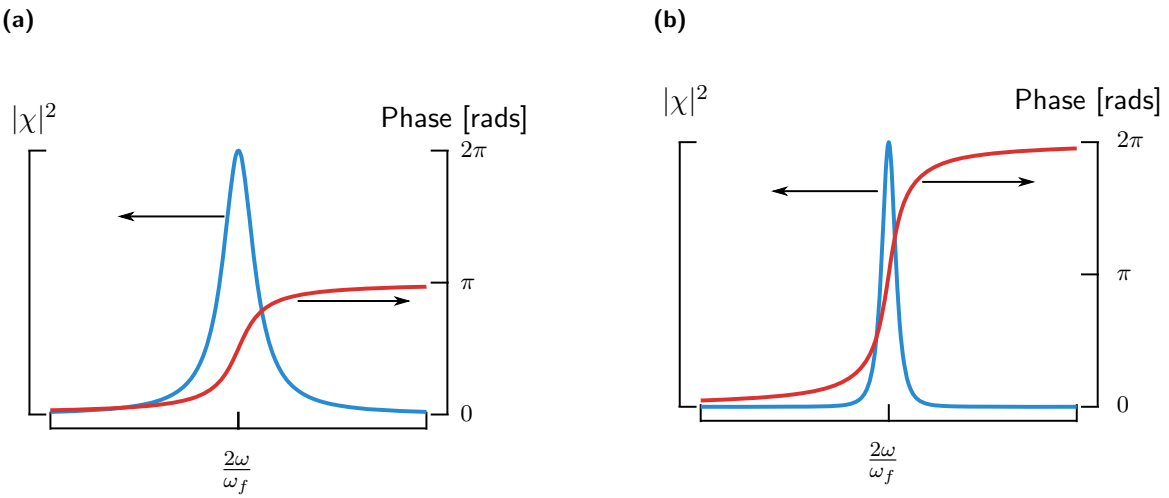

Figure 3.7: Resonance conditions from Eq. 3.21 indicating a resonance with either the fundamental photon or the second harmonic photon 3.7a and a resonance with both the fundamental and second harmonic frequency 3.7b. The resonance occurs at $\frac{2\omega_f}{\omega_f}$ where ω_f is the fundamental frequency.

exactly the same location. So we are left with an equation

$$-P_i^{(2)}(\omega) = \epsilon_0 \chi_{ijk}^{(2)}(\omega)(-E_j(\omega_1))(-E_k(\omega_2)). \tag{3.22}$$

The left side of the equation is negative and the right side of the equation is positive. The only way a negative number can equal a positive number is if $\chi_{ijk}^{(2)} = 0$. This argument holds true for all even orders of the polarization. This simple result is the origin of the surface sensitivity of SHG. Only when centrosymmetry is broke, at a surface or an interface, is SHG allowed (within the electric dipole approximation).

For other non-centrosymmetric materials there is a large SH signal from the bulk of the material. There is, however, still a possibility of measuring the surface selectivity. By judiciously choosing the azimuthal angle of the crystal and the polarizations of the incident pulses it is possible to eliminate the bulk contribution to the signal[8]. The total second order polarization with the surface and the bulk is

$$P^{(2)}(2\omega) = \epsilon_0 \chi_{\text{blk}}^{(2)} EE + \epsilon_0 \chi_{\text{surf}}^{(2)} EE. \tag{3.23}$$

These two contributions to the overall polarization can have a different origin and the emitted light may interfere. The only way to separate these components is if there is a polarization combination

that can be used to isolate the surface or bulk contributions individually. Additional contributions arise when we consider an electric field at the surface.

3.3.3 Electric-field induced SH

Electric field present at an interface due to charge transfer or a space charge field can also contribute significantly to the SH signal. This can be described formally as a third order process where two fields are from the fundamental field and the third is from the static electric field at the interface. Incorporating this effect into the expression for the total second order polarization at the second harmonic frequency is

$$P^{(2)}(2\omega) = \epsilon_0 \chi^{(2)}_{\text{blk}} EE + \epsilon_0 \chi^{(2)}_{\text{surf}} EE + \epsilon_0 \chi^{(3)}_{\text{blk}} EEE^{\mathbf{DC}}. \tag{3.24}$$

where we have added $E^{\mathbf{DC}}$ to the overall expression for the polarization. Another phenomena that breaks the symmetry of a crystal, besides the interface, is an electric field at the interface. This can be described as a four-wave mixing phenomenon with a field of zero frequency. This can be expressed with Feynman diagrams except now the interaction described by the arrow carries zero frequency so no actual excitation occurs. This is marked as $|2'\rangle$. More importantly the static field at a surface can be pointing in the $+z$ direction or $-z$ direction which can induce an overall phase shift of 180 degrees in the signal.

Static SHG has at least three contributions arising from the bulk, surface and a DC electric field. Each of these contributions may have a phase associated with them which results in a very complex signal. Furthermore, there may be surface resonances which can add an additional spectral phase to the overall signal. These signals can all contribute to the time-resolved signal as well. In the next section we can begin to see how we can unravel all of these contributions.

3.4 Time-resolved SHG

This section is the culmination of all of the information that has come previously. Time-resolved SHG is a fourth order nonlinear optical experiment. This means that there are 2^4 terms from the

response function and 4! terms which represent the ordering of the incoming pulses. This results in a total of 384 diagrams that can contribute to the fourth order polarization. The number of diagrams for the fourth order polarization can be reduced considerably by taking into account the geometry of the setup and the frequency measured in the experiment.

The experiment consists of two non-collinear laser pulses. The pump arrives first and excites the system. Some time later, the probe arrives to measure the effect of the pump. Only light emitted at the SH of the fundamental frequency and along the same direction as the probe is measured. All other sources of light are either blocked or filtered.

The possible double-sided Feynman diagrams are constrained by the frequency and wave vector measured in the experiment. The emitted signal must have a frequency of $\omega_{\text{sig}} = 2\omega$ and a wave vector $k_{\text{sig}} = k_{\text{probe}}$. Moreover, we know that the final state of the diagrams must be a population state. Therefore the diagrams are constrained to only those which satisfy the criteria above as well as the rotating wave approximation.

Two diagrams which represent the polarization signals measured in a time-resolved SHG experiment are shown in Fig. 3.8. Using the criteria above we can verify that these two diagrams are the polarization signals measured by the SHG experiments. The diagram on the left in Fig. 3.8 has a total wave vector of $k_{\text{pump}} - k_{\text{pump}} + k_{\text{probe}} + k_{\text{probe}} = 2k_{\text{probe}} = k_{sig}$. Therefore the signal is in the same direction as probe. The measured frequency is $-\omega_{\text{pump}} + \omega_{\text{pump}} - \omega_{\text{probe}} - \omega_{\text{probe}} = -2\omega_{\text{probe}} = 2\omega_{sig}$. Thus, this diagram also represents the correct frequency. A similar procedure for the diagram on the right will also show that is a viable pathway to the signal measured in the TR-SHG experiment.

A comparison can be made between this pump-probe spectroscopy and the much more common pump-probe spectroscopy, transient absorption (TA). The two diagrams in Fig. 3.8 are similar to excited state absorption (left diagram) and a signal bleach (right diagram). Conspicuously absent is an equivalent diagram representing stimulated emission. In TA the probe stimulates emission back to the ground state. A similar process is not measurable by TR-SHG because the probe would have to stimulate emission below the ground state, which is not possible.

An example of the data is presented in Figs. 3.9 and 3.10. The two dimensional plot indicates

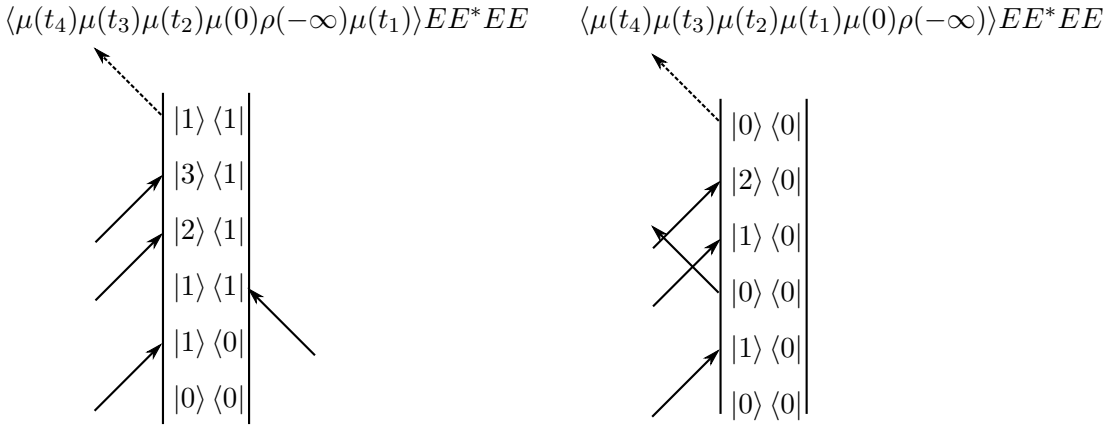

Figure 3.8: Two of the Feynman-like diagrams for the fourth order response measured in a TR-SHG experiment. The left diagram corresponds to excited state SHG while the right side is the diagram for ground state SHG and is responsible for vibrational coherences observed in the SH signal.

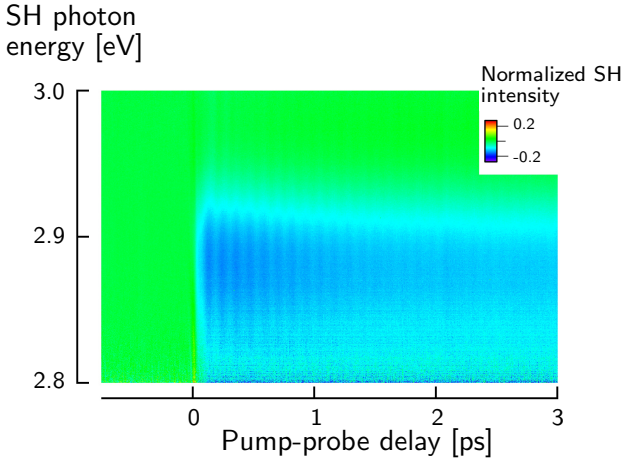

Figure 3.9: Sample of high-resolution data taken on undoped oxided terminated GaAs. The y-axis indicates the energy of the emitted SH photon while the x-axis is the pump-probe delay.

the pump-probe delay on the x-axis and the emission photon energy on the y-axis. When integrating over the wavelength region we can see that there is a vibration at 8.8 THz which corresponds to a longitudinal optical phonon in bulk GaAs[9]. These oscillations are associated with the diagram on the right hand side in Fig. 3.8.

Wavelength slices can also be taken from Fig. 3.9. Taking slices along the 3 ps give a pump-induced SH spectrum as in Fig: 3.10b. These data have noise towards the edges where there is very little intensity from the probe pulse. In the center however, there is an interesting looking spectrum which will be analyzed further in chapter 5. This spectrum is associated with transitions occuring

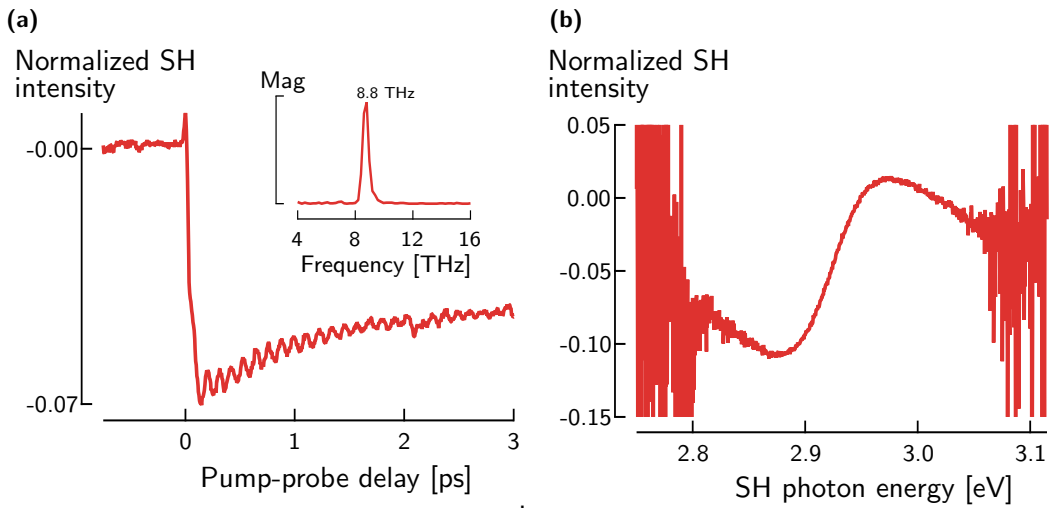

Figure 3.10: Data from Fig. 3.9 with slices along a specific wavelength (3.10a) and at a specific time (3.10b)

at the SH or fundamental frequency. The feynman diagram for these events it the left side diagram in Fig. 3.8.

Being an even order nonlinear spectroscopy, TR-SHG also retains the benefits of surface sensitivity described in section 3.3.2. However, the interference from different contributions described in Eq. 3.24 are still present and can increase the difficulty in interpreting TR-SHG results. Chapter 4 takes advantage of the repid spectral acquisition time to measure SH rotational anisotropy spectra and pump-probe rotational anisotropy spectra. Chapter 5 details a method for extracting the SH amplitude and phase and uses this technique to investigate the time-dependence of SH on the phase of the static SH contributions and surface states.

References

1. Hamm, P. & Zanni, M. *Concepts and Methods of 2D Infrared Spectroscopy.* (Cambridge University Press, 2011).

2. Mukamel, S. *Principles of Nonlinear Optical Spectroscopy.* (Oxford University Press, 1995).

3. Franken, P., Hill, A., Peters, C. & Weinreich, G. 'Generation of optical harmonics.' *Physical Review Letters* **7,** 118–119 (1961).

4. Boyd, R. *Nonlinear Optics.* Third Edit (Elsevier, New York, 2008).

5. Kuzyk, M. G. *Lecture Notes in Nonlinear Optics: A student's perspective.* (NLOsource.com, 2013).

6. Bloembergen, N. & Pershan, P. S. 'Light waves at the boundary of nonlinear media.' *Physical Review* **128,** 606–622 (1962).

7. Becker, P. *et al.* 'Femtosecond photon echoes from band-to-band transitions in GaAs.' *Physical Review Letters* **61,** 1647–1649 (1988).

8. Stehlin, T., Feller, M., Guyot-Sionnest, P. & Shen, Y. R. 'Optical second-harmonic generation as a surface probe for noncentrosymmetric media.' *Optics Letters* **13,** 389 (1988).

9. Chang, Y., Xu, L. & Tom, H. 'Observation of Coherent Surface Optical Phonon Oscillations by Time-Resolved Surface Second-Harmonic Generation.' *Physical Review Letters* **78,** 4649–4652 (1997).

4

Rotational Anisotropy of GaAs

At the end of chapter 3, it is clear that there exist many competing contributions to the time-resolved SH signal. There are, in addition to resonances in the frequency domain, a variety of other SH signals from a surface or interface that can interfere to change the measured intensity of the time-resolved SH signal. Single wavelength pump-probe experiments provide insufficient information to determine the dynamic processes generating the SH at the surface of materials. In this chapter we expand pump-probe SHG to the frequency domain. With the added information we are able to gain a more complete picture of the time resolved dynamics of material surfaces and interfaces. The purpose of this chapter is to demonstrate the utility of broadband femtosecond lasers to rapidly acquire time and angle resolved SH spectra and how this information can elucidate the physical processes generating the SH signal.

We begin by examining the experimental apparatus used to acquire time-frequency data, including the light source, beam path and detection. This is followed by a review the expected rotational anisotropy for gallium arsenide (GaAs), our sample of choice, from SHG measurements. Our results are compared to the expected anisotropy behavior. Finally, We extend the experiment to include rotational anisotropy spectra as a function of pump-probe delay which reveals some unexpected results which will be elaborated on later in chapter 5.

4.1 Experimental set-up

4.1.1 Femtosecond light source

At the heart of all the experiments in this thesis is a home-built oscillator which provides the ultrafast broadband pulses. The oscillator is based on a kerr lens mode-lock design from the Kapteyn-Murnane group[1, 2]. This design enables the laser to operate with large bandwidths. We have measured some of the most important values for the experiments performed here. These values are presented in the following paragraphs to give the reader an idea of the laser system specifications.[1]

The repetition rate is the inverse of the time for one pulse to complete a round trip in the laser cavity. This oscillator operates at 78 MHz at an average power of 550 mW. Power stability over 7 hours is 0.6 % RMS which is comparable to oscillators of similar design from KMLabs which are specified for <1 % RMS deviation.

Ocillator spectral output can be centered from 1.48 to 1.53 eV with a spectral bandwidth of 100 meV. From this bandwidth a pulse of approximately 15 fs is expected out of the oscillator. However, when the pulses were measured with frequency resolved optical gating (FROG)[3, 4], the temporal FWHM of the pulses was approximately 35 fs, indicating significant chirp on the output pulses. This is not important, however, because the pulse will travel through more transmissive optics and will need to be compressed before arriving at the sample.

4.1.2 Optical layout

A complete description of the optical layout along with the manufacturer and part number can be found in appendix A while an abridged optical layout is provided in Fig. 4.1. Two pulses are generated with a 66:33 (Reflection:Transmission) beam splitter with 66 % of the power going to the pump pulse and the difference to the probe pulse. The pump is delayed from the probe by moving a computer controlled optical delay stage. Polarization of both beams is controlled with a waveplate-polarizer combination which also serves as a variable attenuator. Finally, to ensure that there is no interfering SH light from the optics reaching the detector, we placed a colored glass filter,

[1] Appendix A contains the original data used to calculate the specifications for the laser system.

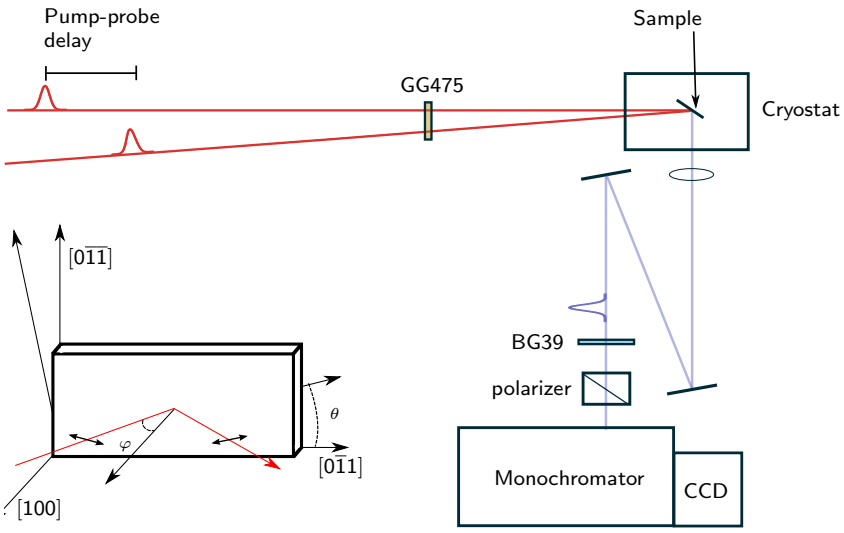

Figure 4.1: Experimental set-up to acquire time-resolved SH spectra with the sample orientation included. The symbol φ is the angle of incidence and θ is the rotation angle about the surface normal.

GG475, in the beam path just before the sample.

The pulses were directed at the sample and focused by concave mirrors with an f-number of 30 at an incident angle of 43° for the pump and 45° for the probe, each projecting an elliptical spot on the sample surface. The minor axis of the pump and probe beam ellipses was determined by the knife-edge technique to be 105 ± 2 μm and 85 ± 1 μm, respectively. Reported spot size measurements are for the 80/20 definition of the spot size.

SH signal from the sample was collected by a lens and then directed to a monochromator with two mirrors anti-reflective coated for 400 nm. Residual fundamental was removed with a BG 39 colored glass filter with OD greater than 4 for the fundamental light. The polarization of the SH was selected with a Glan-Taylor polarizing prism. Finally, the SH spectrum is detected on a LN cooled CCD detector following square law detection,

$$S(\omega) = |E(\omega)|^2 = \left| \frac{1}{2\pi} \int_{-\infty}^{\infty} E(t) \mathrm{e}^{i\omega t} dt \right|^2 . \tag{4.1}$$

Before beginning an experiment the camera was allowed to cool to its operating temperature and maintain that temperature for at least 60 minutes. After the camera had cooled, it was calibrated with an HgAr arc lamp with five spectral lines from 404-435 nm[5].

Samples were mounted in a nitrogen vapor cryostat (Janis ST-100) equipped with a computer

controlled rotation stage for measuring rotational anisotropies. All samples were measured in flowing N_2 gas to minimize effects of photodegredation of the sample surface due to oxidation. To ensure the minimum pulse duration at the sample, a pair of chirped mirrors was used to compensate for the approximately 500 fs^2 of GDD imparted on the pulse by the optical elements in the beam path. They also served to compensate for dispersion out of the oscillator, resulting in a final pulse duration of 20 fs at the sample.

4.2 Gallium arsenide as a model system

The choice of material is important when developing a new technique. Many of the material properties should already be known. One of the most studied materials in history is gallium arsenide (GaAs) making it the perfect sample to demonstrate the utility of our new technique. GaAs is a noncentrosymetric material in point group $\overline{4}3m$ (T_d) which means that SHG is allowed in the bulk of the crystal. In spite of possible complications caused by bulk SHG, GaAs is an ideal material to begin to collect time-resolved SH spectra. One reason, is that GaAs is a very well studied material and nearly every parameter of the bulk crystal has been studied[6] making it ideal for initial characterization of time-resolved spectra. In addition, since our laser spectrum is essentially fixed we need to examine a material with optical transitions within our laser pulse spectrum so that we can excite the sample. Another benefit of using GaAs is that we can begin to assess the the relative importance of bulk, surface and electric field contributions to the time resolved signal discussed in chapter 3.

Additionally, there have been extensive studies employing SHG on single crystal GaAs surfaces. Many of those studies used narrow bandwidth light sources and either wavelength integrated data or scanned the wavelength and provided no time-resolved data. Many of these studies focused on rotational anisotropy data as a proxy for investigating band bending[7] and surface reconstructions[8] or used scanning wavelength to determine bulk resonances[9, 10]. Typically acquiring rotational anisotropy and spectra are not collected together because of the difficulties in tuning the laser for each angle. Generally this is very time consuming and small deviations in the beam

path may accrue over time. So instead of having to repeat the experiment multiple times for every wavelength it is better to use a broadband light source where the entire spectrum can be measured at once. The benefit of the technique used here is the rapid acquisition of spectra without the need to scan wavelength. We can use the time we saved to capture the rotational anisotropy spectra as a function of pump-probe delay. This additional information creates a more complete view of the processes generating SH at the surface and in the bulk of GaAs.

4.2.1 Rotational anisotropy from GaAs

Recall from subsection 3.1.2 that the second order polarization is a third rank tensor. That is, it has three indicies, $\chi^{(2)}_{ijk}$ which relates the incident electric field vectors specified by j and k to the polarization vector i. This tensor can be written as a 3-D matrix with 27 entries (see appendix B.2) resulting in 27 distinct ways to generate SH. The number of terms in the tensor can be reduced by taking into account the crystal symmetry; the more symmetric a material the fewer entries in the third-rank tensor. For a centrosymmetric material all of the entries vanish and the third-rank tensor is zero. For noncentrosymmetric cubic crystals like GaAs, there is a small number of manageable entries. A GaAs crystal, with $\bar{4}$3m symmetry, has six tensor elements which are equal,

$$\chi^{(2)}_{ijk} = xyz = xzy = yzx = yxz = zxy = zyx. \tag{4.2}$$

The third-rank tensor above is defined in crystal coordinates that differ from our experimental coordinates. So in order to determine the tensor elements probed given our sample geometry in figure 4.1 we must derive a relationship between the crystal coordinate system and the laboratory coordinate system. There are four commonly used polarization combinations for SHG which describe the polarization of the fundamental beam and the detection polarization. They are P_{out}-P_{in}, P_{out}-S_{in}, S_{out}-P_{in} and S_{out}-S_{in}. All of these polarizations access different tensor elements and can give rise to different rotational anisotropies. We need to find a way to represent these polarization combinations in the lab coordinates.

There are two equivalent ways of accomplishing this. One is to project the electric field vector into the crystal coordinates, have the fields interact with the material and then rotate the output

back into the lab coordinates. The other method is to rotate the tensor into the laboratory frame. We will use the second method even though there is a little more effort because we obtain the anisotropies for all of the polarization combinations at once (see appendix B.2 for details). For the polarization combinations given above and the constraints of the experimental geometry the equations that relate the fundamental pulse to the SH electric field as a function of azimuthal angle are,

$$E_{pp}(2\omega) \propto \cos(2\theta)\,\chi^{(2)}E(\omega)^2 \tag{4.3}$$

$$E_{sp}(2\omega) \propto \cos(2\theta)\,\chi^{(2)}E(\omega)^2 \tag{4.4}$$

$$E_{ps}(2\omega) \propto \sin(2\theta)\,\chi^{(2)}E(\omega)^2 \tag{4.5}$$

$$E_{ss}(2\omega) = 0 \tag{4.6}$$

As we rotate about the surface normal in the coordinate system defined in Fig. 4.1 we should see intensity patterns that are proportional to the square of Eqs. 4.4-4.6. Therefore the measured anisotropy patterns should exhibit four-fold symmetry.

The four-fold symmetry may be reduced because of the presence of a surface where the crystal symmetry is reduced. A reduction of symmetry leads to additional anisotropic terms which modulate the intensity of the bulk contributions. Interference between the surface and the bulk can reduce the overall symmetry from four-fold to two-fold[8].

In addition to the presence of a surface, a static electric field at the interface will also reduce the symmetry to two-fold. As mentioned in chapter 3 the electric field induced SH (EFISH) is described by a fourth rank tensor. Since we are only concerned with static fields parallel to the surface normal we can reduce the fourth rank tensor to a third rank tensor. For crystals of $\bar{4}$3m symmetry there are only 4 independent tensor elements which are $iiii$, $iijj$, $ijij$, $ijji$ ($i \neq j$) with i and j ranging over the Cartesian coordinates x, y, and z[7, 11]. Since we know that the electric field is always along the z direction when contracted, $\chi^{(3)}_{ijkz}E^{\mathrm{DC}}_z$ we are left with four non-unique entries zzz, $xxz = yyz$, $xzx = yzy$ and $zxx = zyy$. A DC electric field contributes a constant value when rotated about the surface normal which interferes with bulk SH to reduce the overall SH anisotropy to two-fold [12].

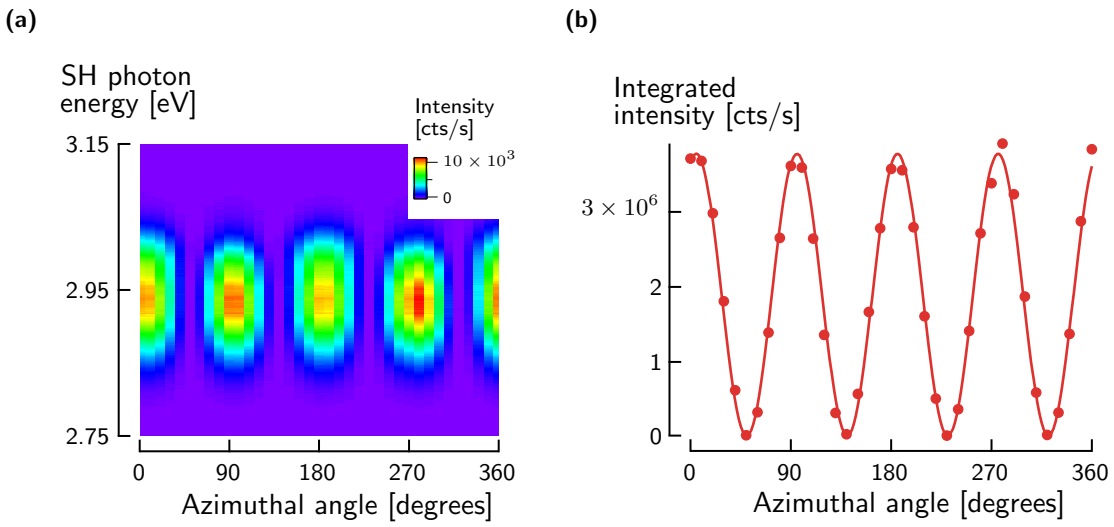

Figure 4.2: Raw data from a rotational anisotropy scan (4.2a). Wavelength integrated data showing distinct four-fold symmetry (4.2b).

4.3 Rotational anisotropy spectra of GaAs(100)

To investigate the utility of acquiring broadband SHG spectra and anisotropy with time resolution, we used a semi-insulating GaAs(100) surface with a resistivity greater than 1×10^8 Ω cm, corresponding to a carrier concentration less than 1×10^7 cm^{-3}. The GaAs(100) surface was passivated by a 5 nm thick epitaxial layer of gallium phosphide (GaP) using metal organic chemical vapor deposition. GaP is a wide bandgap material with $E_g = 2.26$ eV while the E_g of GaAs is 1.42 eV. The energy levels align such that the band gap of GaAs sits completely in the gap of GaP[13]. Moreover, GaP reduces surface states on GaAs by energetically shifting them out of the band gap[14]. These features make GaP a perfect material for passivisation of GaAs and it has been widely used for this purpose[14–16].

Although GaP energetically passivates dangling bonds present at the GaAs interface, the lattice constant of GaP is smaller (5.4505 Å) than GaAs (5.653 Å). The difference in lattice parameters can be characterized by $(a_{\mathrm{GaAs}} - a_{\mathrm{GaP}})/a_{\mathrm{GaAs}}$. Using the lattice constants above, the mismatch is characterized as 3.6 %. Since GaAs and GaP are both piezoelectric materials, Such a large mismatch may create strain and, therefore, an electric field at the interface. This has been observed in GaAs/AlGaAs nanowires where the lattice mismatch was only 0.05 % [12]. The presence

of this field may complicate the interpretation of our data.

As our first test of spectral resolved SHG we used GaP capped GaAs(100) described above at a temperature of 90K with the sample geometry as depicted in Fig. 4.1. The azimuthal rotation, rotation about the surface normal, is indicated by θ and the angle of incidence is indicated with φ. An azimuthal angle of zero corresponds to the $[0\bar{1}1]$ crystallographic direction. All experiments were performed with an incident angle of 45° with respect to the surface normal. Polarization of the incident light and the detected SH was set parallel to the plane of incidence in the P_{in}-P_{out} configuration.

When the GaAs(100) crystal is rotated through an angle of θ, the SH intensity exhibits a four-fold symmetry as expected from eq. 4.4 in the P_{in}-P_{out} geometry (Fig. 4.2). Both the wavelength resolved data (Fig. 4.2a) and the wavelength integrated data (Fig. 4.2b) reflect this fact. However, we must take into consideration that the data are obscured by the pulse envelope. Therefore, in order to extract meaningful conclusions about the frequency dependence of the anisotropy, we must normalize the data.

To find a normalization of the data we first realize that the spectral envelope of the pulse is not changing during the course of an experiment. Then we can assume that the spectral density is constant. With this assumption we are able to normalize each energy between zero and one, allowing for direct comparison between different SH photon energies at the same azimuth. Then any deviation in the intensity from four-fold symmetry is a result of a change in anisotropy due to an interfacial field, a change in surface structure or a resonance.

Normalized data (Fig. 4.3) show a marked change in anisotropy from 2.99 eV to 3.06 eV. In this region there is a lowering of the symmetry from four-fold to two-fold. Taking cuts at three different energies highlights the difference in anisotropy (symbols in Fig. 4.3b) over this region. This modulation reflects the overall contribution to the SH signal which consists of bulk surface electric field and electronic structure of the GaAs(100) sample.

A lowering of crystal symmetry has been observed before and was attributed to a surface reconstruction or a depletion electric field[7]. Both of these effects reduce the symmetry to two-fold and should be independent of wavelength. These studies, however, were carried out at fixed photon

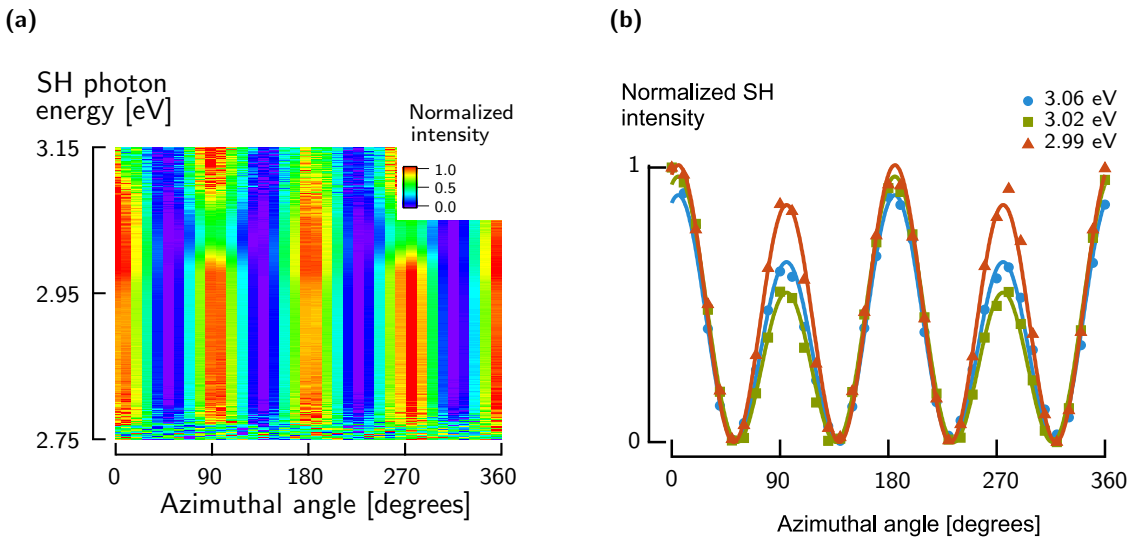

Figure 4.3: Rotational anisotropy after normalization of the photon energy (4.3a). Slices near 3.06, 3.02, 2.99 eV shows distinct two fold symmetry and its dependence on photon energy (4.3b).

energy so they were unable to assess the impact of different photon energies on symmetry. With our broadband technique we are able to determine the photon energy dependence with high resolution.

To further our analysis we will characterize the anisotropy as a function of photon energy by[8, 9]:

$$I(\theta) = |A + B\cos(2\theta)|^2 \tag{4.7}$$

where A is an isotropic contribution to the overall SH signal, B is the much stronger bulk contribution arising from the underlying GaAs(100) crystal symmetry and the cosine term reflects the anisotropy of the crystal point group.

The traces in Fig. 4.3b are fit with Eq. 4.7 yielding information of the isotropic and anisotropic contributions. We can repeat this process for each energy and extract values of A and B at each energy and plot the ratio of the two parameters (Fig. 4.4). The A/B ratio is a measure of the isotropic contribution to the bulk signal. As seen in Fig. 4.4 there is a peak in the ratio at 3.03 eV for a temperature of 90 K. Warming the sample to 190 K shifts the peak to 3.00 eV.

Peaks in the A/B ratio at 90K and 190K are only 30 meV apart. We can compare this small change to the expected changes in the band gap for both the single photon resonance at E_g and the

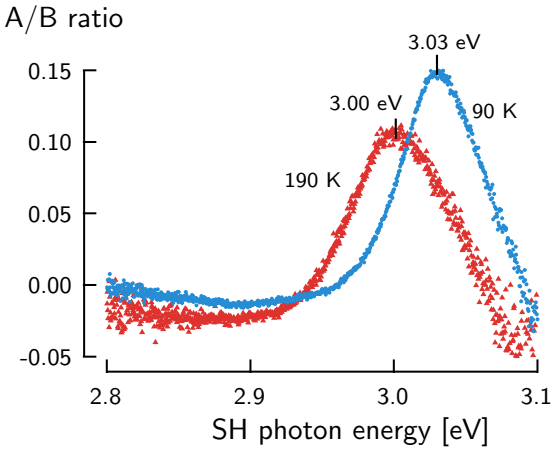

Figure 4.4: A/B anisotropy ratio at temperatures of 190 K and 90 K. Peaks are at locations 3.03 eV for 90 K and 3.00 eV for 190 K with a difference of 30 meV.

two photon resonance at E_1. Changes in band energies caused by temperature can be thought of in the context of tight-binding in chapter 2. When the crystal is cooled the lattice contracts and the atoms move closer together increasing the orbital overlap and increasing the splitting of energy levels which increases the band gap. An opposite effect is expected as the crystal temperature increases. The change in band gap can be quantified using a phenomenological equation called the Varshni equation[17] which uses empirically measured parameters to describe band gap shifts. For GaAs the parameters have already been measured using ellipsometry[18].

With the empirical data and the Varshni equation we can calculate both the expected position and the expected width of the band edge and E_1 resonances and compare them with our measured values. Tables 4.1a and 4.1b compare the peak positions and widths for the E_g and E_1 resonances. Since we can only observe the second harmonic and not the fundamental frequency the band gap peak has been multiplied by two in order to represents the position it would have if that resonance was visible in our experiment.

From these tables we can see that the peak position for our data corresponds more closely to the E_1 resonance. This is further corroborated by the peak width data which show that the width of E_g is exceedingly narrow and again our data corresponds more closely to the E_1 resonance.

While we see qualitative agreement with the E_1 resonance the exact nature of this feature

	90 K	190 K
E_g (eV)	3.00	2.94
E_1 (eV)	3.02	2.97
Experiment (eV)	3.03	3.00

(a) Peak positions

	90 K	190 K
Γ_g (eV)	0.002	0.010
Γ_1 (eV)	0.049	0.058
Experiment (eV)	0.039	0.049

(b) Peak widths

Table 4.1: Comparison of measured peak position and width of the E_1 and E_g resonances with known values for GaAs.

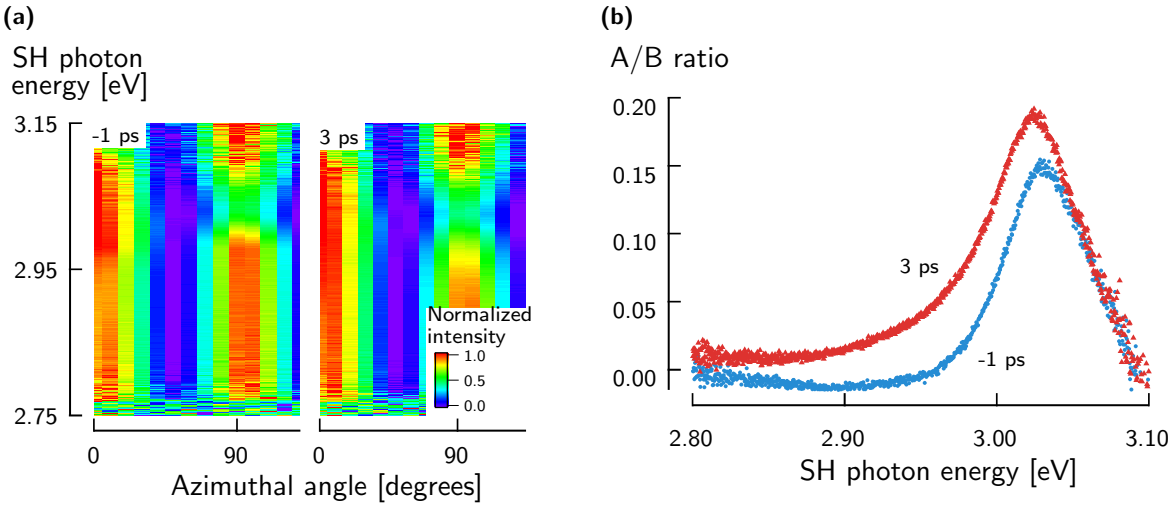

Figure 4.5: Pump-probe rotational anisotropy image plot showing a slight increase in anisotropy at lower energies (4.5a). Fits to Eq. 4.7 extracting the increase in anisotropy (4.5b).

has seen considerable debate. The features seen in our experiment have been seen before by others and have been interpreted as the E_1[9, 10], E_g[19] and a surface state resonance [20]. Since the E_1 resonance is expected to have a higher density of states as compared to the band gap resonance and this feature follows the temperature trend for E_1 resonance both in peak position and in width we believe that this feature arises from the E_1 resonance.

4.4 Rotational anisotropy dynamics

In addition to static rotational anisotropy, we can observe rotational anisotropy dynamics using our pump-probe setup. Fig. 4.5a is a plot of the rotational anisotropy normalized in the same manner as the static anisotropy spectra (4.3a) at time delays of -1 ps and 3 ps. There is a small change in the anisotropy after the pump pulse arrives (Fig. 4.5a). We can characterize the change in anisotropy after the pulse arrives by fitting each photon energy with Eq. 4.7 and extracting the A/B ratio (Fig. 4.5b). After excitation of the GaAs substrate, we observe a shift in the peak position from 3.032 to 3.024 eV and the appearance of a tail extending to lower photon energies. We attribute these to band renormalization and carrier screening because the pump pulse injects a transient carrier density of 10^{18} cm $^{-3}$. These high carrier densities are known to lead to a transient shifts in the band[21, 22].

An alternative to the above data analysis is to normalize the spectrum at a particular pump-probe delay time $I(E, \theta, t)$ by the averaged anisotropy spectra before the pump arrived and present the pump induced change in the spectra as:

$$I'(E, \theta, t) = \frac{I(E, \theta, t)}{I_0(E, \theta, t < 0)} - 1 \tag{4.8}$$

The function I is the intensity as a function of the photon energy E, azimuthal angle θ and pump-probe delay time t. When the spectra are normalized to taken spectra before the arrival of the pump, we obtain the normalized intensity I'. The result of this normalization is displayed in Fig. 4.6a which shows the result of normalization for pump-probe delay times of -1 ps and 3 ps. Near what was determined to be the E_1 resonance in the previous section we see the greatest pump-induced change. In Fig. 4.6a at 3.0 eV we see the normalized intensity increase as we rotate from 0 to 45° and then suddenly the pump induced change turns from positive to negative at 45°. Since we cannot pump the E_1 resonance with our laser pulse the origin of the pump induced change must come from excitation near the band edge.

To highlight this sign change as a function of crystal angle and pump-probe delay we have taken time resolved slices at 2.99 eV and along the $[0\bar{1}1]$ (0°) and $[0\overline{11}]$ (90°) and are shown in Fig.

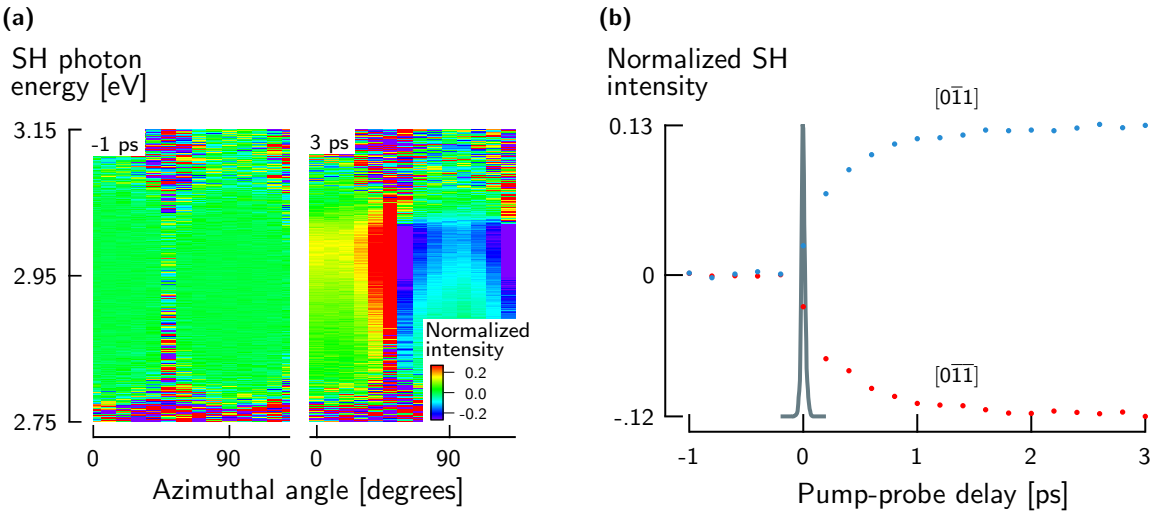

Figure 4.6: Pump-probe rotational anisotropy at -1 ps and 3 ps highlighting the pump-induced change and its variation with azimuthal angle (4.6a). Pump-induced change along two of the principle crystallographic directions in GaAs (4.6b). The auto-correlation of the pump and probe pulse is also shown.

4.6. Exponential fits of both traces give time constants of 400 ± 30 fs which is attributable to the transport of photo-generated carriers in the space charge field[21, 22]. The similarity of the time constants suggests that both traces have the same origin. The opposite sign of the pump-induced change is a consequence of the interference between the [0$\bar{1}$1] and [0$\bar{1}\bar{1}$] crystal directions and an isotropic contribution that seems to be related to the bandgap or possibly a surface state.

By using the GaP capped GaAs(100) sample we have attempted to minimize the contribution of surface states and by using an undoped sample we should also minimize the space charge field. We have used both to explain the data that we observed in this experiment. Most of the evidence for passivisation using GaP comes from surface recombination velocity measurements and theory. Surface recombination velocity, however, does not measure surface state density but only recombination of carriers and there may be other factors that could change the recombination but not the surface state density[23]. There has been no direct spectroscopic evidence for the reduction of state as a result of GaP passivisation. In order to progress further we need to move to oxidized samples with different doping types. There is much more information about these surfaces in the literature which can help when trying to assign spectroscopic peaks.

4.5 Conclusions

This chapter highlighted a technique which uses the broadband nature of femtosecond pulses to rapidly acquire spectra. This rapid acquisition allowed for a detailed study of the anisotropy of both static SH for the GaAs surface and the pump-induced SH. In the static SHG we were able to ascertain that the increase in anisotropy was due to the E_1 resonance. In addition, the ability to take pump-probe SHG data with wavelength and angle resolution has allowed us to study the time-resolved evolution of the signal as a function of photon energy, azimuthal angle and time. This revealed complicated dynamics and signal which we can partially attribute to interference between the bulk and some anisotropic component. In the next chapter we attempt to explain the results obtained in this chapter by working with a variety of GaAs(100) samples which have oxide, sulfur passivated surfaces with either p- or n-type doping.

References

1. Zhou, J *et al.* "Pulse evolution in a broad-bandwidth Ti:sapphire laser." *Optics letters* **19,** 1149–1151 (1994).

2. Asaki, M. T. *et al.* "Generation of 11-fs pulses from a self-mode-locked Ti:sapphire laser." *Optics letters* **18,** 977–979 (1993).

3. Kane, D. J. & Trebino, R. "Characterization of arbitrary femtosecond pulses using frequency-resolved optical gating." *IEEE Journal of Quantum Electronics* **29,** 571–579 (1993).

4. Trebino, R. *Frequency-Resolved Optical Gating: The Measurement of Ultrashort Laser Pulses.* (Springer US, Boston, MA, 2000).

5. Reader, J, Sansonetti, C. J. & Bridges, J. M. "Irradiances of spectral lines in mercury pencil lamps." *Applied optics* **35,** 78–83 (1996).

6. Blakemore, J. "Semiconducting and other major properties of gallium arsenide." *Journal of Applied Physics* **53,** R123–R181 (1982).

7. Germer, T. A., Koasin-acuteski, K. W., Stephenson, J. C. & Richter, L. J. "Depletion-electric-field-induced second-harmonic generation near oxidized GaAs(001) surfaces." *Physical Review B* **55,** 10694–10706 (1997).

8. Yamada, C. & Kimura, T. "Anisotropy in second-harmonic generation from reconstructed surfaces of GaAs." *Physical Review Letters* **70,** 2344–2347 (1993).

9. Janz, S. & Lu, Z. H. "Interband resonances in the optical second-harmonic response of the (001) GaAs-oxide interface." *Journal of the Optical Society of America B* **14,** 1647 (1997).

10. Bergfeld, S. & Daum, W. "Second-Harmonic Generation in GaAs: Experiment versus Theoretical Predictions of χxyz(2)." *Physical Review Letters* **90,** 036801 (2003).

11. Boyd, R. *Nonlinear Optics.* Third Edit (Elsevier, New York, 2008).

12. Hocevar, M. *et al.* "Residual strain and piezoelectric effects in passivated GaAs/AlGaAs core-shell nanowires." *Applied Physics Letters* **102** (2013).

13. Hinuma, Y., Gr, A., Kresse, G. & Oba, F. "Band alignment of semiconductors from density-functional theory and many-body perturbation theory." *Phys. Rev. B* **90,** 155405 (2014).

14. Darbandi, A., Salehzadeh, O., Kuyanov, P., LaPierre, R. R. & Watkins, S. P. "Surface passivation of tellurium-doped GaAs nanowires by GaP: Effect on electrical conduction". *Journal of Applied Physics* **115,** 234305 (2014).

15. Haggren, T. *et al.* "Strong surface passivation of GaAs nanowires with ultrathin InP and GaP capping layers." *Applied Physics Letters* **105,** 033114 (2014).

16. Mariani, G., Scofield, A. C., Hung, C.-H. & Huffaker, D. L. "GaAs nanopillar-array solar cells employing in situ surface passivation." *Nature communications* **4,** 1497 (2013).

17. Varshni, Y. "Temperature dependence of the energy gap in semiconductors." *Physica* **34,** 149–154 (1967).

18. Lautenschlager, P., Garriga, M., Logothetidis, S. & Cardona, M. "Interband critical points of GaAs and their temperature dependence." *Physical Review B* **35,** 9174–9189 (1987).

19. Yeganeh, M. S., Qi, J., Culver, J. P., Yodh, A. G. & Tamargo, M. C. "Interference in reflected second-harmonic generation from thin nonlinear films." *Physical Review B* **46,** 1603–1610 (1992).

20. Tanaka, H., Mizutani, G. & Ushioda, S. "A new resonance of the surface SHG from GaAs(001) in air." *Surface Science* **402-404,** 533–536 (1998).

21. Shah, J., Leheny, R. & Wiegmann, W. "Low-temperature absorption spectrum in GaAs in the presence of optical pumping." *Physical Review B* **16,** 1577–1580 (1977).

22. Shank, C., Fork, R., Leheny, R. & Shah, J. "Dynamics of photoexcited GaAs band-edge absorption with subpicosecond resolution." *Physical Review Letters* **42,** 112–115 (1979).

23. Ohno, T. "Sulfur passivation of GaAs surfaces." *Physical Review B* **44,** 6306–6311 (1991).

5

Demonstration of TR-FDISH

This chapter utilizes the broad bandwidth of the femtosecond oscillator described in chapter 4 to perform spectral interferometry (SI) and extract the amplitude and phase of the second harmonic (SH) light emitted from a sample as a function of pump-probe delay. In the first section, we review the importance of the SH phase and cover the basics of amplitude and phase retrieval using a direct inversion technique called Fourier transform spectral interferometry (FTSI). We then cover the specific implementation used in this thesis for retrieving the time-resolved SH amplitude and phase.

Following the description of SI and the procedure for extracting the amplitude and phase from time-resolved second harmonic generation (TR-SHG), we apply this technique to our model system, GaAs(100). All GaAs samples in this chapter are either oxygen or sulfur passivated with n- or p-type doping. Spectral interferometry will help us determine the phase relationship between bulk and the electric field induced SHG. Then we will concentrate on the pump-induced spectral changes on the GaAs surface where spectral signatures imply the presence of surface states. Moreover, these states exhibit asymmetric line shapes which points to coupling of a discrete surface state with a continuum associated with the bulk. Similar behavior is observed when we investigate charge transfer between CuPc and sulfur passivated p-doped GaAs(100).

5.1 Measuring amplitude and phase

Many experiments seek to measure the frequency or spacial distribution of light from a sample. Methods such as X-ray crystallography and light scattering measure intensity as a Fourier transform of the spacial distribution of electron density in a sample. Ultrafast optical experiments are similar except that they measure the Fourier transform of the response of a material when excited at optical frequencies (see chapter 3). The spectrometer experimentally Fourier transforms this response and records it onto a CCD which measures only the spectral density $S(\omega) = \left|\int_{-\infty}^{\infty} E(t)\mathrm{e}^{i\omega t}dt\right|^2$[1]. In the detection process, important information about the phase of the electric field can be lost, but, this information is critical to understanding the physical origin of the signal.

For some time it has been known in imaging and crystallography that precise knowledge of the phase in the spacial-frequency domain can be combined with amplitude information to reproduce an exact image of the spacial electron density in a crystal. In fact, most of the information which makes an image appear the way it does is because of its spacial phase; without it, exact reproduction of the image is nearly impossible. The necessity of phase information to reconstruct an image is known as phase dominance[2, 3] and has been considered for many years in image processing but rarely in optical experiments.

In ultrafast optical experiments the idea is similar but a little more abstract since we do not form a spacial image but instead a temporal image of material response. By measuring the amplitude and phase of light from linear and nonlinear interactions with our material system we can gain valuable insight into the processes occurring in the material and possibly reconstruct a more complete understanding of the dynamic material response. In the case of surface sensitive techniques, such as SHG, we can gain valuable insight into dynamics at surfaces and interfaces, particularly charge trapping and transfer. We have a problem, however, because detectors only measure the spectral density (spectrum) of the pulse; all phase information is lost. So we need a technique which can help us recover the phase of the optical signal.

There are many ways to recover the phase of a pulse, frequency resolved optical gating (FROG)[4], multiphoton intrapulse interference phase scan (MIIPS)[5], and spectral interferom-

etry (SI)[1]. Both FROG and MIIPS are based off of nonlinear measurements of a pulse to retrieve the amplitude and phase of the fundamental pulse. In our experiment the pulse of interest is the SH light emitted from the sample. These pulses are usually very weak and unable to provide sufficient intensity for nonlinear characterization techniques like FROG or MIIPS. In contrast, spectral interferometry (SI) is a linear technique that is capable of retrieving the amplitude and phase of a pulse. Amazingly, it can measure pulses which, on average, have less than one photon per pulse [6]! Such a sensitive technique is ideal for measuring the weak pulses from our nonlinear experiment.

5.1.1 Fourier transform spectral interferometry concepts

In SI there are two pulses which are delayed by a time τ. Both pulses propagate co-linearly into the spectrometer where the grating performs an experimental Fourier transform of the pulse pair and the resulting interference pattern is measured on a CCD. Mathematically the interference on the detector is described as

$$\begin{aligned} S_\tau(\omega) &= \left| \int_{-\infty}^{\infty} \left[E(t) + E_{ref}(t-\tau)\right] \mathrm{e}^{i\omega t} dt \right|^2 \\ &= \left| \widetilde{E}(\omega) + \widetilde{E}_{ref}(\omega)\mathrm{e}^{i\omega\tau} \right|^2 \\ &= \left| \widetilde{E}(\omega) \right|^2 + \left| \widetilde{E}_{ref}(\omega) \right|^2 + \widetilde{E}(\omega)\widetilde{E}^*_{ref}(\omega)\mathrm{e}^{-i\omega\tau} + \widetilde{E}^*(\omega)\widetilde{E}_{ref}(\omega)\mathrm{e}^{i\omega\tau} \\ &= |E(\omega)|^2 + |E_{ref}(\omega)|^2 + |E(\omega)||E_{ref}(\omega)| \left[\mathrm{e}^{-i\omega\tau - i\phi_{ref}(\omega) + i\phi(\omega)} + c.c\right] \\ &= \underbrace{|E(\omega)|^2 + |E_{ref}(\omega)|^2}_{\text{Non-interfering terms}} + \underbrace{|E(\omega)||E_{ref}(\omega)| \cos\left[\phi(\omega) - \phi_{ref}(\omega) - \omega\tau\right]}_{\text{Interference term}}. \end{aligned} \tag{5.1}$$

The sample and reference fields are denoted $E(t)$ and $E_{ref}(t-\tau)$ and the Fourier transform of the pulse pair is $\widetilde{E}(\omega)$ and $\widetilde{E}_{ref}(\omega)\mathrm{e}^{i\omega\tau}$. The term $\mathrm{e}^{i\omega\tau}$ represents a linear phase shift in the reference pulse caused by the time delay. Quantities with a tilde over the top mark the complex field amplitudes which are separated into amplitude and phase components in the final two expressions. The intensity on the CCD oscillates as a cosine function with the number of fringes determined by the central frequency of the pulse and the delay between the two pulses. There are a couple of conditions that must be satisfied for accurate retrieval of the pulse. First the delay, τ, must be large enough so that the two pulses do not overlap in the time domain. Second, the spectrum of the

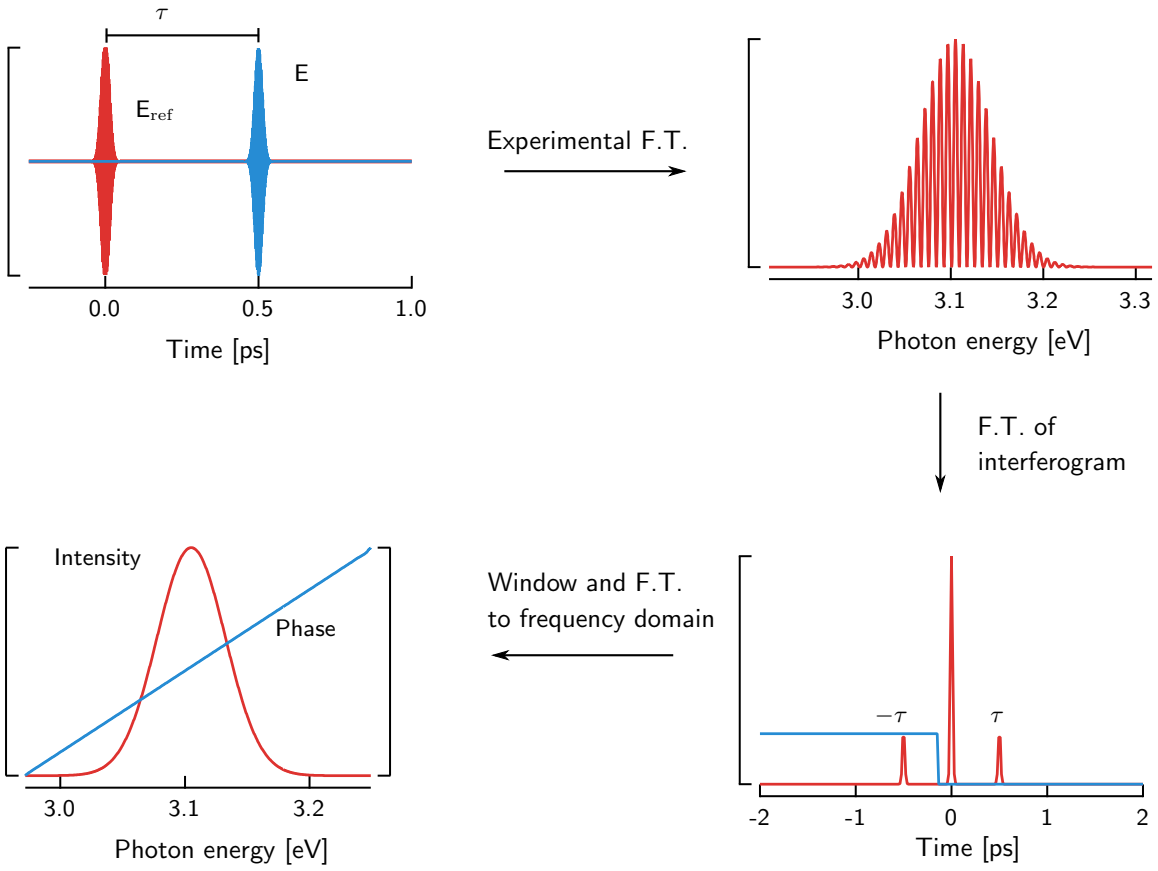

Figure 5.1: Simulated pulses meant to illustrate detection and the direct inversion algorithm for recovering the spectral amplitude and phase. First, the two electric fields with a time delay of 0.5 ps are Fourier transformed yielding the spectrum expected from Eq. 5.1. This is the detection step which is performed experimentally. Then the interferogram is Fourier transformed into the time domain where the peak at $-\tau$ is windowed. This peak contains the correct sign of the sample phase. The windowed peak is Fourier transformed back into the frequency domain where we can separate the sample signal into amplitude (red) and phase (blue). The phase has a linear slope because of the time delay $\phi_{\text{delay}} = \omega\tau$ and can be subtracted from the retrieved phase with knowledge of τ.

reference pulse must be equal to, or greater in bandwidth than the pulse we wish to measure. When both of these conditions are satisfied we can use the direct inversion method for phase retrieval.

Detection and direct inversion to recover the amplitude and phase of the signal pulse are illustrated in Fig. 5.1. The detection step, leading to the final expression in Eq. 5.1, is illustrated with the full real electric field of flat phase Gaussian pulses in the upper left corner of Fig. 5.1. The time delay between the two pulses is $\tau = 0.5$ ps. These pulses enter the spectrometer and are dispersed into their spectral components by the grating. This is equivalent to Fourier transforming the pulse pair. These pulses interfere when they are experimentally Fourier transformed into the frequency domain by the grating which produces an interferogram on the detector (upper-right corner Fig. 5.1). The full signal contains the non-interfering terms, which contain no phase information, and the interference term, which contains the information of interest. The amplitude and phase information of the sample is obscured by the reference pulse so we need to devise a method to extract only the amplitude and phase of the sample.

There are a couple of methods we can use to extract the amplitude and phase of the unknown pulses. One is polarization multiplexing[1] and the other is a Fourier transform method referred to in this thesis as direct inversion [1, 6, 7]. The direct inversion method is our method of choice since it only requires one measurement and is able to directly retrieve the amplitude and phase. The process is described in the flow diagram in Fig. 5.1. First, the measured signal (upper-right corner) is Fourier transformed into the time domain where there are three peaks centered at $-\tau$, 0 and τ (bottom-right corner in Fig. 5.1). By windowing one of these peaks we can isolate and extract the interference term in Eq. 5.1. If the reference intensity, phase and the delay between the pules is known we can easily extract the amplitude and phase of the unknown pulse. There is, however, an ambiguity associated with this method of phase extraction stemming from the fact that the signal is a cosine function.

Since the cosine is an even function there is a sign ambiguity in the retrieved phase. For example, $\cos[\phi_{ref}(\omega) - \phi(\omega)] = \cos[-\phi_{ref}(\omega) + \phi(\omega)]$ which means that the phase could be either positive or negative. To resolve this issue we can look at the complex form of the signal which are the third and fourth terms in Eq. 5.1. The complex exponential part of these equations contain

terms at $i\omega\tau$ and $-i\omega\tau$ which when Fourier transformed into the time domain (see lower-right corner of Fig. 5.1) yields peaks at $-\tau$ and τ as well as a DC background centered at zero. In addition to the time delay, the correct phase is also included in the exponent. As long as we know which pulse entered into the spectrometer first, we can window the peak which contains the positive sample phase and Fourier transform this peak which recovers the sample phase with the correct sign.[1]

In equation 5.1 we have already assumed that the reference pulse arrives first and the sample pulse follows. Therefore the peak corresponding to the proper extraction of the phase is the negative peak. If the sample pulse was first then the signs of the sample and reference pulses are interchanged and then the correct peak in the time domain to window is the peak as positive τ. Despite the ease of phase extraction there are may practical issues associated with the implementation of SI, especially for SH photon energies. These concerns are addressed in the following subsection.

5.1.2 Practical spectral interferometry for SHG

Practical implementation of SI is a challenging task for many reasons. First, it requires precise overlap of both the reference and the sample laser pulses. Moreover, the beam path must be stable on the order of $\lambda/2$ to retain high fringe contrast and ensure repeatability. At typical SH wavelengths of 400 nm this is a very difficult task. Mach-Zender and Michelson geometries have already been considered but it was found that stability was difficult to maintain and the fringe contrast was poor[8]. In the same study the authors tried a completely collinear geometry which provided high fringe constant and was less sensitive to air currents and temperature differences that would normally deteriorate the signal in optical interferometry experiments[8]. Because of the added benefits of a collinear beam path we will also use this beam geometry in our implementation of second harmonic SI (SHSI).

An example of the beam path used for SHSI is given in Fig 5.2. The optic in the probe beam path generates a reference SH pulse that is delayed from the fundamental by the difference

[1]Extracting the correct sign of the phase during the retrieval process can be complicated by different definitions of the Fourier transform used in different disciplines. The one used in the text is the modern physics definition but neglects the prefactor of $\frac{1}{\sqrt{2\pi}}$. The messy details of the direct inversion algorithm are discussed in more detail in appendix C.3.2.

in group velocity of the fundamental and the SH through glass. The fundamental continues to the sample where the pulse generates a SH signal from the sample. From there, both the reference and sample SH propagate to the spectrometer where both pulses are dispersed by the grating onto the spectrometer where we measure our signal as a function of wavelength.

Measuring the signal as a function of wavelength is also problematic. All of the Fourier transforms in the direct inversion algorithm require the data to be linearly spaced in the frequency domain; our data, however, are only linearly spaced in wavelength. Actually, the data are only linear spaced in pixel, strictly speaking. To map the wavelength to the pixel we generate a calibration function with the use of known spectral lines from a HgAr vapor lamp. A typical calibration function is simply a polynomial expansion as[7]

$$\omega(x) = \omega_0 + \alpha_1 x + \frac{1}{2}\alpha_2 x^2 + \frac{1}{6}\alpha_3 x^3 \cdots \tag{5.2}$$

The effect of the nonlinear data spacing to create an artificial phase factor in the retrieved complex electric field

$$S_{\text{ret}}(\omega) = |E_{\text{ref}}(\omega)||E(\omega)|(e)^{i\omega(x)\tau + \Delta\phi} \tag{5.3}$$

where ω has been replaced by the calibration function $\omega(x)$ which introduces higher order phase into the retrieved data.

Typically linear or cubic spline interpolation is used to interpolate the nonlinear wavelength axis into a linear frequency axis[9, 10]. This method, however, can introduce artifacts in the retrieved phase which is undesirable[7]. Another method is an exact interpolation scheme called the zero filling method. This method does not introduce any phase artifacts, but it requires a Fourier transform followed by padding the Fourier transform with 4N the number of points in the data. Therefore our data, which contains a spectrum of 1340 points would require 5360 points. Since we want to take time resolved SH data we will have one spectrum at each delay point and about 100 delay points. Then the total data that has to be handled is 536000 points. This number of points can become unwieldy. Fortunately, there is a simpler way which is to Fourier transform the data directly using the pixel spacing nonlinear frequency spacing and then subtract out the phase $\omega(x)\tau$ to yield the correct, undistorted sample phase.

One requirement laid out in the previous section is the need for a well characterized reference pulse. This is typically not available for the SH because the reference is still too weak to be measured with a nonlinear characterization method such as FROG. Instead we look to internal normalization. One method used to recover static SH phase is to use a spectrally flat reference such as quartz. The term spectrally flat means that this material is free from one or two photon resonances. This can then become a standard sample[9, 10] for all of our measurements.

Taking pump-probe data provides an attractive alternative for normalizing the data. If we are only concerned with the pump-induced changes, which we typically are, then we are able to normalize all of the data internally to the unpumped portion of the data. That is, when the probe arrives before the pump. To see how this can help us recover only the pump induced phase we will walk through the normalization procedure.

When the reference is generated though SHG there may be many contributions that make up the phase. The phase and the phase difference are then given by[10]

$$\Delta\phi(2\omega) = \overbrace{\left[\phi^{\chi}_{samp} + \phi^{f}_{samp} + \phi^{I}_{samp}\right]}^{\text{Sample phase}} - \overbrace{\left[\phi^{\chi}_{ref} + \phi^{f}_{ref} + \phi^{p}_{ref} + \phi^{R}_{ref}\right]}^{\text{Reference phase}} + \frac{\omega l}{c}\left[n_{air}(2\omega) - n_{air}(\omega)\right] + \frac{\omega d}{c}\left[n_{glass}(2\omega) - n_{glass}(\omega)\right]. \tag{5.4}$$

Here, the total phase difference has been separated into all of its contributing components; ϕ^{χ}_{samp} is the nonlinear susceptibility phase, ϕ^{f}_{samp} is the phase acquired from the nonlinear Fresnel factors. A DC electric field contributes a phase ϕ^{I}_{samp}. The last two components of the reference phase are a DC propagation delay, which occurs in non-phased matched thin films, and the phase acquired as a result of reflection from the sample. The last two terms are the phases acquired due to the propagation delays through air and glass over distances l and d.

When normalizing the phase we divide the pumped sample by the unpumped sample. In this case we can write the magnitude and phase as[11]:

$$\frac{|E_{samp}(2\omega,t)|}{|E_{samp}(2\omega,t<0)|} = \frac{|E_{samp}(2\omega,t)||E_{ref}(2\omega,t)|}{|E_{samp}(2\omega,t<0)||E_{ref}(2\omega,t<0)|} \tag{5.5}$$

$$\exp[i\Delta\phi(2\omega,t) - i\Delta\phi(2\omega,t<0)] = \frac{\exp[i(\omega\tau + \Delta\phi(2\omega,t))]}{\exp[i(\omega\tau + \Delta\phi(2\omega,t<0))]} \tag{5.6}$$

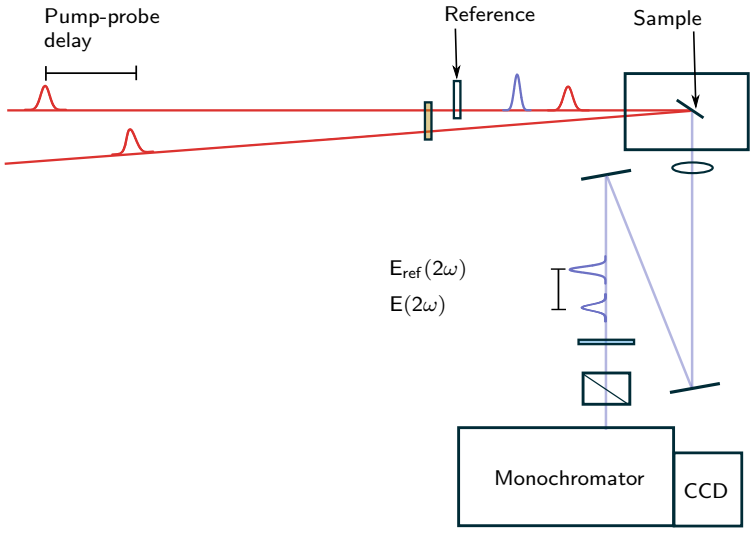

Figure 5.2: Experimental setup for SH spectral interferometry. A more complete description of the experimental setup along with a list of all components can be found in appendix A.

Since the neither the reference nor the delay through air or glass should change as a function of pump-probe delay, the phase normalized to the unpumped sample can be simplified to

$$\Delta\phi(2\omega, t>0) - \Delta\phi(2\omega, t<0) = \left[\phi^{\chi}_{samp}(t>0) + \phi^{f}_{samp}(t>0) + \phi^{I}_{samp}(t>0)\right] - \left[\phi^{R}_{ref}(t>0)\right] \tag{5.7}$$

where the only remaining contribution from the reference is the reflection of the SH reference. Normalizing the data in this way eliminates some sources of error associated with imperfect calibration of the CCD and small phase changes associated with change from one sample to another to acquire interferograms on a standard sample.

Alternatively, we can attempt to look at the phase referenced to a spectrally flat, standard sample. This was the preferred method in many static phase resolved SHG studies where quartz was the preferred standard sample[10, 12–14]. In this case, the phase due to the reference cancels when the sample and standard sample (quartz) are divided by each other. This is a method which we can use to understand static spectra in our material system.

5.1.3 Implementation of SHSI for phase retrieval

In order to carry out interferometry measurements we need a way to generate a reference SH pulse. We obtained a reference SH signal by inserting a poled polymer film with large second order nonlinear susceptibility into the path of the probe beam (see Fig. 5.2). The polymer was formulated by doping 20 wt% of dipolar chromophore, 2-(3-cyano-4-(4-(dibutylamino)styryl)-5- phenyl-5-(trifluoromethyl)furan-2(5H)yli-dene)malononitrile, into polycarbonate[15]. The polymer was spin-cast onto a glass slide with a thickness of approximately 780 nm and then poled at a temperature of 120°C under an electric field of 100 V μm^{-1}. The poled films showed a Pockels coefficient of 35 pm/V at a wavelength of 830 nm to a large $\chi^{(2)}$ of 146 pm V^{-1}. After poling, the top gold electrode was etched off by a gold etchant, and the poled polymer films were used to generate the reference pulse for all the SHSI measurements in this chapter.

The reference SH pulse generated from the poled polymer film was delayed from the remaining fundamental pulse by the group velocity delay of the fused silica windows on the cryostat. The SH field generated from the fundamental pulse at the sample surface propagates collinearly with the reflected reference pulse into the spectrometer where the interference spectrum was recorded on a liquid nitrogen cooled charge coupled device.

All data were collected with a custom built LabView® program which interfaced with a delay stage, CCD camera and spectrometer. A background spectrum was acquired before data acquisition to remove unwanted signal from the SH spectra. The CCD camera has a variety of settings which can be controlled. All of the data acquired in this chapter were as follows. An exposure time of 500 ms with an analog-to-digital conversion of speed of 200 kHz. The analog gain was always set to high and the read out port to low noise. A custom bin of pixels on the CCD selected only pixels that were illuminated by the SH signal. This was typically 1340 pixels wide by 20 pixels high. The temperature was always set to -120°C. CCD data was always cleared before acquiring a new spectra at a different delay point. This removed the chance of the CCD acquiring spectra over multiple delay points.

Time resolved data were collected by scanning the delay stage several times. Each scan was recorded and saved in a separate folder. The final averaged scan was analyzed and imported into

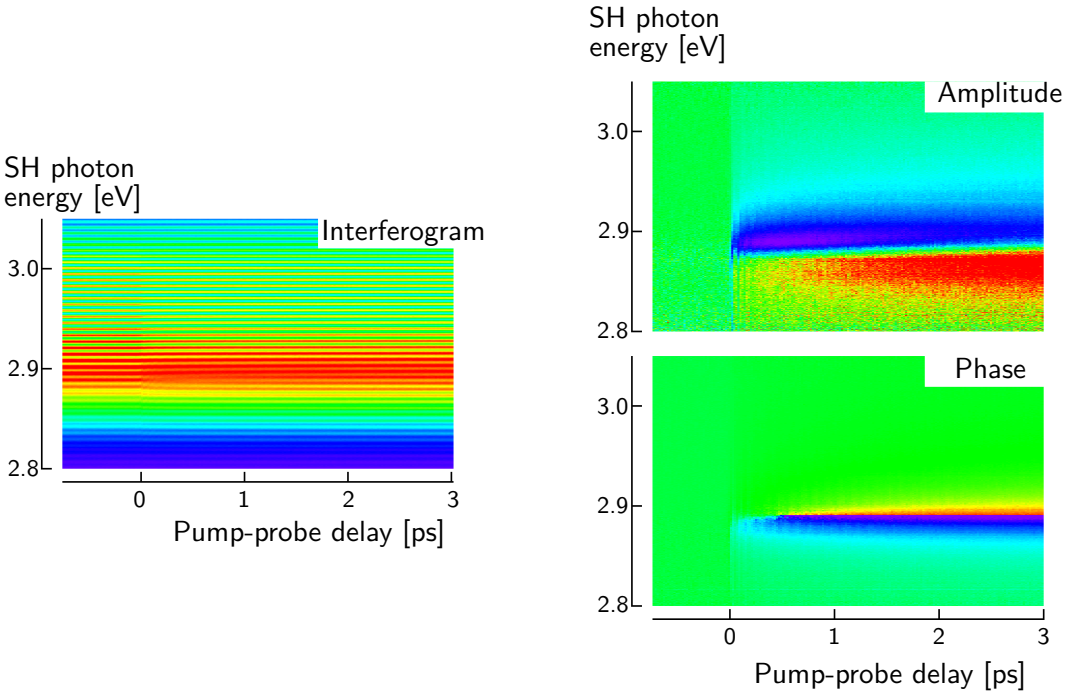

Figure 5.3: Example interferometric pump-probe data acquired on an n-type GaAs sample. Raw data is generated by acquiring a spectral interferogram at each pump-probe delay point (left side). Each interferogram is analyzed using the direct inversion algorithm explained in the text and normalized to negative pump-probe delay which reveals a change in the amplitude (top right) and phase (bottom right) as a function of both photon energy and pump-probe delay.

MATLAB® where interferograms at each delay were analyzed with the direct inversion algorithm with custom code in MATLAB® (see appendix C.3.2). All data were normalized to data at negative pump-probe delay as described above. A sample time-resolved interferogram and corresponding amplitude and phase are given in Fig. 5.3.

When taking a discrete Fourier transform we must window the data in the time domain effectively reducing the number of points when we Fourier transform back into the frequency domain. Since the resolution in the frequency domain is equal to the range in the time domain, windowing reduces the overall resolution of the experiment. We can calculate the reduced resolution from windowing with the equation $\delta\nu\frac{n}{n_{\text{win}}}$. For our data $n = 1340$ points, $n_{\text{win}} = 645$ points and $\delta E = 3.4$ μeV. Therefore using Fourier transforms and the direction inversion algorithm reduces the resolution of the experiment to approximately 1 meV. This is more than enough to determine spectral features as we can see in Fig. 5.3.

5.1.4 Samples for second harmonic spectral interferometry

All samples used in the following experiments were either n- or p-type GaAs. Doping levels for the n-type GaAs were 2.5×10^{18} cm^{-3} and p-type GaAs was 1×10^{19} cm^{-3}. Complete data sheets for the three different types of GaAs used in the experiments performed in this thesis are in appendix E. Surfaces of the oxide passivated samples were cleaned with isopropanol and acetone and immediately transferred into the cryostat.

Sulfur passivated samples were prepared by rinsing the samples 3× with isopropanol and then acetone. The oxide layer was then removed by a 60 sec treatment in NH_4OH. The sample was rinsed with 18 MΩ·cm water and transferred to an $(NH_4)_2S$ solution where the sample remained for 2 hrs. After 2 hrs the sample was rinsed again with 18 MΩ·cm dried with nitrogen and immediately transferred to the cryostat. Before any experiments were preformed the cryostat was purged for 2 hours with N_2.

Charge transfer studies were carried out only on sulfur passivated p-type GaAs. Sulfur passivated GaAs samples were prepared in exactly the same manner as described above. After passivisation the GaAs crystal was transferred into an N_2 filled glove box and was immediately transferred into a thermal deposition chamber. Copper phthalocyanine (CuPc) was deposited at a temperature of 395 °C at a rate of 0.11 Å s^{-1}. The rate was determined with a quartz crystal microbalance. Final film thicknesses were between 10-20 nm. Base pressure during depositions was better than 10^{-7} mbar. During deposition a portion of the GaAs crystal was shadowed to prevent CuPc from being deposited on that portion of the substrate. This provided an *in-situ* control where we could check spectra and the dynamics of the CuPc/GaAs against a bare sulfur treated substrate on the same wafer at the same azimuthal angle. After CuPc was deposited on GaAs the organic-inorganic heterostructure was transferred through the air into the cryostat where it was purged for 2 hrs with flowing nitrogen before laser illumination. This was an effort to prevent any photo-oxidation of CuPc or GaAs during the purging process.

After purging the cryostat, the camera was aligned and the pump power was adjusted so that the pump power was 260 mW and the probe power was 80 mW. Spot sizes were measured with the knife edge test to be 100 μm for the pump and 65 μm for the probe. These spot sizes are using the

80/20 definition of the spot size.

5.2 Energy integrated SHG from GaAs(100)

5.2.1 Crystal direction dependence of SHG phase

To test the implementation of this time resolved technique we begin with a well known and well studied sample. From chapter 4 we already know we can see a variety of changes in the static as well as time resolved SH spectra of GaAs. Rotational anisotropy allowed us to normalize the data which revealed the presence of a two photon resonance attributed to the E_1 resonance in GaAs. Time-resolved data focused on amplitude changes as well as spectral features which occur in both the temporal and spectral domain (see Fig. 4.6). First we will concentrate on the time resolved amplitude changes from GaAs. Using the interference fringes we will be able to confirm the assumption made in chapter 4 that the pump induced change and the static SHG from the bulk can be either in phase or out of phase with each other. The total SH signal depends on both space charge field direction as well as crystallographic direction of the GaAs(100).

In order to provide evidence for our hypothesis we need to use a material which we know has an electric field near the surface. In chapter 2, we saw that a defective surface can have many states that are energetically in the band gap. By doping the material we can fill these traps which creates an energetically unfavorable situation at the surface of the semiconductor. As a result, the bands bend to lower the overall energy in the surface region (see Fig. 2.6). This creates a near surface electric field which is detectable by our experiment. Furthermore, by switching from n-type to p-type GaAs we can change the direction of this field.

Our experiment to test the relationship between bulk and electric field induced SH begins with n-type GaAs(100) with a native oxide. First, we will examine the raw spectral interferograms along the $[0\overline{1}\overline{1}]$ and $[0\bar{1}1]$ crystallographic directions. From Fig. 5.4 we can see that the two directions contain a fringe difference of exactly one fringe. This means that the two crystallographic directions are exactly 180° out of phase with each other which is consistent with previous observations[12].

We can rationalize this phenomenon in two ways; first, by looking at the equation for rotational

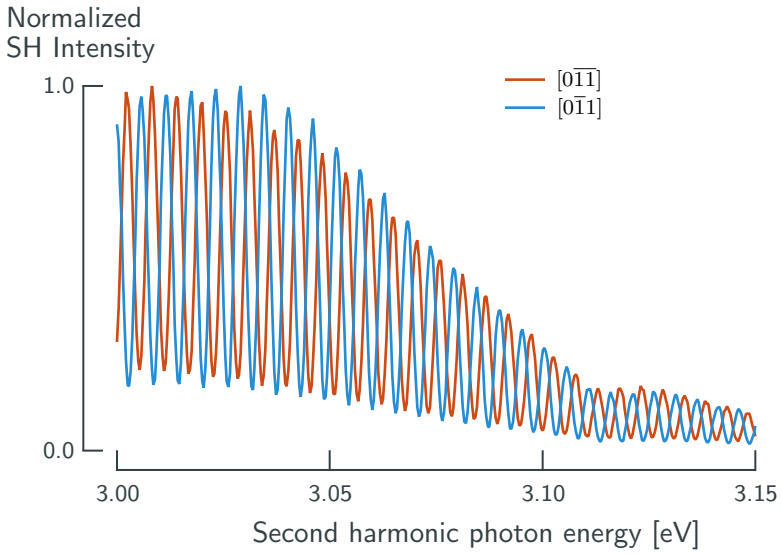

Figure 5.4: Interferograms recorded along the $[0\bar{1}\bar{1}]$ and $[0\bar{1}1]$ show a shift of exactly one fringe between the two directions. This indicates that there is a $180°$ phase shift between the bulk SH emitted along the two directions.

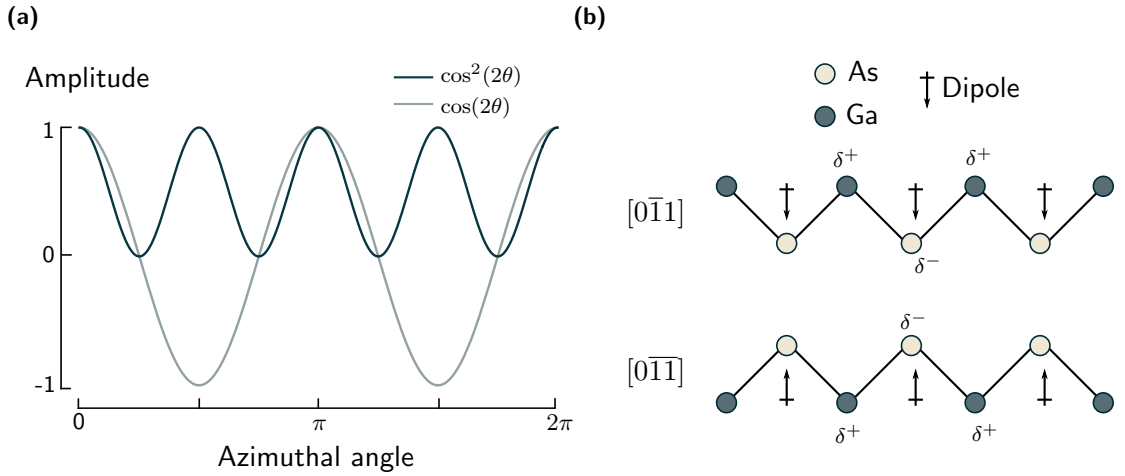

Figure 5.5: Phase relationship as the crystal is rotated about the surface normal. Fig. 5.5a represents the azimuthal function derived from crystal symmetry with both the electric field and intensity contributions. Fig. 5.5b provides a physical explanation. In a first approximation, there is an electronegativity difference between the Ga and As atoms. This creates a partial positive charge on Ga atoms and partial negative charge on As atoms. The over all effect is a dipole which points in different directions for different crystal directions.

anisotropy in the P_{in}-P_{out} configuration, and second, by looking at the physical arrangement of the atoms along the two crystal directions (see Fig. 5.5). The equation for the azimuthal dependence of SHG from GaAs(100) is $E = \cos(2\theta)$ but the measured quantity is actually $I = |E|^2 = \cos^2(2\theta)$. As the crystal is rotated from one crystal direction to the other, the sign changes from 1 to -1 corresponding to a 180° phase shift in the signal. If we only measure the intensity we are unable to resolve this sign change 5.5a. With phase resolution we can recover the sign difference between the crystallographic directions.

We can also arrive at a physical interpretation of the phase shift by looking at the crystal structure of GaAs. Bonds in GaAs have an asymmetry in their charge distribution because of the difference in electronegativity between Ga and As. This means that there is a partial positive charge, δ^+, on Ga atoms and partial negative charge, δ^-, on As atoms. As the crystal is rotated from one crystal direction to the other, the direction of this dipole (Fig. 5.5b) changes the phase of the SH emitted from the bulk. With the phase resolved implementation of SH we are able to detect sign changes along the azimuthal angle will help us ascertain the phase relationship between the GaAs bulk and electric field SH.

5.2.2 Dependence of TR-SHG on crystal angle

Now that we understand the phase difference arising from different crystal directions we can concentrate on pump induced changes seen in n-type GaAs (Fig. 5.6a). We can clearly see that the pump-induced change along the $[0\bar{1}1]$ increases while the signal along the $[0\bar{1}\bar{1}]$ decreases. Initially this is counter intuitive since we would expect a decrease in the electric field due to band gap excitation of n-type GaAs and, therefore, a decrease in the overall SH signal (Fig. 5.6b). This is not the case and it can be explained by taking the phase of each contribution of the SH signal into account.

In order to understand the data in Fig. 5.6a we must break down the total SH into its various contributions. In chapter 3 we covered a variety of contributions to the SH signal. The two most important contributions which need to be considered here are the bulk SH, which we can consider independent of time since the lattice is not changing, and the electric field induced SH which we

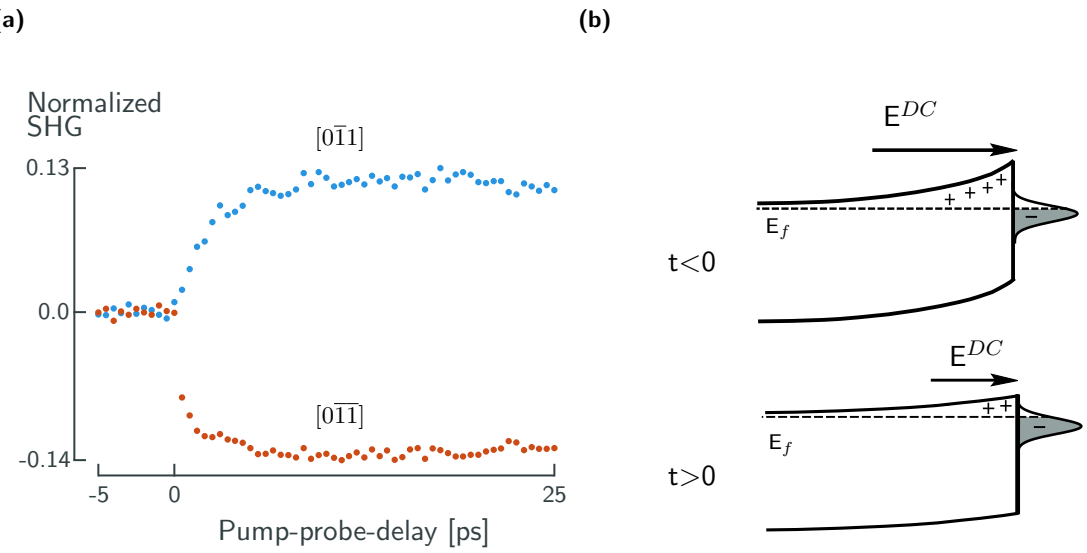

Figure 5.6: Energy integrated pump-probe data on n-type GaAs along the $[0\bar{1}\bar{1}]$ and $[0\bar{1}1]$ crystal directions (5.6a). The corresponding physical picture where the space charge field E^{DC} is reduced after the arrival of the pump (5.6b). The data however show an increase in the signal along the $[0\bar{1}1]$ direction 5.6a.

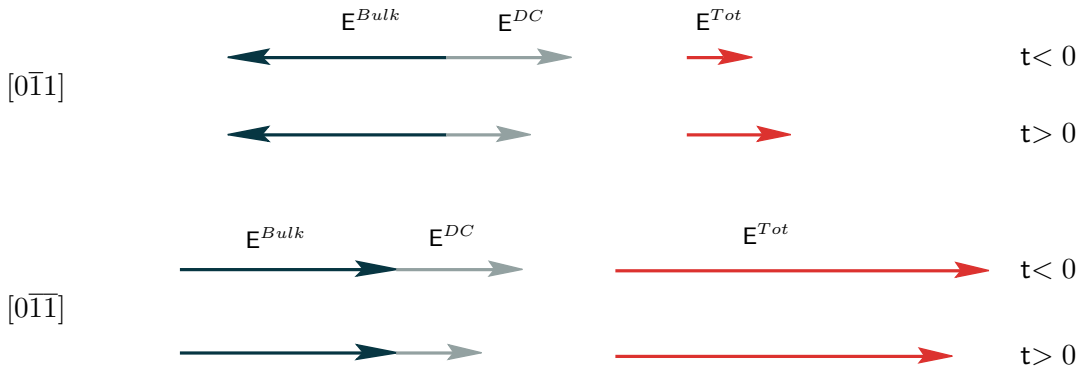

Figure 5.7: Vector diagram illustrating the contributions and phase relationship along two crystal directions for the unpumped ($t < 0$) and pumped ($t > 0$) n-type GaAs(100) along both crystal directions. The contributions are separated into bulk (E^{bulk}), the electric field (E^{DC}), and their sum (E^{Tot}).

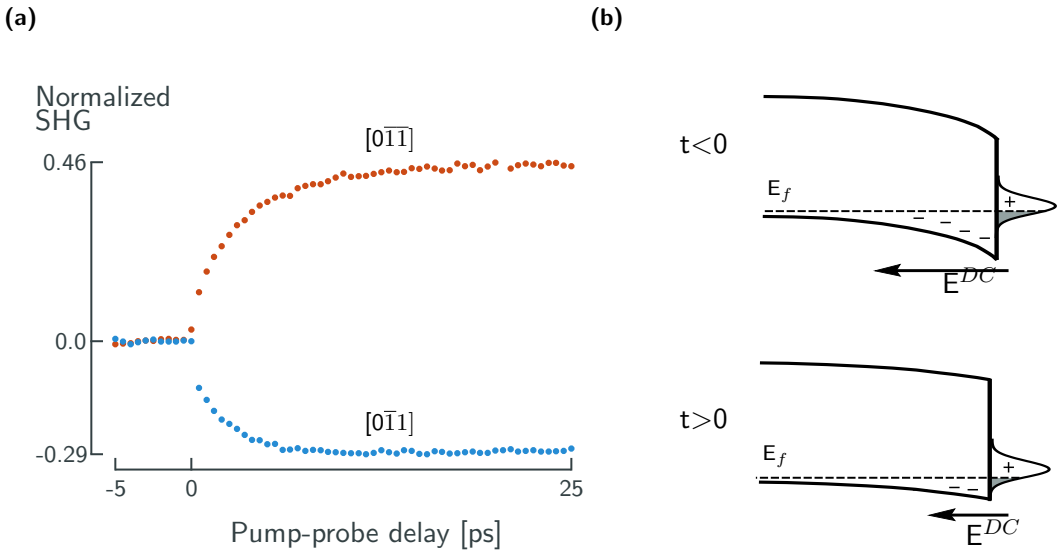

Figure 5.8: Energy integrated pump-probe data on p-type GaAs along the $[0\overline{1}\overline{1}]$ and $[0\bar{1}1]$ crystal directions (5.8a). The corresponding physical picture where the space charge field E^{DC} is reduced after arrival of the pump (5.8b).

expect to decrease after the GaAs has been pumped. Fig. 5.7 illustrates the vector contributions of both the electric field E^{DC} and the bulk E^{Bulk} SH as well as the total contribution E^{Tot} for both the unpumped ($t < 0$) and pumped ($t > 0$) GaAs.

Focusing on the $[0\bar{1}1]$, the bulk and the electric field contributions are considered to be 180° out of phase. When the two vectors on the left are added we can obtain the total resultant as the red arrow on the right for both $t < 0$ and $t > 0$. If we divide the vector for $t > 0$ by the vector for $t < 0$ then we will recover the signal that is measured in the experiment. Namely, a signal increase along the $[0\bar{1}1]$ crystal direction.

A similar vector expression can be derived for the $[0\overline{11}]$ direction. In this case, however, the bulk contribution points in the other direction. We know this from the spectral interferometry fringe shifts above which indicated a 180° phase shift from one crystal direction to the other. Now the two components add constructively so that when the electric field is reduced the SH signal also decreases.

If the interpretation of the electric field interfering with the bulk GaAs is correct, we should be able to test this hypothesis by switching the direction of the electric field. This is equivalent to switching the direction of the electric field vectors in Fig. 5.7. We can accomplish this by switching from n-type to p-type GaAs. The opposite doping creates a space charge field pointing in the opposite direction 5.8b. When the experiment above is repeated we see that the signal along the $[0\bar{1}1]$ now decreases and the signal along the $[0\overline{11}]$ increases exactly as expected (Fig. 5.8).

The next section switches from the time domain into the frequency domain. The purpose is to gain insight as to the origin of spectral features. We know from the previous chapter that there are resonances near our fundamental and SH photon energies. By investigating the dependence on crystal angle and doping type we will be able to understand the spectral features in our experiment.

5.3 Recovered SH spectra from GaAs(100)

So far we have only examined wavelength integrated time-resolved SH traces and have neglected the spectral dependence of the SH from the GaAs(100) surface. As we saw in chapter 4 there can be

large variation in the SH signal within the bandwidth of the laser. This section highlights the pump induced spectral changes of GaAs(100) which reveals distinct SH line shapes. These features display temperature and rotational dependence and exhibit different line profiles for whether depending on the doping type. In addition the surface passivisation also changes the SH signal from the surface. Data on samples with oxidized surfaces will be presented first followed by data for sulfur passivated GaAs(100).

5.3.1 Oxide terminated GaAs

Oxide terminated GaAs has a defective surface which leads to a strong space charge field. The dynamics of which were studied in the previous section (sec. 5.2). These surface states are typically broadly distributed in energy, but we may be able to measure electronic transitions from these states with SHSI described in section 5.1 if their energy distribution is less than the bandwidth of the laser pulse. This section examines the spectral response of GaAs(100) at a pump-probe delay time of 25 ps. These data reveal both the power of the SHSI technique in selectively interrogating surface states.

Data acquired with SHSI on oxide terminated GaAs(100) surface is presented in Fig. 5.9. The first striking result is that there is a prominent spectral feature for n-type GaAs along the $[0\bar{1}1]$ direction. This spectral feature is noticeably absent along the $[0\overline{11}]$ crystal direction. For p-type GaAs the situation is reversed; the most prominent spectral feature lies along the $[0\overline{11}]$ direction while the other crystal direction is devoid of any spectral features.

Crystal directions with spectral features have peaks resembling asymmetric Lorentzians. In order to test whether this is a real line shape or the result of our interferometric detection or the direct inversion algorithm we systematically changed the temperature from 250K to 100K (Fig. 5.9). As the sample temperature decreases we see a shift in the spectral peak from lower to higher energies, which is consistent with what we would expect upon cooling GaAs. This indicates that the spectral features are not due to artifacts from detection or the direct inversion algorithm.

Having established the reliability of the data we can attempt to understand the origin of the asymmetric Lorentzian peaks. Asymmetric peaks are the result of quantum mechanical coupling

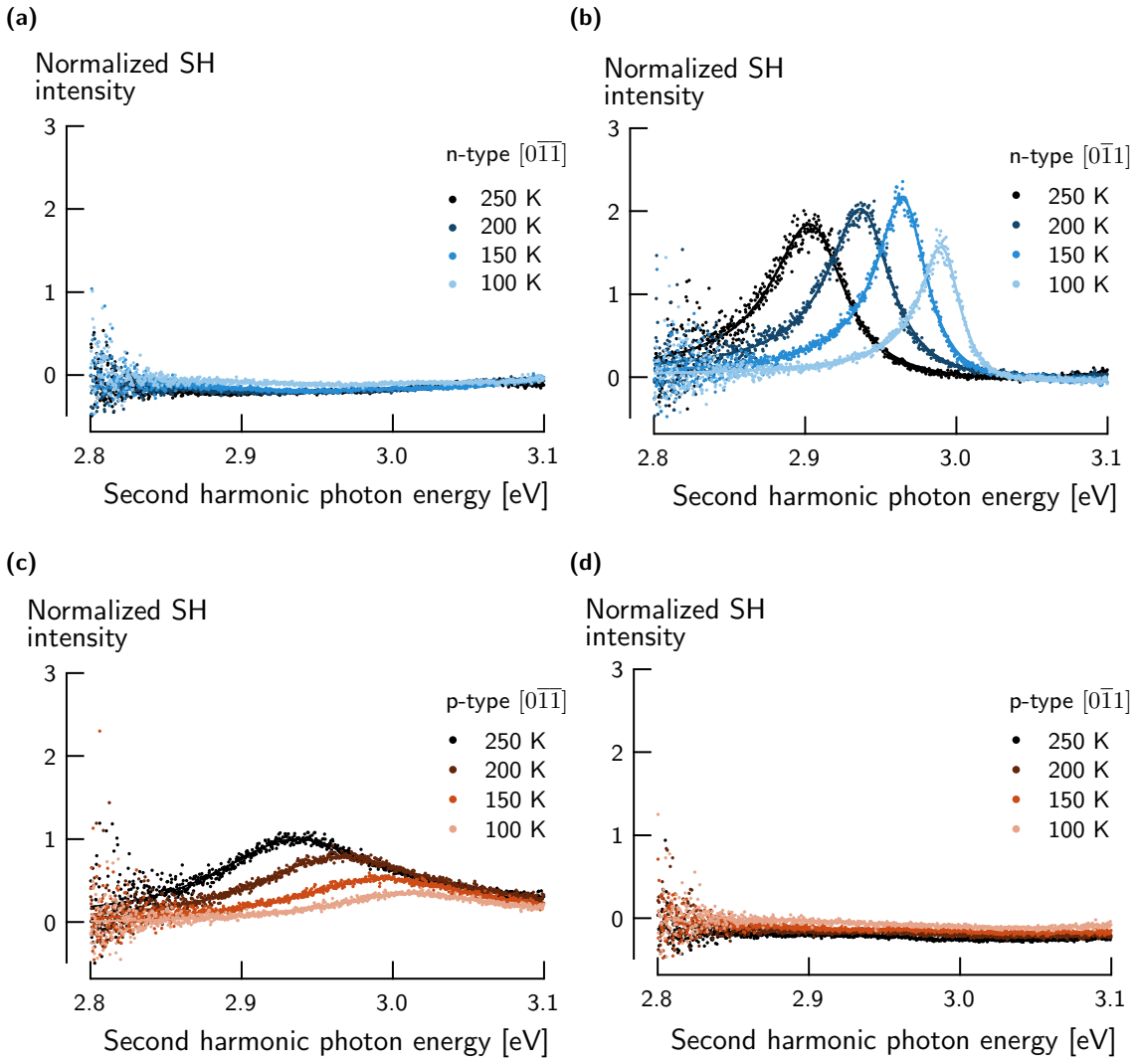

Figure 5.9: Spectral slices taken at 25 ps as a function of sample temperature for n-type GaAs along the $[0\bar{1}\bar{1}]$(Fig. 5.9a) and $[0\bar{1}1]$ (5.9b) and for p-type GaAs also along the $[0\bar{1}\bar{1}]$ (Fig. 5.9c) and $[0\bar{1}1]$ (Fig. 5.9d). The lines in Figs. 5.9b and 5.9c are fits to the Fano function which is described in the text.

between a a ground state and a continuum state. A mathematical description of this phenomena was first described by Ugo Fano[16] in 1961 and are known as Fano resonances or Fano line shapes. Fano resonances have been observed in a variety of disciplines including atomic physics[17–20], molecular spectroscopy[21] and solid state physics[22, 23]. These line shapes have been observed in linear absorption spectra near the band edge. Although this was only able to be observed at a temperature of 1.6 K and a magnetic field of 10 T[24–26].[2]

A graphical representation of the energetic situation which leads to a Fano resonance is displayed in Fig. 5.10. The ground state ($|0\rangle$) can be coupled into either a discreet state ($|1\rangle$) or a continuum of states ($|E_i\rangle$) by an incident light field. The two exited states themselves are coupled through V_{E_i1}. This leads to the formation of new eigenstates in the material whose new optical transition matrix elements are given by[16, 28, 29]:

$$|\mu(E_i)|^2 = \frac{(q+\epsilon)^2}{1+\epsilon^2}\mu_{E_i1}^2 \tag{5.8}$$

The variable $\mu_{E_i1}^2$ is the original transition matrix element for the uncoupled continuum energetically distant from the discrete state. The Fano parameter, q, dictates the line shape and can be decomposed into the parameters illustrated in Fig. 5.10 [29],

$$\begin{aligned} q &= \frac{\mu_{10}}{\pi V_{E_i1}\mu_{E_i0}\rho} \\ &= \left(\frac{2}{\pi\Gamma\rho}\right)^{1/2}\frac{\mu_{10}}{\mu E_i 0} \end{aligned} \tag{5.9}$$

Here ρ is the density of states of the continuum. So, the Fano parameter q is proportional to both the transition dipole elements of the two states as well as the coupling. The width parameter, Γ, is the inverse of the lifetime, and is:

$$\Gamma = 2\pi V_{E_i1}^2\rho \tag{5.10}$$

Therefore the peak width is due solely to the coupling between the two excited states. The parameter

[2] A review of the prevalence of Fano resonances in a variety of fields is given a review in reference[27].

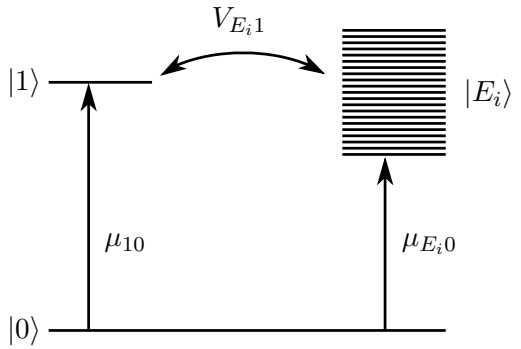

Figure 5.10: Energy level diagram depicting the situation of coupling to a continuum. Ket $|0\rangle$ is the ground state, $|1\rangle$ is the excited discreet state and $|E_i\rangle$ is the continuum of states. Transition probabilities between the ground state and one of the excited states are given by μ_{10} or μ_{E_i0}. The variable V_{E_i1} is the coupling between the excited discreet state and the continuum.

epsilon is called the reduced energy and is:

$$\epsilon = \frac{E - E_1}{\hbar(\Gamma/2)} \tag{5.11}$$

where E_1 is the position of the discrete state $\hbar$ is the reduced planks constant and Γ is the reciprocal lifetime described above.

From these equations it is clear that the line shape is sensitive to the coupling strength and the transition matrix elements. Strong coupling leads to short lifetimes, and therefore, broad peaks with very distinct line shapes. Very weak coupling yields a more Lorentzian line shape, and in the limit of no coupling, a perfect Lorentzian is recovered.

With this information we can find ways to test the hypothesis that the asymmetric line shape is caused by a discreet surface state coupled to a continuum of surface projected bulk states. Since the surface projected bands and the coupling between the surface state and these bands should be anisotropic we can rotate the crystal. As the crystal the coupling parameter and the transition matrix element should change resulting in a change in line shape with crystal rotation.

We rotated both n- and p-type samples with an oxidized surface at a temperature of 100 K to ascertain if the line shapes changed as a function of rotation. The data are presented in Fig. 5.11. Both doping types have a very different line shapes as the crystal is rotated. First, the n-type sample spectral shape changes significantly as the sample is rotated about its surface normal. A

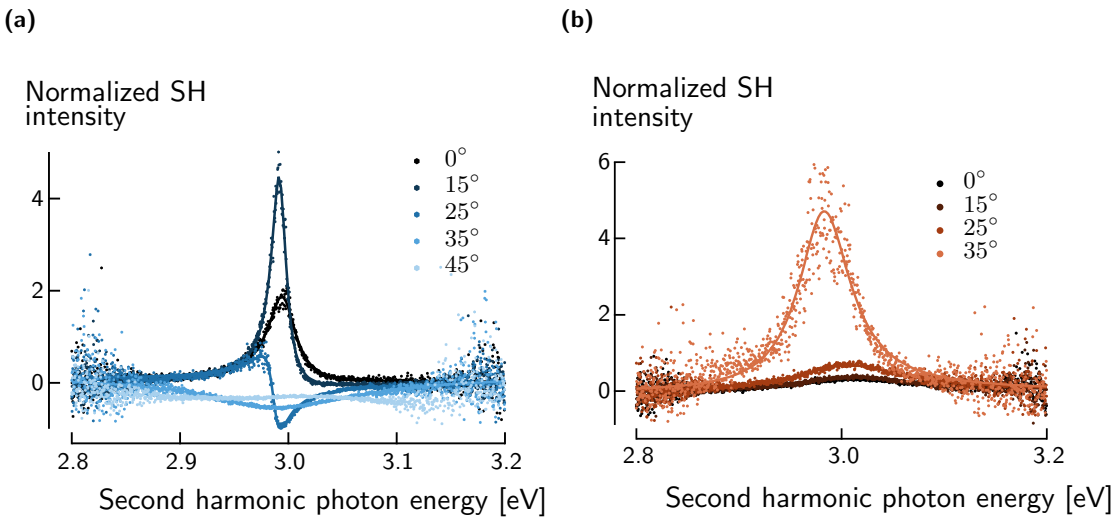

Figure 5.11: Rotational dependence of the pump induced SH spectra at 25 ps for both n- and p-type oxidized surfaces. The angles are relative to the $[0\bar{1}1]$ direction for n-type (Fig. 5.11a). For p-type crystals the zero angle is relative to the $[0\bar{1}\bar{1}]$ crystal direction (Fig. 5.11b). Dots are data points and lines correspond to fits with the Fano equation (Eq. 5.8).

Angle [°]	q	E_0 [eV]	Γ [eV]
0	-10.7	3.00	0.032
15	-8.3	2.99	0.017
25	-0.77	2.99	0.016
35	-0.04	2.99	0.187

(a) n-type

Angle [°]	q	E_0 [eV]	Γ [eV]
0	3.2	2.98	0.126
15	9	3.00	0.139
25	11	3.00	0.134
35	65000	2.98	0.061

(b) p-type

Table 5.1: Fano parameters recovered from fitting Eq. 5.8 to the data in Figs. 5.11a and 5.11b

simple fit with the Fano formula gives values of q and Γ.

For the n-type spectra the most interesting change occurs between 15° and 25° azimuth. Fit parameters indicate that the width remains nearly constant, 0.017 eV width for 15° and 0.016 eV for 25°. The q parameter, however, changes dramatically, from -8.3 to -0.77. This indicates that the primary influence on the line shape is the change in the ratio of the transition dipole moments for the discreet and the continuum states. Furthermore, when rotating from 25° to 35° the q parameter changes from -0.77 to -0.04 while the width changes from 0.016 eV to 0.187 eV. This large change is most likely due to increased coupling between a discreet state and a continuum of states.

Trends for the p-tye GaAs are significantly different. Fano's parameter, q, increases over all angles until it becomes very large indicating the recovery of a Lorentzian line shape. The width is essentially constant until 35° where it drops to half. This indicates a decrease in coupling between the discreet and continuum states. now that we have established our ability to manipulate the spectral line shape by rotating the crystal about its azimuth we can discuss possible origins for the discreet and continuum states.

The Fano formula above describes a discrete state coupled to a continuum and in GaAs there are two possible origins of a discrete state. First is the exciton; however, the exciton binding energy is approximately 0.004 eV corresponding to a temperature of 45 K[30]. Peaks in the linear absorption spectra, corresponding to excitons, can be observed at temperatures below 200 K[31]. At 250 K the exciton line is sufficiently broadened so that an exciton peak is unresolvable. Data in Fig. 5.9b, however, show a peak that is visible for all temperatures. Furthermore, an excitonic peak should be visible for both n- and p-type with the same width and peak energies. While there are peaks on both samples they are different enough to point to a different origin of the peak for each surface.

A second possibility is that the discreet state is caused by defects at the oxide-GaAs interface. There has been a report of a surface state under the oxide surface from a combined SHG and SFG study on an oxide terminated n-type GaAs(100) surface[32]. These data show signs of a discrete state at the surface of n-type GaAs. No comparable study has been carried out on p-type GaAs, however, from the data above it is clear that the states on the n- and p-type GaAs may have very

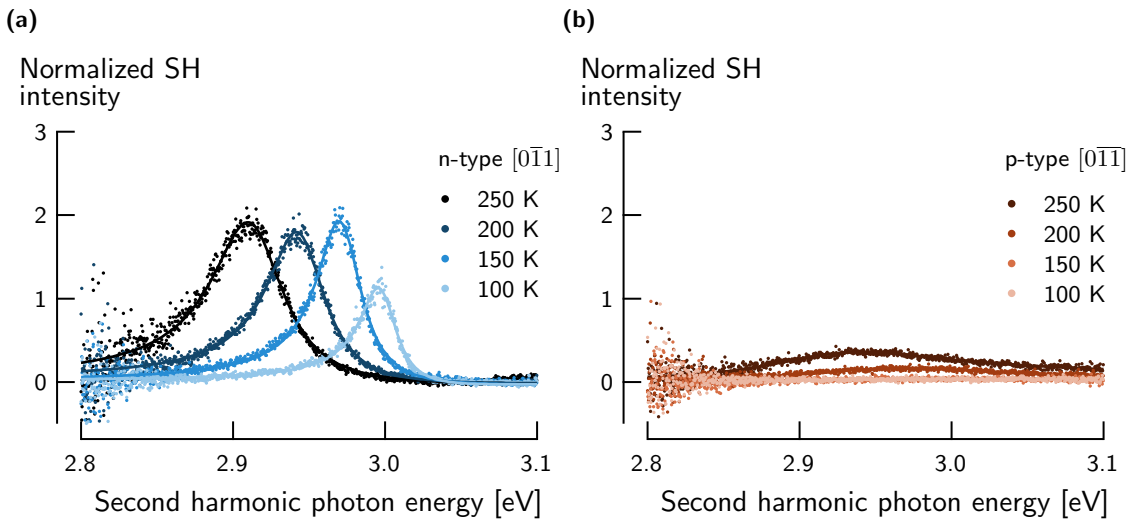

Figure 5.12: Temperature dependence of the SH signal from sulfur treated GaAs surfaces. Data for n-type GaAs (5.12a) was taken along the [0$\bar{1}$1] direction. The p-type data (5.12b) was taken along the [01$\bar{1}$] direction.

different origins. Modifying the GaAs surface may help determine the origin of the resonance peaks observed in the data.

5.3.2 Sulfur terminated GaAs

Sulfur termination of GaAs has been known to improve the electrical properties of GaAs devices [33–35]. These electrical measurements have served a proxy to measure the number of surface states present at the surface of a semiconductor. Modifying the surface should reduce the number of surface states and therefore decrease the signal that is seen in the GaAs SH spectrum.

After sulfur treatment the n-type GaAs intensity remains nearly the same as the oxide terminated GaAs. For p-type GaAs the treatment has significantly reduced the amount of surface states leading to a large decrease in the amplitude of the SH spectrum. After the sample is cooled below 200 K there is no peak. This implies that the peak that was seen on the surface of p-type GaAs stems primarily from defects at the oxide-GaAs interface. These defects are partly passivated by sulfur treatment of the GaAs surface. The n-type surface is more intriguing and insightful.

5.3.3 Surface states n-type GaAs

Due to the technological importance of GaAs and the (100) surface there have been many theoretical and experimental studies to try to understand the surface reconstruction and electronic configuration[36–38]. Scanning tunneling microscopy (STM) images have revealed a stark difference between the n-type and p-type surfaces[39–42]. The typical surface reconstruction for GaAs(100) is a 2×4 with an As dimer vacancy in the last row. The As-As dimer bonds are parallel to the $[0\bar{1}1]$ direction while the back bonds of the top As layer to the underlying Ga atoms are along the $[0\overline{11}]$. In p-type GaAs the dimer rows are straight along the $[0\bar{1}1]$ direction. In n-type GaAs the dimer rows are tilted at an angle of about 15° with respect to the $[0\bar{1}1]$ direction. The deviation from the $[0\bar{1}1]$ is the result of a defect formation on highly n-doped ($> 10^{17}$ cm^{-3}) GaAs(100). Fig. 5.13a shows an example of an n-typed GaAs surface doped with silicon at 10^{19} cm^{-3}. The white arrows indicate the formation of the kink defect and the arrows at the bottom denote $[0\bar{1}1]$ crystal direction and the deviation from that direction caused by the kink state.

STM provides evidence of the local structure but is unable to probe long range order. A complementary electron diffraction technique, reflection high energy electron diffraction (RHEED), was used to determine the long range order of n-type GaAs(100) surfaces. RHEED data on n-type GaAs surface observe long range order of two different lattices; one corresponding to the underlying structure of the bulk lattice and the other a superstructure rotated approximately 15° from the $[0\bar{1}1]$ surface[43]. Combined, the STM and RHEED studies strongly indicate the presence of a surface state defect unique to n-type GaAs(100); p-type GaAs shows no signs of this kink state 5.13b.

While the samples used in our SHG studies are highly doped (2.5×10^{18} cm^{-3}) all of the STM and RHEED studies were carried out under UHV conditions with pristine surface; our studies are carried out on oxide surface at ambient pressure under nitrogen gas. However, we may still be able to confirm that the state we are observing is indeed the kink state described in the STM experiments. First, we carried out rotational anisotropy on the n-type samples and plotted the spectra for slices at 25 ps for a few select angles (5.11a). Again the data contain the Fano line shapes, however the ratio of the optical transition matrix elements, q, increases with increasing angle. Most significantly when rotated to 15° we see a significant increase in the ratio of the discrete state to the continuum

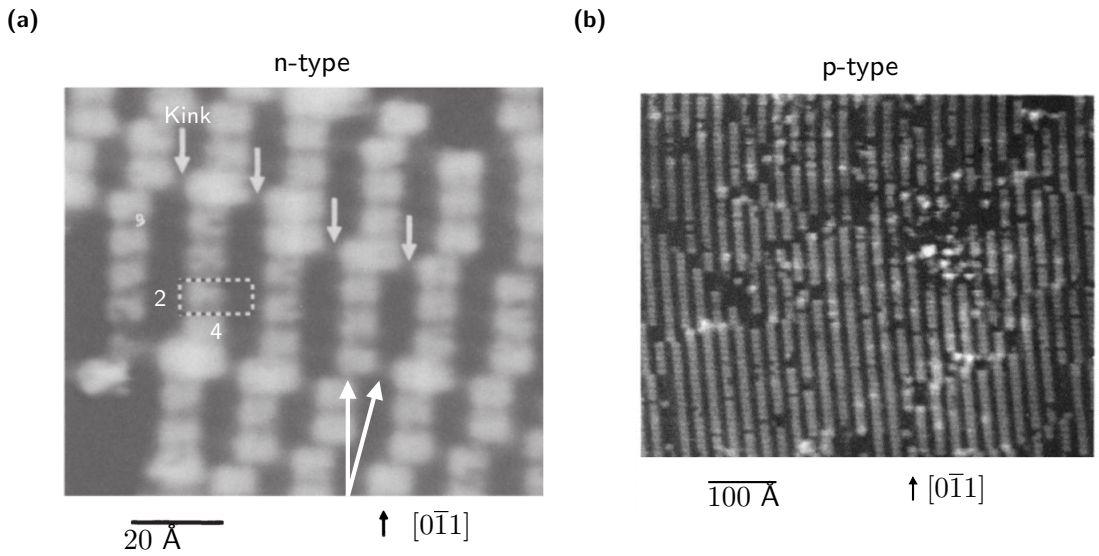

Figure 5.13: STM image of n-and p-type GaAs(100) surfaces with a (4x2) reconstruction the doping density is 10^{19} cm^{-3}. Arrows pointing down indicate kinks(5.13a) while the two white arrows near the bottom indicate the 15° offset of the kinks versus the crystal direction. *Fig. 5.13a adapted from refs. [40] and [41]*

state which yields a much more Lorentizan-like line shape. At this angle we also see a significant reduction in the line width from 0.032 eV along the [0$\bar{1}$1] direction to 0.016 eV at 15° from the [0$\bar{1}$1]. Continued rotation to 25° decreases the ratio of the matrix element of the discrete state to the continuum resulting in a q-parameter of -0.7. The line width and therefore the coupling is nearly the same. At 35° coupling dramatically increases as indicated by the line width $\Gamma = 0.160$ eV. Rotational studies along with the absence of a peak on p-type GaAs provide strong evidence that the state we observe here is the same one which causes the defects and Fermi level pinning on n-type GaAs(100). Surprisingly, we are able to see evidence for an ordered defect even with a native oxide layer under ambient pressures. The suggested origin of this state is the result of a highly doped bulk crystal which suggests that these states may be insensitive to the surface layer. We confirmed this by treating the n-type GaAs with sulfur.

Temperature dependent experiments were carried out in the same manner as before. The pump, probe and detection polarization were all set to excite and measure p-polarized light. The GaAs azimuthal angle was set so that the polarization was aligned along the [0$\bar{1}$1] direction. Data from the sulfur passivated surface contain the same feature as the oxidized surface indicating that

this is indeed a surface defect induced by the bulk doping level. Treatment with sulfur changed the fit parameters a minimal amount. Now that we have identified the origin of the peak as a surface state there is still a question about the coupling.

5.3.4 Coupling of the surface states to a continuum

Fano resonances are the result of the coupling of a discrete state to a continuum. We have identified the discrete state but the continuum could be associated with either the band gap or the E_1 resonance. This ambiguity arises because SHG is a two photon process and the coupling which brings about the Fano resonance may occur with either the first or second photon. However, from chapter 3 we know that for excited state SHG we only observe two pathways of SHG during our pump-probe experiments given by the Feynman pathways in Fig. 3.8. One pathway corresponds to excited state SHG and the other to ground state SHG.

We already know that GaAs has both the band edge and the surface state at the one photon energy of our laser. From chapter 4 we also saw that there is a two photon resonance which corresponds to the E_1 resonance of GaAs. It is possible that the band gap and the surface state provide two competing pathways for SHG generation and by populating the surface state we are able to change the enhancement of the SH generated at the surface. Therefore the two interfering pathways would be the surface state and the bulk band gap and they can interfere during the process to generate SHG.

Additionally there may be other states lying higher in the band gap which provide for additional coupling, however without a theoretical description of the process it is difficult to ascribe any pathway with certainty. From the rotation measurements we can say that the coupling strength (given by Γ) and the line shape (given by the ratio of the transition matrix elements of the discrete and continuum states q) depend on the crystallographic direction. At a rotation of 25° the continuum transition matrix element is greater than the discrete state matrix element which changes the the line shape dramatically.

The rotational dependency may arise from the fact that we are sampling different electronic structure in the surface Brillouin zone when we rotate the sample. The surface band responsible

for the surface states in n-type GaAs may come into a resonance with a bulk band along the $[0\bar{1}0]$ direction which is why we see the complete disappearance of this state. However, to prove this assertion further corroborating evidence is needed from more conventional techniques such as photoelectron spectroscopy.

5.4 Charge transfer from CuPc to GaAs

Organic-inorganic interfaces are of great interest because of their potential in electronics and solar materials. To ensure their usefulness we must be able to determine how they charge transfer and determine where the problems are and suggest ways to improve them either through interfacial engineering or through molecular design. SHG and other even order nonlinear techniques are ideally suited to observe ultrafast events at surfaces and interfaces including charge transfer. By employing broadband spectroscopy we may be able to selectively observe interfacial charge transfer states.

Here we deposit copper phthalocyanine (CuPc) on sulfur passivated p-type GaAs(100) as a model system to observe hole transfer from the GaAs to the CuPc. Sulfur passivated p-type GaAs(100) was the superior choice because the surface states are reduced when compared to sulfur passivated n-type GaAs(100). This gives us a relatively clean interface where we can thermally deposit CuPc in a repeatable fashion. In addition, CuPc has been found to lie with its plane parallel to the GaAs surface[44] indicating a strong interaction which would make this organic-inorganic heterostructure a good candidate for charge transfer. Moreover, previous experiments with ultraviolet photoelectron spectroscopy established the energy level alignment between CuPc and GaAs(100) that is favorable for hole transfer from GaAs to the highest occupied molecular orbital (HOMO) of CuPc[45]. The dynamics of hole transfer was established by single wavelength time resolved SHG[45]. Their experiments are repeated here taking advantage of the broadband spectroscopy to gain a more complete picture of the dynamics of hole transfer.

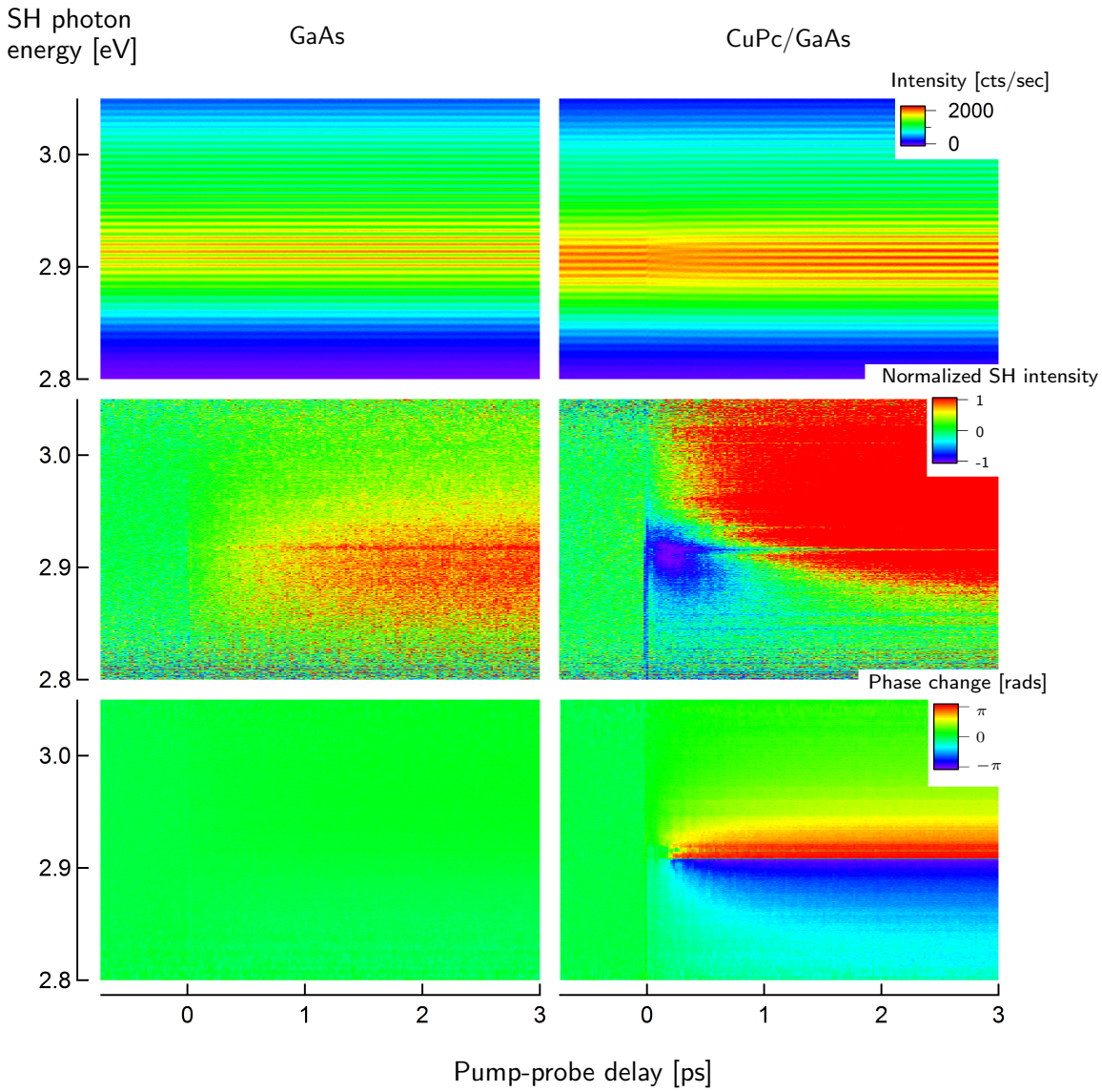

Figure 5.14: Time-resolved interferograms (top) and extracted amplitude (middle) and phase (bottom) of bare sulfur treated p-type GaAs and the same GaAs with CuPc deposited on top. This difference in amplitude and phase between bare GaAs and CuPc/GaAs is a signature of charge transfer.

5.4.1 Sample preparation

Full pump-probe traces are presented in Fig. 5.14. Raw data from the actual interferometric trace is presented for both CuPc/GaAs and GaAs alone. The sample-reference delay, τ, for all data was 0.6 ps. The interferogram with CuPc shows a dramatic change in interference fringes at approximately 200 fs after the pump arrived. These data indicate a large phase shift as a result of excitation of the GaAs. The control sample of only sulfur passivated p-type GaAs shows no change in the fringes with pump-probe delay.

Data from the interferograms can be analyzed further by applying the direct inversion algorithm in section 5.1.1 to extract the time resolved amplitude and phase of the samples. We will first concentrate on the Amplitude data. The most notable difference between the two samples is that the sample with CuPc has a significant amplitude decrease near 200 fs at a photon energy of approximately 2.9 eV. This is in contrast to the control sample which only shows a broad increase in the SH signal. The phase shows even more dramatic behavior.

Phase resolved plots of the SH reveal a massive phase change in the spectral domain of 2π for the sample with CuPc. The location of the higher slope of the phase change is again near 2.9 eV indicating it has some relationship to the amplitude change. Along the pump-probe axis there is a π shift in phase with respect to the unpumped sample. The direction of this shift depends on whether we look at wavelengths above or below the resonance. The large differences in amplitude and phase of the CuPc/GaAs sample and the GaAs provide strong evidence for charge transfer.

The band gap of CuPc is about 1.7 eV but this transition may be broadened. To ensure that we are not exciting both the CuPc and the GaAs we thermally evaporated 20 nm of CuPc onto Aluminum oxide, a thermally conductive large band gap (8.8 eV) insulator, effectively isolating CuPc. Pump-probe traces on this sample show no pump-induced change. Therefore we can conclude that we are only exciting GaAs with our laser.

By taking line slices of the data presented in Fig. 5.14 we can look at cross section of the data near the amplitude minimum 5.15. The transient 'state' seems to be similar to those in the n-type GaAs at rotation angle of 25°.

Most of the data presented here provide solid evidence that there is hole transfer between

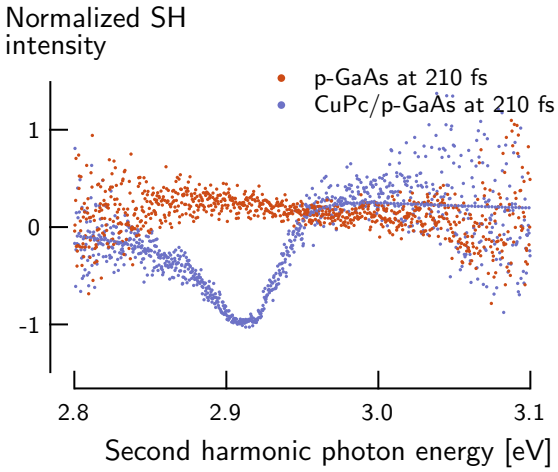

Figure 5.15: Slice of sulfur treated p-type GaAs with CuPc (magenta) and without CuPc (orange) take at 210 fs pump-probe delay.

GaAs and CuPc. However, these data are extremely sensitive to air, exposure time to the laser beam and other variables such as surface passivation. Single wavelength or wavelength integrated traces do not provide enough detail to be able to assign charge transfer for multiple reasons. First, there is the phase change which occurs depending on crystal direction. This is a general phenomena so in order to assign the electric field contribution unambiguously the phase relationship between the static and electric field contributions must be known. In addition, we have to know whether there are any resonances near our probe wavelength. This can dramatically change the intensity of the peak and can carry its own phase. From the data in Fig. 5.14 there is an increase in signal at high energies but a decrease and an increase at lower photon energies. If the data were wavelength integrated the time-domain dynamics could be misinterpreted.

However, with this new technique we are able to ascertain time resolved states that are transiently excited. In the case of the n-type GaAs we have spectroscopically characterized a transiently populated surface state unique to the n-type GaAs surface. We believe that this state is associated with the structural defects observed in STM and RHEED data. This state is populated for over 700 ps indicating that the life time is convergent on life times for trap states in GaAs. We can also detect transient surface states resulting from a heterojunction which was one of the goals of this thesis. This transient state is short lived and only apparent if we analyze the full spectra. The phase shifts also help ascertain a state and its coupling. By analyzing the line shapes with

a Fano formula we can tell further information about the coupling of the excited state and other states by the line shape and width of the spectra. This also helps us ascertain the origin of the Fano resonance.

Wider applicability of the the time resolved second harmonic spectral interferometry technique detailed here can only take place if we can confidently assign the spectral features and develop a theoretical frame work to analyze the data. In the final chapter we identify experiments that can help corroborate spectral features from SHSI. Suggestions for improving the experiment are also provided.

References

1. Lepetit, L., Chériaux, G. & Joffre, M. "Linear techniques of phase measurement by femtosecond spectral interferometry for applications in spectroscopy." *Journal of the Optical Society of America B* **12,** 2467 (1995).

2. Millane, R. P. & Hsiao, W. H. "On apparent counterexamples to phase dominance." *Journal of the Optical Society of America. A, Optics, image science, and vision* **20,** 753–756 (2003).

3. Millane, R. P. & Hsiao, W. H. "The basis of phase dominance." *Optics letters* **34,** 2607–2609 (2009).

4. Trebino, R. *et al.* "Measuring ultrashort laser pulses in the time-frequency domain using frequency-resolved optical gating." *Review of Scientific Instruments* **68,** 3277 (1997).

5. Lozovoy, V. V., Pastirk, I. & Dantus, M. "Multiphoton intrapulse interference. IV. Ultrashort laser pulse spectral phase characterization and compensation." *Optics letters* **29,** 775–777 (2004).

6. Fittinghoff, D. N. *et al.* "Measurement of the intensity and phase of ultraweak, ultrashort laser pulses." *Optics letters* **21,** 884–886 (1996).

7. Dorrer, C., Belabas, N., Likforman, J.-P. & Joffre, M. "Spectral resolution and sampling issues in Fourier-transform spectral interferometry." *Journal of the Optical Society of America B* **17,** 1795 (2000).

8. Wilson, P. T. *Second-harmonic generation spectroscopy using broad bandwidth femtosecond pulses.* PhD thesis (University of Texas at Austin, 2000).

9. Wilson, P. T., Jiang, Y, Aktsipetrov, O. a., Mishina, E. D. & Downer, M. C. "Frequency-domain interferometric second-harmonic spectroscopy." *Optics Letters* **24,** 496–498 (1999).

10. Wilson, P. T., Jiang, Y., Carriles, R. & Downer, M. C. "Second-harmonic amplitude and phase spectroscopy by use of broad-bandwidth femtosecond pulses." *Journal of the Optical Society of America B* **20,** 2548 (2003).

11. Nelson, C. A. *et al.* "Time-, energy-, and phase-resolved second-harmonic generation at semiconductor interfaces." *The Journal of Physical Chemistry C* **118,** 27981–27988 (2014).

12. Carriles, R., An, Y. Q. & Downer, M. C. "Frequency-domain measurement of second harmonic phase." *physica status solidi (b)* **242,** 3001–3006 (2005).

13. An, Y., Carriles, R. & Downer, M. "Absolute phase and amplitude of second-order nonlinear optical susceptibility components at Si(001) interfaces." *Physical Review B* **75,** 241307 (2007).

14. Shen, Y. R. "Phase-sensitive sum-frequency spectroscopy." *Annual review of physical chemistry* **64,** 129–50 (2013).

15. Li, M. *et al.* "Photo-induced denitrogenation of triazoline moieties for efficient photo-assisted poling of electro-optic polymers." *Polymer Chemistry* **4,** 4434 (2013).

16. Fano, U. "Effects of Configuration Interaction on Intensities and Phase Shifts." *Physical Review* **124,** 1866–1878 (1961).

17. Garton, W. R. S. & Codling, K. "Ultra-violet Extensions of the Arc Spectra of the Alkaline Earths: The Absorption spectrum of barium vapour." *Proceedings of the Physical Society* **75,** 87 (1960).

18. Madden, R. P. & Codling, K. "New autoionizing atomic energy levels in He, Ne, and Ar." *Physical Review Letters* **10,** 516–518 (1963).

19. Fano, U & Cooper, J. "Spectral distribution of atomic oscillator strengths." *Reviews of Modern Physics* **40,** 441 (1968).

20. Rost, J. M., Schulz, K, Domke, M & Kaindl, G. "Resonance parameters of photo doubly excited helium." *Journal of Physics B: Atomic, Molecular and Optical Physics* **30,** 4663–4694 (1997).

21. Liu, Z. *et al.* "Room-temperature Fano resonance tunable by chemical doping in few-layer graphene synthesized by chemical-vapor deposition." *Phys. Rev. B* **82,** 155435 (15 2010).

22. Kroner, M *et al.* "The nonlinear Fano effect." *Nature* **451,** 311–314 (2008).

23. Fan, J. A. *et al.* "Self-assembled plasmonic nanoparticle clusters." *Science* **328,** 1135–1138 (2010).

24. Glutsch, S., Siegner, U., Mycek, M.-A. & Chemla, D. S. "Fano resonances due to coupled magnetoexciton and continuum states in bulk semiconductors." *Phys. Rev. B* **50,** 17009–17017 (23 1994).

25. Siegner, U., Mycek, M., Glutsch, S. & Chemla, D. "Ultrafast coherent dynamics of Fano resonances in semiconductors." *Physical Review Letters* **74,** 470–473 (1995).

26. Bar-Ad, S., Kner, P., Marquezini, M. V., Mukamel, S. & Chemla, D. S. "Quantum confined Fano interference." *Physical Review Letters* **78,** 1363–1366 (1997).

27. Miroshnichenko, A. E., Flach, S. & Kivshar, Y. S. "Fano resonances in nanoscale structures." *Reviews of Modern Physics* **82,** 2257–2298 (2010).

28. Agarwal, G. S., Haan, S. L. & Cooper, J. "Radiative decay of autoionizing states in laser fields. I. General theory". *Physical Review A* **29,** 2552–2564 (1984).

29. Meier, T., Schulze, A., Thomas, P., Vaupel, H. & Maschke, K. "Signatures of Fano resonances in four-wave-mixing experiments." *Physical Review B* **51,** 13977–13986 (1995).

30. Blakemore, J. "Semiconducting and other major properties of gallium arsenide." *Journal of Applied Physics* **53,** R123–R181 (1982).

31. Sturge, M. "Optical Absorption of Gallium Arsenide between 0.6 and 2.75 eV." *Physical Review* **127,** 768–773 (1962).

32. Tanaka, H., Mizutani, G. & Ushioda, S. "A new resonance of the surface SHG from GaAs(001) in air." *Surface Science* **402-404,** 533–536 (1998).

33. Yablonovitch, E., Sandroff, C. J., Bhat, R. & Gmitter, T. "Nearly ideal electronic properties of sulfide coated GaAs surfaces." *Applied Physics Letters* **51,** 439 (1987).

34. Paget, D., Gusev, a. & Berkovits, V. "Sulfide-passivated GaAs (001). II. Electronic properties". *Physical Review B* **53,** 4615–4622 (1996).

35. Ohno, T. "Sulfur passivation of GaAs surfaces." *Physical Review B* **44,** 6306–6311 (1991).

36. Ohtake, A. "Surface reconstructions on GaAs(001)." *Surface Science Reports* **63,** 295–327 (2008).

37. Schmidt, W. & Bechstedt, F. *Geometry and electronic structure of GaAs(001)(24) reconstructions.* 1996.

38. Wang, W., Lee, G., Huang, M., Wallace, R. M. & Cho, K. "First-principles study of GaAs(001)-β2(24) surface oxidation and passivation with H, Cl, S, F, and GaO." *Journal of Applied Physics* **107,** 103720 (2010).

39. Pashley, M. D. & Haberern, K. W. "Compensating surface defects induced by Si doping of GaAs." *Physical Review Letters* **67,** 2697–2700 (1991).

40. Pashley, M. D. & Haberern, K. W. in *Semiconductor Interfaces at the Sub-Nanometer Scale* 001, 63–73 (1993).

41. Pashley, M. D., Haberern, K. W., Feenstra, R. M. & Kirchner, P. D. "Different Fermi-level pinning behavior on n- and p-type GaAs(001)." *Physical Review B* **48,** 4612–4615 (1993).

42. Pashley, M. D. & Srivastava, G. P. *STM Studies of Fermi-Level Pinning on the GaAs(001) Surface [and Discussion].* 1993.

43. Sugawara, A., Fujieda, K. & Otsuka, N. "Long period reconstruction of GaAs(001) surface." *Surface Science* **394,** L174–L178 (1997).

44. Berkovits, V. L., Gordeeva, A. B., Kosobukin, V. A. & Terukov, E. I. "Studying structure of thin copper phthalocyanine films by reflectance anisotropy spectroscopy." *Technical Physics Letters* **38,** 286–289 (2012).

45. Park, H, Gutierrez, M, Wu, X, Kim, W & Zhu, X.-Y. "Optical Probe of Charge Separation at Organic/Inorganic Semiconductor Interfaces." *The Journal of Physical Chemistry C* **117,** 10974–10979 (2013).

6

Conclusions and Future Outlook

Having precise ideas often leads to a man doing nothing.

— Paul Valéry

The previous chapters have walked though the need for a technique which can selectively probe surfaces and interfaces. Second harmonic and other even order nonlinear techniques are ideally suited for this task. However, difficulties arise because of the many contributions in the SH signal which greatly complicates the assignments of charge transfer from transient data. The spectral resolved techniques introduced in the final two chapters attempt to address this difficulty, but interpretation still remains difficult.

In spite of the difficulty of assigning spectral features we were able to make claims concerning dynamics of the bulk band gap and the rotational dependence in chapter 4. In chapter 5 we were able to demonstrate that phase is extremely important in interpreting time resolved SH data. In fact, the signal can rise or fall depending on the phase of the bulk component. GaAs(100) was ideal to observe this effect because the two crystal directions are 180° out of phase with each other. We can also control the doping to switch the field direction. These studies revealed that an increase in SH signal only indicates a final signal amplitude increase or decrease that can be effected by the interference between the static SH and electric field. While the idea of interference is not necessarily new, the direct measure of the phase in a pump-probe experiment with spectral resolution has only been accomplished recently[1].

To add to the complications of interpreting the signal there are spectral features that occur as either the one photon, two photon or both the one and two photon energy. These can reveal spectral features which can obscure dynamics of interest. If a quantitative measure of charge transfer is also desired the magnitude will matter. And if there are any resonances near the fundamental or second harmonic wavelength the intensity of the SH can vary greatly. While there are further complications the technique presented here can begin to provide insight into charge transfer mechanisms and surface states. This chapter concludes the thesis with recommendations for going forward with these types of experiments. They cover what needs to be done to turn this technique into a full-blown analytical technique akin to photo electron spectroscopies without the need to for ultra high vacuum (UHV)

6.1 Proving surface state assignments and momentum resolution

We cannot completely discount UHV and photoelectron spectroscopies right away. First, we need to draw a one-to-one correlation between the features we see in SH spectroscopy with those observed in ultraviolet photo emission (UPS) and two photon photo emission (2PPE). UPS should enable us to assign any static features in our samples but what we are really interested in are the surface state features observed on n-type GaAs wafers. In order to ascertain the origin of these features we need to carry out the same experiments presented in this thesis in UHV while at the same time using 2PPE to provide independent confirmation of these states and their assignment. In addition, the momentum resolution that photoemission provides will allow us to determine the origin of the Fano line shapes which have pervaded the data.

Once we are confident in the assignments we need a thorough grounding in theory so that the spectral features can be simulated using known details about the materials. Some ideas for how the experiment can be interpreted through the framework of nonlinear optics was presented in chapter 3. These ideas can be taken one step further to provide a density matrix description of the experiment which would allow for basic simulations of the data. This provides another check of the validity of the data and the interpretation.

6.2 Improving the experiment

All of the data in this thesis were collected with a home built oscillator with its central wavelength essentially fixed at 1.5 eV. This lack of tunability is a terrible handicap for confirming interpretations and for investigating novel and relevant systems. These experiments call for two independently tunable laser beams of ultrabroadband width of at least 100 meV FWHM. Two independently tunable ultrafast lasers will allow for the tuning of a pump beam at the band edge of a material and the center wavelength of the probe beam can be tuned across the material generating a complete excited state SH spectrum of the material of interest. This could include the energetic levels of interface states in bilayers although some line shape analysis could also reveal coupling of states.

Further improvement and even more information can be obtained by generating two pump pulses with a pulse shaper. This will be a two dimensional implementation of SH spectroscopy. A vibrational version of 2D-SFG has been implemented but has yet to make it to the electronic domain. This is where many of the electronic processes that govern solar cell functionality take place. Particulate charge trapping and transfer. A 2D electronic spectroscopy that is sensitive to an interface will yield unprecedented access to interfacial electronic states and could revolutionize the way we investigate and understand charge transfer at surfaces and interfaces.

6.3 What it all means

This thesis demonstrates a new technique which is able to selectively observe spectra from surface states. While the main material studied was GaAs the spectral signatures of surface states and the coupling of those states to a continuum should be observable for a wide variety of systems. As long as there is an ultrashort pulse which encompasses the desired spectral range it should be simple to use this experiment for a multitude of studies.

With this new technique it should be possible to better assign surface state transitions at ambient operating temperatures as well as at buried interfaces. This could allow for unambiguous determination of surface states and the ability to detect if those states have diminished as a result of some passivation scheme. This is far better than observing electrical properties which do not

directly interrogate surface states[2].

Furthurmore, dynamics of surfaces can be studied as we showed with the CuPc/GaAs interface. This gives unprecedented detail as to the time dynamics. Most importantly, this technique allows for some measure of the coupling strength of the charge transfer event. With coupling information it will be much easier to study and understand charge transfer rates. This is an exciting opportunity in surface physics that should not be overlooked.

References

1. Nelson, C. A. *et al.* "Time-, energy-, and phase-resolved second-harmonic generation at semiconductor interfaces." *The Journal of Physical Chemistry C* **118,** 27981–27988 (2014).

2. Ohno, T. "Sulfur passivation of GaAs surfaces." *Physical Review B* **44,** 6306–6311 (1991).

Appendices

A

TR-FDISH setup details

The data for the oscillator parameters is presented in this appendix along with the complete optical setup including a description of all of the optics used in the beam path and the equipment used to acquire the data.

The oscillator power stability is shown in Fig. A.1. The stability is 0.6 % RMS over the 7 hour period measured here which is much longer than the duration of any of the experiments. The repetition rate was also measured giving a round trip time in the oscillator of 12.8 ns corresponding to a 78 MHz repetition rate. At an output power of 550 mW this corresponds to about 7.5 nJ per pulse.

Pulse durations were measured using FROG and the intensity and the phase of the pulses were retrieved only the intensity auto-correlations are displayed here but they are a good representation of the pulses out of the oscillator and at the sample. The intensity auto-correlation out of the oscillator was measured by generating SH in a beta-barium borate crystal. At the sample the intensity auto-correlation was measured at the sample position with a piece of z-cut quartz. The full width at half maximum (FWHM) on the graphs corresponds to the FWHM of the intensity auto correlation assuming a Gaussian pulse we can divide the FWHM by $\sqrt{(2)}$ to get the pulse duration. The pulse duration out of the oscillator is then 30 fs while the pulse at the sample is 21 fs in duration. Since the pulse is more sech^2 the pulses are actually slightly shorter.

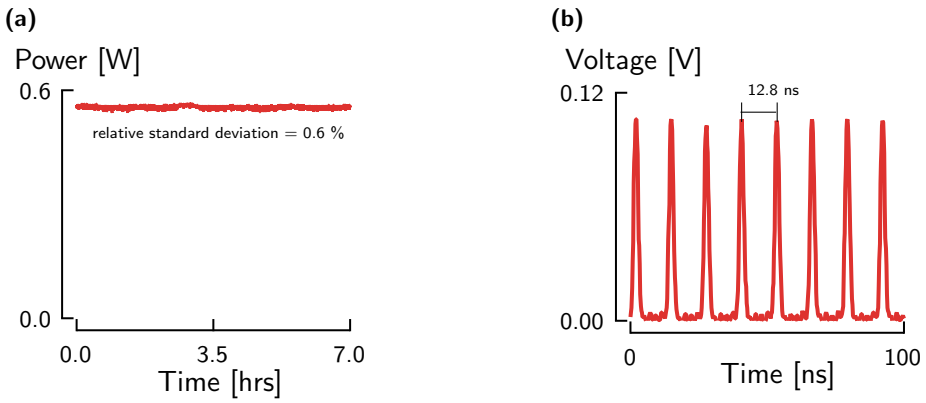

Figure A.1: Power stability and repetition rate of the home built oscillator.

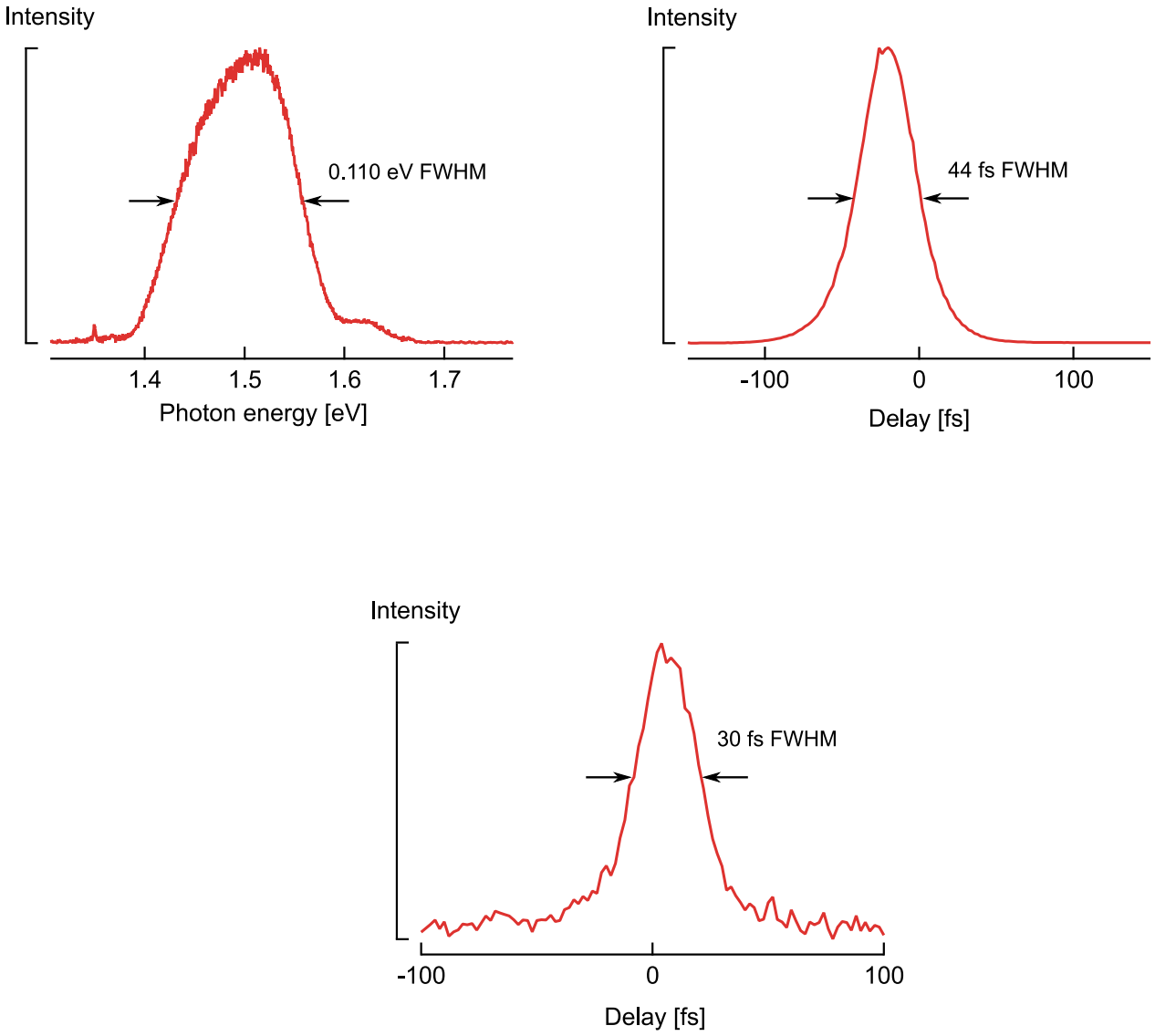

Figure A.2: Top row: Spectrum of the femtosecond pulse out of the oscillator measured with an ocean optics USB2000 spectrometer. Pulse duration from an intensity auto-correlation measurement in a Beta-barium borate crystal at the output of the oscillator. Bottom row: auto-correlation of the laser pulse at the sample with the GaAs being replaced by z-cut quartz.

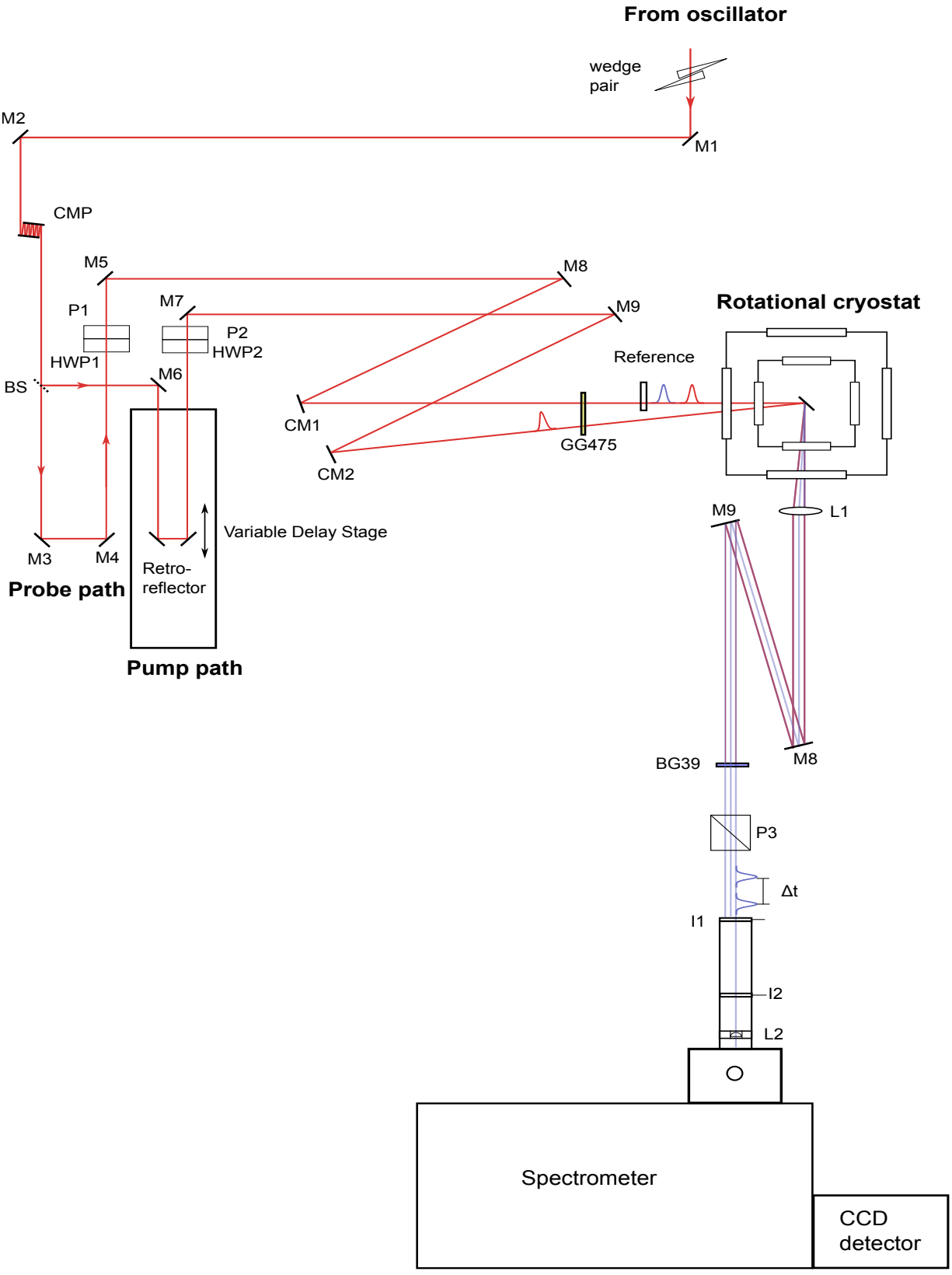

Figure A.3: Full TR-FDISH setup with all of optical elements included. A complete list of optical elements is given in the table below.

TR-FDISH setup: Optics

Diagram Label	Optic	Details	Company	Part Number
Wedge pair	CaF_2 wedge pair	1.4 mm thick Wedge angle 4°	Venteon	N/A
M1-M2	Mirror	1" protected silver mirror for femtosecond applications	Venteon	N/A
M3-M9	Mirror	½" protected silver mirror for femtosecond applications	Venteon	N/A
CMP	Chirped Mirror Pair	ultra-broadband (600-1200nm) dispersion compensating mirror pair >99.9 % reflectivity	Venteon	DCM7
BS	Beam splitter	67:33 (R:T) 1 mm thick	Layer Tec	104041
Retro reflector	Retro reflector	Broadband Hollow Retro reflector, 1.0 in, 2 arc sec parallelism, 450-10,000 nm	Newport	UBBR1-2S
HWP1-HWP2	Half Wave Plate	Zero order Quartz half wave plate (830 nm)	Thor Labs	WPH05M-830
P1-P2	Polarizer	Polarcor polarizer (740 – 860 nm)	Newport	10P109AR.16
CM1 – CM2	Concave Mirror	½"protected silver mirrors 250 mm FL	Newport	05DC500ER.2
GG475	Colored Glass Filter	Colored Glass Filter LWP Cut on 475 nm	Newport	FSR-GG475
L1	Lens 50 mm FL	25.4 mm lens UV-Visible antireflective coated	Thorlabs	LA1131-A
BG39	Colored Glass Filter	Blue Band Pass filter (transmits 0.01% of 800nm)	Newport	FSR-BG39
I1 – I2	Irises	Lens Tube Mounted Irises SM1 internal and external threads	Thor Labs	SM1D12
L1	Lens	Aspheric Lens Mounted (M9 threads) –A (UV) coated K59 Glass	Thor Labs	A220TM-A
reference	Glass slide	Glass slide coated with poled polymer reference sample	N/A	N/A
M8-M9	Broadband dielectric mirrors	Broadband anti-reflective mirrors for 400 nm	Thorlabs	BB-E01

Table A.1: Optics list for TR-FDISH experiment

TR-FDISH setup: Equipment

Diagram Label	Equipment	Details	Company	Part Number
Spectrometer	Acton sp-2300i	Equipped with 1200 lines/mm grating blazed at 300 nm	Princeton Instruments	sp-2300i
CCD	LN-cooled pylon CCD	1340x400 pixel detector 20x20 um per pixel	Princeton Instruments	Pylon 1300B
Variable delay stage	Variable delay stage	150 mm Motorized Linear Translation Stage, Stepper Motor	Thor Labs	NRT150
Rotational cryostat	Vapor rotational cryostat	Temp range 1.5 – 325 K Custom rotation stage added to control rotation	Janis	STVP-100
Rotation stage (not on diagram)	Motorized rotation stage	Rotation stage for SM1 optics mounted to cryostat with custom adapter	Thor Labs	PRM1Z8E

Table A.2: Equipment list for TR-FDISH experiment

B

Rotational anisotropy

This appendix derives the expressions for rotational anisotropy given in chapter 4. Helpful material concerning tensors and there properties can be found in [1–3]. Much of the material presented here was derived with help from these resources. We begin with the rotational anisotropy of the bulk tensor and then move on the the electric field tensor. The general framework used for the rotations can be applied to any material system as long as the symmetry of the crystal is known. Boyd [1] is a very useful resource when determining which tensor elements are 0 or equal, which reduces the over all problem.

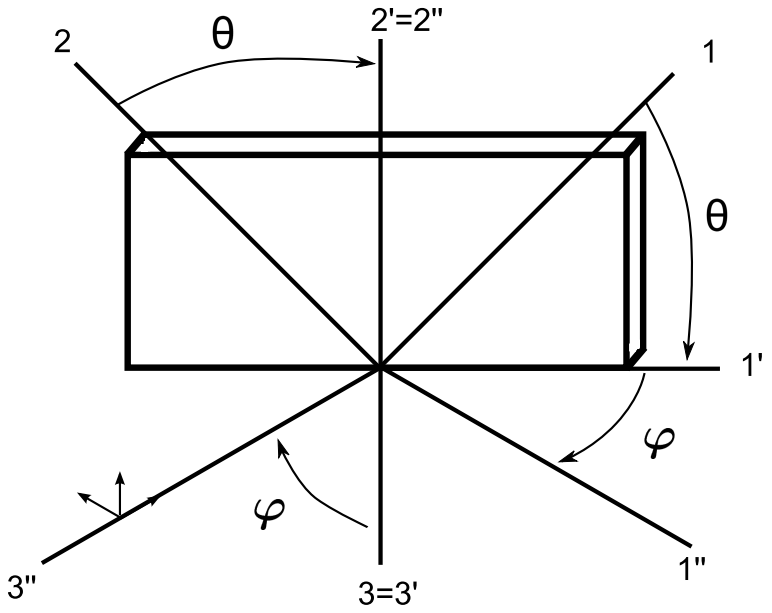

Figure B.1: Definition of matrix rotations. The directions 1 and 2 correspond to the crystal directions [010] and [001] while direction 3 is the [100] direction.

B.1 Rotational anisotropy equations for GaAs(100)

The third rank tensor describing the second order nonlinear effects contains 27 tensor elements and can be represented as a 3-D matrix. The three different layers are described in Eq. B.1

$$\chi^{(2)}_{ijk} = \left(\begin{pmatrix} \chi_{111} & \chi_{112} & \chi_{113} \\ \chi_{121} & \chi_{122} & \chi_{123} \\ \chi_{131} & \chi_{132} & \chi_{133} \end{pmatrix} \begin{pmatrix} \chi_{211} & \chi_{212} & \chi_{213} \\ \chi_{221} & \chi_{222} & \chi_{223} \\ \chi_{231} & \chi_{232} & \chi_{233} \end{pmatrix} \begin{pmatrix} \chi_{311} & \chi_{312} & \chi_{313} \\ \chi_{321} & \chi_{322} & \chi_{323} \\ \chi_{331} & \chi_{332} & \chi_{333} \end{pmatrix} \right) \tag{B.1}$$

We can reduce the number of tensor elements by considering the crystal symmetry. For GaAs which is a crystal with $\bar{4}3m$ (T_d) symmetry which implies that all tensor elements vanish except for

$xyz = xzy = yzx = yxz = zxy = zyx$ [1] which is reflected in the tensor by removing the proper elements for the overall $\chi^{(2)}$ in Eq. B.1. The reduced tensor is then

$$\chi^{(2)}_{ijk} = \left(\begin{pmatrix} 0 & 0 & 0 \\ 0 & 0 & \chi_{123} \\ 0 & \chi_{132} & 0 \end{pmatrix} \begin{pmatrix} 0 & 0 & \chi_{213} \\ 0 & 0 & 0 \\ \chi_{231} & 0 & 0 \end{pmatrix} \begin{pmatrix} 0 & \chi_{312} & 0 \\ \chi_{321} & 0 & 0 \\ 0 & 0 & 0 \end{pmatrix} \right). \tag{B.2}$$

While all the tensors entries are equal by symmetry we will keep the subscripts so that we can define their location within the tensor. All of the tensor entries are in the crystal coordinate system and need to be rotated into the lab frame to derive expressions for the rotational anisotropy.

To rotate the tensor we first need to define a rotation matrix that brings the crystal frame into the lab frame. Instead of Cartesian coordinates x, y and z we will use numerical indices 1, 2 and 3. This will make it easier to keep track of the coordinate system and its transformations. First we define 3 to be pointing along the surface normal of GaAs. Then 1 and 2 are in the plane and arrange such that they form a right handed coordinate system.

We can now define two rotation matrices which rotate the coordinate system.[1] One which rotates in plane about 3 and another which rotates about the $2'$. The first rotation matrix is a clockwise rotation about 3 and is

$$a_{ij} = R(\theta) = \begin{pmatrix} \cos(\theta) & -\sin(\theta) & 0 \\ \sin(\theta) & \cos(\theta) & 0 \\ 0 & 0 & 1 \end{pmatrix} \tag{B.3}$$

[1] We are rotating the coordinate system not the vector therefore the rotation matrices defined here and the ones which rotate a vector are different.

The subsequent rotation is about the $2'$ axis and is

$$c_{ij} = R(\varphi) = \begin{pmatrix} \cos(\varphi) & 0 & \sin(\varphi) \\ 0 & 1 & 0 \\ -\sin(\varphi) & 0 & \cos(\varphi) \end{pmatrix} \tag{B.4}$$

We can multiply these two matrices together. We need to remember that these matrices are operators and multiplication in non-commutative for operators. So the order of the rotations matters. First we will rotate $R_1(\theta)$ and then $R_2(\varphi)$ which is then

$$c_{ik} = a_{ij}b_{jk} = R(\varphi,\theta) = \begin{pmatrix} \cos(\varphi) & 0 & \sin(\varphi) \\ 0 & 1 & 0 \\ -\sin(\varphi) & 0 & \cos(\varphi) \end{pmatrix} \begin{pmatrix} \cos(\theta) & -\sin(\theta) & 0 \\ \sin(\theta) & \cos(\theta) & 0 \\ 0 & 0 & 1 \end{pmatrix} \tag{B.5}$$

Multiplying gives

$$c_{ik} = R(\varphi,\theta) = \begin{pmatrix} \cos(\varphi)\cos(\theta) & -\cos(\varphi)\sin(\theta) & \sin(\varphi) \\ \sin(\theta) & \cos(\theta) & 0 \\ -\cos(\theta)\sin(\varphi) & \sin(\theta)\sin(\varphi) & \cos(\varphi) \end{pmatrix} \tag{B.6}$$

Now that we have defined a rotation matrix for the two desired rotation we can operate on the tensor rotating it from the crystal frame into the lab frame. The operations is given as

$$\chi'^{(2)}_{ijk} = a_{il}a_{jm}a_{kn}\chi^{(2)}_{lmn} \tag{B.7}$$

Here a is the rotation matrix defined in Eq. B.6. It operates three times on the tensor each time transforming one of the indicies from the crystal coordinates into the lab coordinates. The lab coordinates are defined as $\chi^{(2)'}_{ijk}$ and the crystal coordinates $\chi^{(2)}_{lmn}$. This is a very tedious calculation so a mathematics program is the best bet for this rotation. In Mathematica this code looks like this:

$$\chi' = \mathsf{Transpose}[\mathsf{a.Transpose}[(\mathsf{a.Transpose}[(\mathsf{a.Transpose}[\chi, 3, 2, 1]), 2, 1, 3]), 3, 2, 1], 1, 3, 2] \ .$$

In our geometry the angle of incidence is $\varphi = 45°$ and does not move so with this in mind we can

write the full second order tensor as

$$\chi'^{(2)}_{ijk} = \begin{pmatrix} \begin{pmatrix} \sin(2\theta) & \cos(2\theta) & 0 \\ \cos(2\theta) & \sin(\theta) & 0 \\ 0 & 0 & 0 \end{pmatrix} \\ \begin{pmatrix} \cos(2\theta) & \sin(2\theta) & 0 \\ \sin(2\theta) & 0 & 0 \\ 0 & 0 & 0 \end{pmatrix} \\ \begin{pmatrix} 0 & 0 & 0 \\ 0 & 0 & 0 \\ 0 & 0 & 0 \end{pmatrix} \end{pmatrix} \tag{B.8}$$

Again all of the entries that have a three in the index entry are zero because they correspond to a nonphysical situation where and electric field vector is pointing along the direction of propagation these entries are set to zero.

The output is another 3D matrix with many entries however taking into account the physicality of the situation we only need eight entries of this matrix. Since only the electric field vector can interact with the material and the electric field is orthogonal to the direction of propagation then any element that contains an index of 3 is automatically zero because we cannot have any electric field in that direction. The electric field vectors are aligned with either 1 or 2. If aligned with 2 then the electric field is polarized parallel to the surface and is termed s-polarized light. If the electric field is polarized in the 1 direction then we have p-polarized light. Using these definitions we can choose the entries in our rotated tensor which correspond to Pin-Pout, P_{in}-S_{out}, S_{in}-P_{out}, S_{in}-S_{out}. This is for a transmission geometry but this should hold for the reflection geometry. We have neglected the Fresnel factors which may play a role between differences in the intensity for reflected and transmitted SH.

We should also note that all of these derivations relate the principle crystal axes, [010] and [001], and the tensor components related. From the matrix we see that the most signal for P_{in}-P_{out} is along the [011] directions. All of the data in chapter 4 is referenced to these directions. So all we

need to do is rotate by 45° which is then $\sin(2(\theta+45)) = \sin(2\theta+90) = \cos(2\theta)$. Which are the equations given in chapter 4.

B.2 Electric field induced second harmonic

The same analysis can be done for the electric field induced SH. $\chi^{(3)}_{ijkl}$ for $\bar{4}3m$ structure has unique elements $iiii$, $iijj$, $ijij$, $ijji$ when contracted with an electric field in the 3 direction (the surface normal direction) then we are left with 333, 223 = 113, 131 = 232, 311 = 322. The contracted tensor for electric field induced SHG from GaAs (100) is

$$\chi^{\prime(2)DC}_{ijk} = \begin{pmatrix} \begin{pmatrix} 0 & 0 & \chi_{131} \\ 0 & 0 & 0 \\ \chi_{113} & 0 & 0 \end{pmatrix} \\ \begin{pmatrix} 0 & 0 & 0 \\ 0 & 0 & \chi_{232} \\ 0 & \chi_{223} & 0 \end{pmatrix} \\ \begin{pmatrix} \chi_{311} & 0 & 0 \\ 0 & \chi_{322} & 0 \\ 0 & 0 & \chi_{333} \end{pmatrix} \end{pmatrix} \tag{B.9}$$

After this tensor has been rotated into the laboratory frame the tensor is then

$$\chi_{ijk}^{\prime(2)DC} = \left(\begin{pmatrix} c & 0 & 0 \\ 0 & c & 0 \\ 0 & 0 & 0 \end{pmatrix} \begin{pmatrix} 0 & c & 0 \\ c & 0 & 0 \\ 0 & 0 & 0 \end{pmatrix} \begin{pmatrix} 0 & 0 & 0 \\ 0 & 0 & 0 \\ 0 & 0 & 0 \end{pmatrix} \right) \tag{B.10}$$

where c denotes a constant with respect the the azimuthal angle θ. There fore there should be no variation in the electric field contribution with rotation. This component however does interfere with the bulk contribution. Furthermore, by changing the angle of incidence we can control the projection for the electric field onto these tensor elements. So by changing the incident angle, φ, we can change the electric field contribution. This may be one way to quantify the near surface electric field. Especially if we can normalize out the static contributions as in a pump probe experiment.

References

1. Boyd, R. *Nonlinear Optics.* Third Edit (Elsevier, New York, 2008).
2. Nye, J. F. *Physical Properties of Crystals* (Oxford University Press, 1955).
3. Byron, F. W. & Fuller, R. W. *Mathematics of Classical and Quantum Physics* (Dover, 1992).

C

Direct inversion

C.1 The Fourier transform and data analysis

Windowing the right peak to obtain the correct sign of the phase can be a difficult task which is made even more difficult by of the prevalence of different Fourier transform definitions in different fields. Using one over the other can explicitly effect the sign of the recovered phase. The most general Fourier transform can be written as[1]

$$F(\omega) = \sqrt{\frac{|b|}{2\pi^{1-a}}} \int_{-\infty}^{\infty} f(t) \mathrm{e}^{ib\omega t} dt \tag{C.1}$$

where a and b take on different values according to the definition preferred by a specific field. The values, fields and their coefficients and exponents are given in table C.1. All of the definitions in

a	b	Discipline	Coefficient	Exponent
0	1	Modern physics	$\sqrt{\frac{1}{2\pi}}$	$\mathrm{e}^{i\omega t}$
1	-1	Pure mathematics	1	$\mathrm{e}^{-i\omega t}$
-1	1	Classical physics	$\frac{1}{2\pi}$	$\mathrm{e}^{i\omega t}$
0	2π	Signal Processing	1	$\mathrm{e}^{-i2\pi\omega t}$

Table C.1: Fourier transform definitions and the disciplines they are used in.

table C.1 are forward Fourier transforms; reverse transforms just change the sign in the exponent

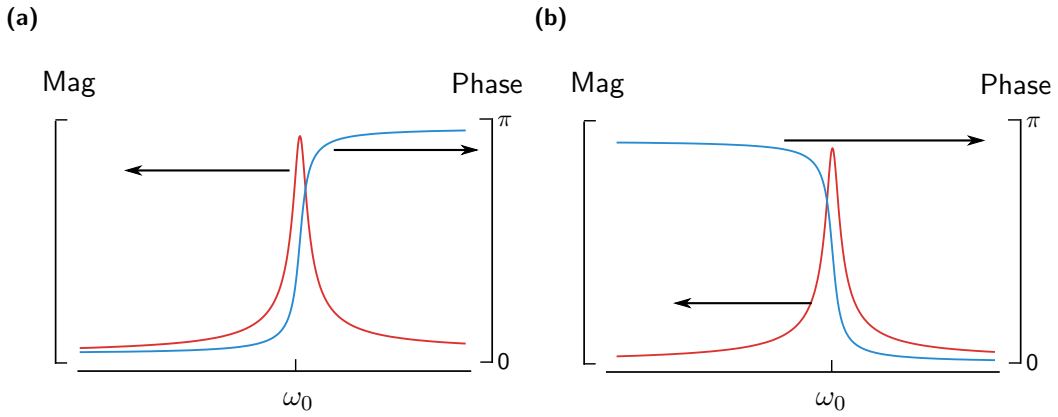

Figure C.1: Fourier transform of Eq. C.2 using the physics definition C.1a and the signal processing definition C.1b The phases have the opposite sign.

and also require a change in the coefficient. As can be seen from the table the Fourier transform definitions have a sign change in the exponent. This is important when we are considering phase of our signal because different definitions lead to different signs of the phase.

As an example we will consider and exponentially damped oscillator driven by an delta-function impulse. Equation of motion for the oscillator has the form

$$f(t) = \theta(t)\mathrm{e}^{-\frac{t}{\tau}}\cos(\omega t) \tag{C.2}$$

where $\theta(t)$ is the Heaviside theta function which has values of 0 for $t < 0$ and 1 for $t > 0$. This enforces causality on the system. τ is the decay constant of the exponential and is related to damping forces in the system and ω is the angular frequency of the oscillator and is equal to $\omega = 2\pi\nu$.

Using the definition of modern physics or classical physics the Fourier transform of Eq. C.2 has the form

$$F(\omega) = -\frac{A}{\omega_0 + \omega + i\gamma} + \frac{A}{\omega_0 - \omega - i\gamma}. \tag{C.3}$$

Howeverm when we use the signal processing convention the Fourier transform has the form

$$F(\omega) = -\frac{A}{\omega_0 - \omega + i\gamma} + \frac{A}{\omega_0 + \omega - i\gamma} \tag{C.4}$$

which is just the complex conjugate of Eq. C.3. The amplitude and phase of Eqs. C.3 and C.4 are plotted in Fig. D.2

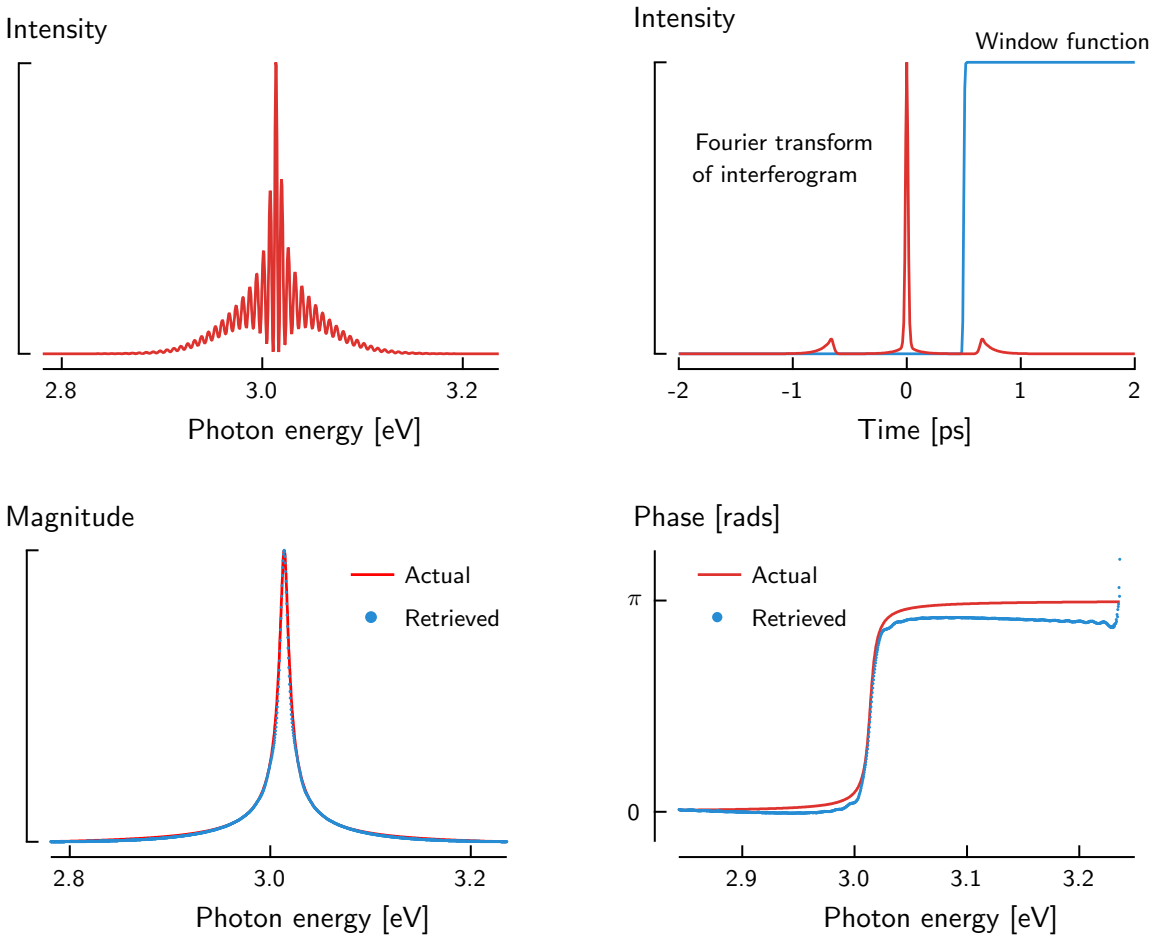

Figure C.2: Sequency used to test the direct inversion algorithm used for recovering the amplitude and phase of a unknown pulse. Amplitude retrival is very good whereas there are some residual phase artifacts.

It can be seen from the plots that the amplitudes using either method remain unchanged but the phase is different. The physics definition is preferable since the phase has the physical significance of the relationship of the motion to the driving force. At low frequencies the oscillator is in phase with the driving force. Then as the frequency of the driving force is scanned through the resonance peak the motion of the oscillator is now out of phase with the driving force. The signal processing method would have an initial out of phase oscillation with respect to the driving force.

While we would like to the definitions in entries 1 or 3 in table C.1 the FFT implementation in many data analysis software is the signal processing definition. Therefore we need to find a way to test the spectral retrieval algorithm with a known phase such that we can extract the correct

phase that has physical significance.

C.2 Testing phase retrival

To begin we construct a signal pulse in the frequency domain $E(\omega)$ which has the desired phase of Eq. C.3 and a flat phase Gaussian reference pulse $E_{ref}(\omega) = \mathrm{e}^{-\frac{(\omega-\omega_0)^2}{\sigma^2}}$. Using the equation for spectral interferometry these two pulses are interfered with each other at a time delay of $\tau = 0.6$ ps producing a interferogram similar to the ones seen in the experiment.

The interferogram is forward Fourier transformed with the function given at the end of this appendix called 'fftPulse' which results in a complex signal in the time domain with frequencies centered at $-\tau$, 0 and τ. The signal at positive τ is windowed and Fourier transformed back into the frequency domain. After subtracting out the residual delay we recover the correct sign of the phase that we started with.

C.3 Direct inversion matlab code

C.3.1 Fourier transforms implemented in matlab

```
function [ E,V ] = fftPulse( t,PulseT )
%fftPulse takes a time domain pulse and converts it to a
%    frequency domain pulse and scales appropriatly.
%
%   t - the time domain scaling
%   PulseT - the pulse in the time domain

%---Creates the frequency scale in 1/t units so typically 1/fs.

npnts = length(t);
stepT = (t(end)-t(1))/npnts;
stepV =  1 / (npnts*stepT);
start = -npnts/2*stepV;
stop = (npnts/2-1)*stepV;
V = start:stepV:stop;

%---Does a proper Fourier Transform on the pulse which preserves the phase.

E = fftshift(fft(fftshift(PulseT)))*stepT;

end
```

```
function [ e,t ] = ifftPulse( V,PulseV )
%fftPulse takes a frequency domain pulse and converts it to a
%    time domain pulse and scales appropriatly.

%   V - frequency domain scaling
%   PulseV - frequence domain pulse

%---Creates the time scale in 1/v units so typically in femtoseconds.

npnts = length(V);
stepV = (V(end)-V(1))/npnts; %was (V(end)-V(1))/npnts
stepT =  1 / (npnts*stepV);
start = -npnts/2*stepT;
stop = (npnts/2-1)*stepT;
t = start:stepT:stop;

%---Does a proper Fourier Transform on the pulse.
e = fftshift(ifft(fftshift(PulseV)))./stepT;

end
```

C.3.2 FTSI implementation in matlab

This will only work with data acquired from our specific setup.

```
function [ xcut,amp_yw_cut,angle_yw_cut,amp_yw,angle_yw,v ] = FTSI( x,y,delay )
%FTSI Algorithm for fourier transform spectral interferometry
%   x - typically data in the frequency domain or pixel domain
%   y - corresponding y values for data in the frequency domain or
%   wavelength domain

%AUTHOR: Cory Nelson
%DATE: 09/09/2013

c = 299792458*(1/1000); %speed of light in nm / ps.
%fourier transform into the time or pseudo time domain.
    if x(1)<x(end); %wavelength scale given
        p = 1:length(x); %create pixel scale
        v = c./x; %frequency in THz from x
        [Y,P] = fftPulse(p,y);
        dv = gradient(v);
        alpha = mean([dv(671) dv(670)]);%calculates instantaneous slope
                                        %at the center of the frequency array
        Z = P/alpha; %called zeta for zeta space
        Yw = windowFT(Z,Y);%window peak the fourier transform must be
                           %scaled to ps.
        [yw] = ifftPulse(Z,Yw); %inverse fourier transforms the windowed
                                %peak
        amp_yw = abs(yw).^2;
        angle_yw = angle(yw);
```

```
        %calculates the phase introduced by the delay and nonlinear spacing
        %v(x) = v0 + a1*x + 0.5 a2*a^2 + 1/6 * a3 a^3 +. . .
        %if calibration is good v(x) should be well known from the
        %wavelength data
        wxtau = 2*pi*(v-max(v))*delay; %Makes linear delay to be subtracted
        angle_yw = -angle_yw+wxtau;

        xcut = v;
        pcut = p;
        angle_yw_cut =angle_yw;
        amp_yw_cut = amp_yw;
        amp_ywN = amp_yw./(max(amp_yw)-min(amp_yw));

        pcut(amp_ywN<=1e-5) = [];
        xcut(amp_ywN<=1e-5) = [];
        angle_yw_cut(amp_ywN<=1e-5) = [];
        amp_yw_cut(amp_ywN<=1e-5) = [];
        %center the angle at 0 in the center of the array
        xM = ceil(xMoment(pcut,angle_yw_cut)); %finds point near center of array
        %angle_yw_cut = angle_yw_cut-mean(angle_yw_cut(xM-20:xM+20));%shifts array to zero

    else %if frequency spacing is given
        [Y,X] = fftPulse(x,y);
        Yw = windowFT(X,Y); %window peak the fourier transform must be scaled to ps.
        [yw] = ifftPulse(X,Yw); %inverse fourier transforms the windowed peak
        amp_yw = abs(yw).^2;
        angle_yw = unwrap(angle(yw));
        wtau = 2*pi*(x-max(x))*delay; %calculates the phase introduced by the delay
        angle_yw = -angle_yw+wtau;

        xcut = x;
        angle_yw_cut =angle_yw;
        amp_yw_cut = amp_yw;
        amp_ywN = amp_yw./(max(amp_yw)-min(amp_yw));

        %trims arrays for data with value less than 1e-5
        %essentially phase blanks the data
        xcut(amp_ywN<=1e-5) = [];
        angle_yw_cut(amp_ywN<=1e-5) = [];
        amp_yw_cut(amp_ywN<=1e-5) = [];

        %center the angle at 0 in the center of the array
        angle_yw_cut = angle_yw_cut-(max(angle_yw_cut)+min(angle_yw_cut))/2;

    end


end
```

```
function [ windowedFT ] = windowFT( xscale,ftdata)
%windowFT takes the fourier transformed data in zeta space and windows the
%positive or negative peak.
%   xscale - the x scaling of the data(in zeta space)should be scaled in ps.
%   ftdata - the fourier transform of the raw data.
```

```
% Since the unkonwn pulse enters the spectrometer first we want the
% peak at the positive delay.  This removes the sign ambiguity.
% This finds the positive delay since zeta space is the inverse the
% positive delay should be at the lower index.

%AUTHOR: Cory Nelson
%DATE: 09/09/2013

    if xscale(1)>0 %check if delay is positive at low index.
        npnts = length(xscale);%number of points in the x scale
        x = xscale(1:npnts/2-25);% extracts pos x values (time in ps)
        after = zeros(1,npnts/2+25);%npnts to be added after the window
        posarray = ftdata(1:npnts/2-25); %extracts the positive y data
    else
        error('dataFormat:wrongformat','Data is not in the'...
            'expected format please check and make sure the data'...
            'are properly scaled in zeta space')
    end

[~,index] = findNearest(x,.6546);% finds the index close to peak.

winpnts = (997-675)*2+1; % calcs num pnts in the window

before = zeros(1,645-winpnts); % calcs num pnts added before window
win = tukeywin(winpnts,0.1).';%creates and transposes Tukey window
wintot = horzcat(before,win,after);
windowedFT = (wintot.').*ftdata;

%%%For trouble shooting purposes only%%%
%disp(winpnts);
%figure;semilogy(xscale,wintot,xscale,abs(ftdata),xscale,abs(windowedFT));

end
```

References

1. Weisstein, E. *Fourier Transform, From mathWorld– A Wolfram Web Resource*.

D

pseudo-code for data acquisition software

Front panel of data acquisition as implemented in LabView. These are provided to get a sense of the control over the experimental parameters that the LabView program allowed.

D.1 TR-FDISH Acquisition

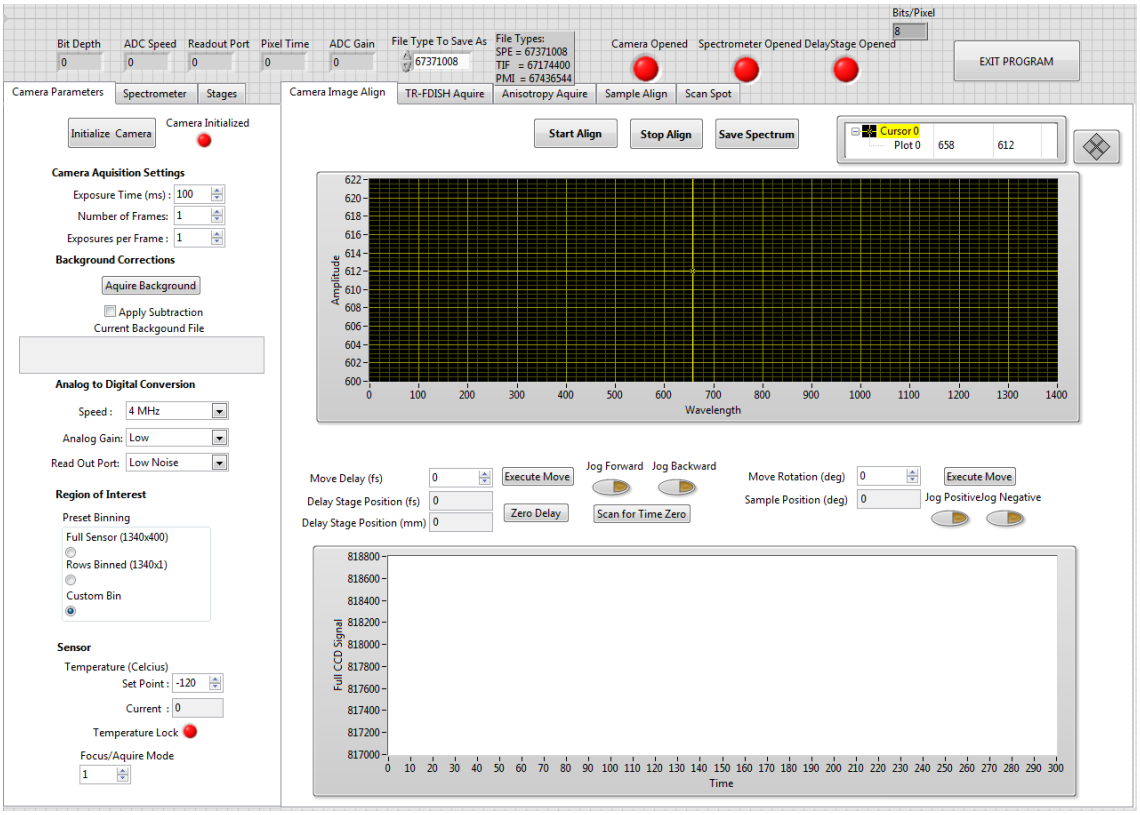
Bit Depth
ADC Speed
Readout Port
Pixel Time
ADC Gain
File Type To Save As
File Types:
SPE = 67371008
TIF = 67174400
PMI = 67436544
Camera Opened
Spectrometer Opened
DelayStage Opened
Bits/Pixel
EXIT PROGRAM
Camera Parameters
Spectrometer
Stages
Camera Image Align
TR-FDISH Aquire
Anisotropy Aquire
Sample Align
Scan Spot
Initialize Camera
Camera Initialized
Camera Aquisition Settings
Exposure Time (ms) :
Number of Frames:
Exposures per Frame :
Background Corrections
Aquire Background
Apply Subtraction
Current Backgound File
Analog to Digital Conversion
Speed :
4 MHz
Analog Gain:
Low
Read Out Port:
Low Noise
Region of Interest
Preset Binning
Full Sensor (1340x400)
Rows Binned (1340x1)
Custom Bin
Sensor
Temperature (Celcius)
Set Point :
Current :
Temperature Lock
Focus/Aquire Mode
Start Align
Stop Align
Save Spectrum
Cursor 0
Plot 0
Amplitude
Wavelength
Move Delay (fs)
Execute Move
Jog Forward
Jog Backward
Delay Stage Position (fs)
Delay Stage Position (mm)
Zero Delay
Scan for Time Zero
Move Rotation (deg)
Sample Position (deg)
Jog Positive
Jog Negative
Full CCD Signal
Time

Figure D.1

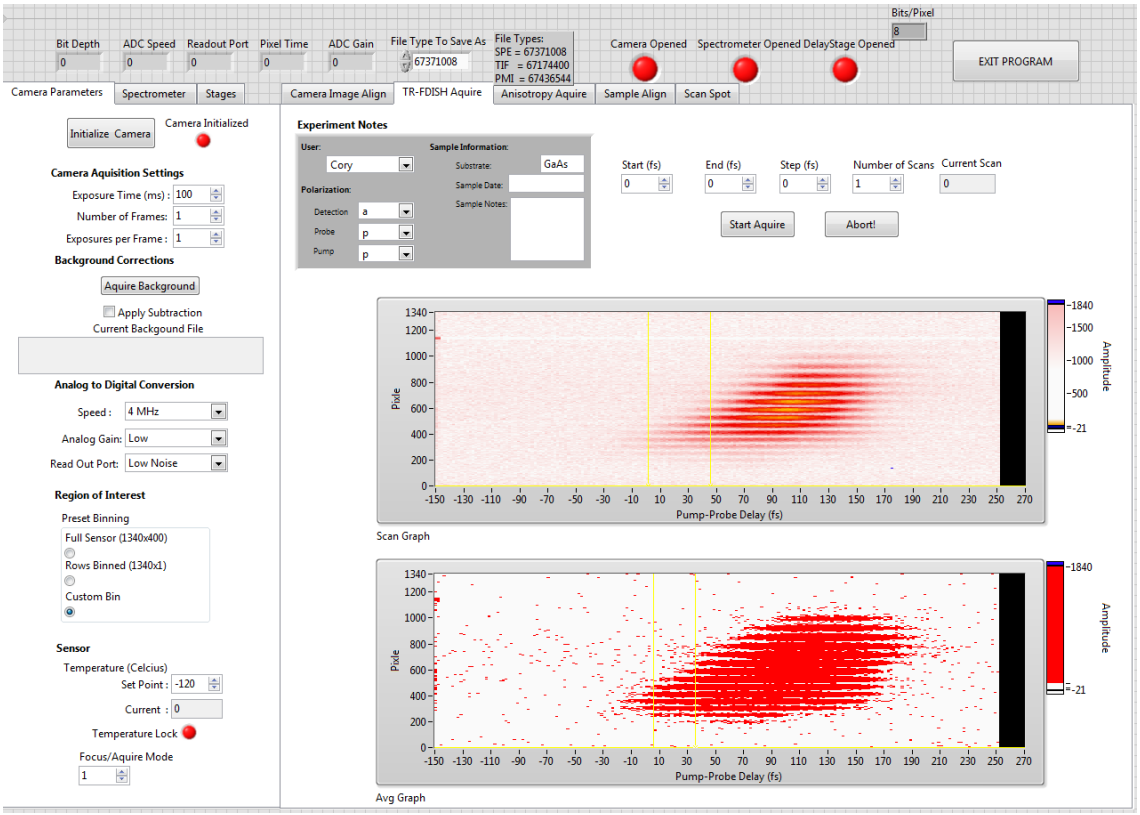

Figure D.2: Fourier transform of Eq. C.2 using the physics definition C.1a and the signal processing definition C.1b The phases have the opposite sign.

E

Gallium arsenide wafer data sheets

Gallium arsenide was ordered from wafer technologies. All measurements of doping concentration cut angle and crystal direction were made by wafer technologies. The specifications of the wafers used in these experiments are summarized in the following pages.

WAFER TECHNOLOGY LTD.

Certificate of Conformance: Single Crystal Materials

Customer		Ingot/lot no.	WV 22215/Zn
Customer specificat		Quantity	
Customer order num		Total weight	
WT order number			

	Specified	Supplied
Material/Growth method	GaAs, VGF	GaAs, VGF
Dopant	Zn p-type	Zn p-type
Orientation	(100) ± 0.1°	(100) ± 0.01°
Diameter/dimensions (mm)	50.5 ± 0.5mm	50.5mm
Flat Option (EJ/SEMI)	EJ	EJ
Major Flat Length(mm)	16 ± 2 on (0-1-1)	16.1 on (0-1-1)
Minor Flat Length(mm)	8 ± 1 on (0-11)	8.1 on (0-11)
Surface Finish/Form	One Side Polished	One Side Polished
Thickness (microns)	350 ± 25µm	351 - 359µm
TIR (microns)	Not Specified	Not Specified
TTV (microns)	Not Specified	Not Specified
Warp (microns)	Not Specified	Not Specified
Additional Information:		

	Specified	Seed End	Tail End
Resistivity (Ωcm)	Not Specified	8.30E-03	3.30E-03
Hall mobility ($cm^2V^{-1}s^{-1}$)	Not Specified	117	121
Carrier concentration (cm^{-3})	(0.5 - 5)E19	6.80E+18	1.70E+19
Average EPD (cm^{-2})	</=3000	761	1655

We hereby certify that the above material has been fully tested and is within quoted specification

Signed by: Production B.J. Ward

Quality Assurance S Russell

Date 15/6/10

SF0088 (Issue G)

34 Maryland Road, Tongwell, Milton Keynes, Bucks MK15 8HJ, England, U.K.

Tel: +44 (0)1908 210444 Fax: +44 (0)1908 210443

www.wafertech.co.uk

WAFER TECHNOLOGY LTD.

Certificate of Conformance: Single Crystal Materials

Customer	UCLA	Ingot/lot no.	WV 23548/Un
Customer specification	QT101211	Quantity	10 Slices
Customer order number	0160 N RB762 00	Total weight	55.1g
WT order number	WT/ 18689 pt 2		

	Specified	Supplied
Material/Growth method	GaAs , VGF	GaAs , VGF
Dopant	Undoped	Undoped
Orientation	(100) ± 0.1°	(100) ± 0.04°
Diameter/dimensions (mm)	50.5 ± 0.5	50.6
Flat Option (EJ/SEMI)	EJ	EJ
Major Flat Length(mm)	16 ± 2 on (0-1-1)	16.7 on (0-1-1)
Minor Flat Length(mm)	8 ± 1 on (0-11)	7.5 on (0-11)
Surface Finish/Form	One Side Polished	One Side Polished
Thickness (microns)	500 ± 25	511 - 520
Bow (microns)	Not Specified	Not Specified
Warp (microns)	Not Specified	Not Specified
TTV (microns)	Not Specified	Not Specified

	Specified	Seed End	Tail End
Resistivity (Ωcm)	>=1E7	3.17E+08	1.77E+08
Hall mobility ($cm^2V^{-1}s^{-1}$)	>=5000	5610	5460
Carrier concentration (cm^{-3})	semi insulating	3.51E+06	6.47E+06
Average EPD (cm^{-2})	<=2000	< 2000	< 2000

Additional Information

We hereby certify that the above material has been fully tested and is within quoted specification

Signed by: Production B.J. Wilson

Quality Assurance A.M. Bowsey

Date 24/1/14

PCF 0003 Iss2

Independently Approved by BSi to ISO 9001
Manufactured under a Quality Assurance System **Certificate Number: FM26963**

34 Maryland Road, Tongwell, Milton Keynes, Bucks MK15 8HJ, England, U.K
Tel: +44 (0)1908 210444 Fax: +44 (0)1908 210443
www.wafertech.co.uk

WAFER TECHNOLOGY LTD.

Certificate of Conformance: Single Crystal Materials

Customer	UCLA	Ingot/lot no.	WV 22023/Si
Customer specification	Q33546	Quantity	17 Slices
Customer order number	0160PME451	Total weight	65.7g
WT order number	WT/ 15973 Pt. 1		

	Specified	Supplied
Material/Growth method	GaAs , VGF	GaAs , VGF
Dopant	Silicon	Silicon
Orientation	(100) ± 0.1°	(100) ± 0.04°
Diameter/dimensions (mm)	50.5 ± 0.5mm	50.5mm
Flat Option (EJ/SEMI)	EJ	EJ
Major Flat Length(mm)	16 ± 2 on (0-1-1)	16.1 on (0-1-1)
Minor Flat Length(mm)	8 ± 1 on (0-11)	8.2 on (0-11)
Surface Finish/Form	One Side Polished	One Side Polished
Thickness (microns)	350 ± 25µm	360 - 366µm
TIR (microns)	Not Specified	Not Specified
TTV (microns)	Not Specified	Not Specified
Warp (microns)	Not Specified	Not Specified

	Specified	Seed End	Tail End
Resistivity (Ωcm)	Not Specified	1.80E-03	1.50E-03
Hall mobility ($cm^2V^{-1}s^{-1}$)	Not Specified	2465	1679
Carrier concentration (cm^{-3})	(1 - 5)E18	1.40E+18	2.50E+18
Average EPD (cm^{-2})	≤ 500	216	216

We hereby certify that the above material has been fully tested and is within quoted specification

Signed by: Production B.J. Wilde

Quality Assurance

Date 29/6/10

SF0088 (Issue F)

34 Maryland Road, Tongwell, Milton Keynes, Bucks MK15 8HJ, England, U.K.
Tel: +44 (0)1908 210444 Fax: +44 (0)1908 210443